

# **Rare Phenomena and $W$ Production in Electron-Proton Scattering at HERA**

**Von der Fakultät für Mathematik, Informatik und Naturwissenschaften  
der Rheinisch-Westfälischen Technischen Hochschule Aachen  
zur Erlangung des akademischen Grades eines Doktors  
der Naturwissenschaften genehmigte Dissertation**

**vorgelegt von**

**Diplom-Physiker**

**Gilles Frising**

**aus Bonn**

**Berichter: Universitätsprofessor Dr. Ch. Berger  
Universitätsprofessor Dr. G. Flügge**

**Tag der mündlichen Prüfung: 15.12.2003**

**Diese Dissertation ist auf den Internetseiten der Hochschulbibliothek online verfügbar.**



## Abstract

A general and model-independent search for deviations from the Standard Model prediction is performed in  $ep$  collisions at HERA using H1 data corresponding to an integrated luminosity of  $115 \text{ pb}^{-1}$ . All experimentally measurable event topologies involving electrons, photons, muons, neutrinos and jets with high transverse momenta are investigated. Events are classified into exclusive event classes according to their final state. A new algorithm is used to look for regions with deviations from the Standard Model in the invariant mass and sum of transverse momenta distributions and to quantify the significance of the observed deviations. A good agreement with the Standard Model prediction is found in most of the event classes. The largest deviation occurs in topologies with an isolated muon, missing transverse momentum and a jet. About 2% of hypothetical Monte Carlo experiments would produce deviations more significant than the one observed in the corresponding sum of transverse momenta distribution. Within the Standard Model events with an isolated muon, or, more general, a charged lepton, and missing transverse momentum are expected to be mainly due to  $W$  boson production with subsequent leptonic decay. The H1 and ZEUS collaborations have already searched for such events and found, in accordance with the general search, an excess of events with high transverse momentum of the hadronic system. Complementary, a search for  $W$  bosons in the dominant hadronic decay channel is performed. The phase space is optimised to maximise the acceptance for  $W$  events and reduce other Standard Model contributions. The data are compared to the predictions of quantum chromodynamics as a function of the transverse momentum of the hadronic system after excluding the  $W$  candidate jets and found to be in good agreement in this regard.

## Kurzfassung

Eine allgemeine und Modell-unabhängige Suche nach Abweichungen von der Vorhersage des Standard-Modells wird in  $ep$ -Kollisionen bei HERA durchgeführt. Die analysierten H1-Daten entsprechen einer integrierten Luminosität von  $115 \text{ pb}^{-1}$ . Alle experimentell messbaren Ereignistopologien mit Elektronen, Photonen, Myonen, Neutrinos und Jets mit hohen Transversalimpulsen werden untersucht. Die Ereignisse werden ihrem Endzustand entsprechend in exklusive Klassen eingeteilt. Ein neuer Algorithmus wird verwendet, um nach Regionen mit Abweichungen vom Standard-Modell in den Verteilungen der invarianten Masse und Summe der Transversalimpulse zu suchen und die Signifikanz der beobachteten Abweichungen zu quantifizieren. Eine gute Übereinstimmung mit der Vorhersage des Standard-Modells liegt in den meisten Ereignisklassen vor. Die größte Abweichung wird in Topologien mit einem isolierten Myon, fehlendem Transversalimpuls und einem Jet gefunden. Etwa 2% von hypothetischen Monte-Carlo-Experimenten würden signifikantere Abweichungen hervorrufen, als die, die in der entsprechenden Verteilung der Summe der Transversalimpulse beobachtet wird.

Innerhalb des Standard-Modells werden Ereignisse mit einem isolierten Myon, oder allgemeiner, einem geladenem Lepton, und fehlendem Transversalimpuls überwiegend der Produktion von  $W$ -Bosonen mit anschließendem leptonischen Zerfall zugeschrieben. Die H1- und ZEUS-Kollaborationen haben bereits nach solchen Ereignissen gesucht und haben, in Übereinstimmung mit der allgemeinen Suche, einen Überschuss von Ereignissen mit einem hohen Transversalimpuls des hadronischen Systems gefunden. Zusätzlich wird eine Suche nach  $W$ -Bosonen im dominanten hadronischen Zerfallskanal durchgeführt. Der Phasenraum wird optimiert, um die Akzeptanz für  $W$ -Ereignisse zu maximieren und andere Beiträge des Standard-Modells zu reduzieren. Die Daten werden mit den Vorhersagen der Quantenchromodynamik als Funktion des Transversalimpulses des hadronischen Systems abzüglich der Jets des  $W$ -Kandidaten verglichen, und es wird diesbezüglich eine gute Übereinstimmung gefunden.



---

# Contents

---

<b>1</b>	<b>Introduction</b>	<b>1</b>
<b>2</b>	<b>High Transverse Momentum Physics at HERA</b>	<b>3</b>
2.1	Deep Inelastic Lepton-Proton Scattering . . . . .	3
2.1.1	Kinematics . . . . .	3
2.1.2	Parton Model and Quantum Chromodynamics . . . . .	4
2.1.3	Inclusive Deep Inelastic Scattering Cross Section . . . . .	5
2.1.4	Production of Jets . . . . .	7
2.2	Photoproduction of Jets . . . . .	7
2.3	Prompt Photon Production . . . . .	8
2.4	Hard Radiative Processes . . . . .	10
2.5	Lepton Pair Production . . . . .	11
2.6	$W$ Production . . . . .	13
2.7	$Z$ Production . . . . .	13
2.8	Beyond the Standard Model . . . . .	15
2.9	Monte Carlo Generators . . . . .	20
<b>3</b>	<b>H1 Experiment at HERA</b>	<b>23</b>
3.1	HERA Collider . . . . .	23
3.2	H1 Detector . . . . .	24
3.2.1	Calorimetry . . . . .	24
3.2.2	Inner Tracking System . . . . .	27
3.2.3	Muon Detectors . . . . .	29
3.2.4	H1 Trigger System . . . . .	30

<b>4</b>	<b>General Search for New Phenomena</b>	<b>33</b>
4.1	Introduction . . . . .	33
4.2	Standard Model Expectation . . . . .	34
4.3	Data Selection . . . . .	36
4.4	Object Definitions and Event Classification . . . . .	38
4.4.1	Jet Identification . . . . .	38
4.4.2	Electron Identification . . . . .	47
4.4.3	Photon Identification . . . . .	49
4.4.4	Muon Identification . . . . .	50
4.4.5	Neutrino Identification . . . . .	53
4.5	Electron Calibration . . . . .	58
4.6	Hadronic Final State Reconstruction and Calibration . . . . .	58
4.7	Trigger . . . . .	63
4.8	Resolution . . . . .	63
4.9	Efficiencies and Purities . . . . .	63
4.10	Systematic Uncertainties . . . . .	65
4.11	Results . . . . .	68
4.12	Search for Deviations from the Standard Model . . . . .	69
4.12.1	Search Algorithm . . . . .	69
4.12.2	Search Results . . . . .	71
<b>5</b>	<b>Search for W Bosons in the Hadronic Decay Channel</b>	<b>83</b>
5.1	Introduction . . . . .	83
5.2	Standard Model Expectation . . . . .	84
5.3	Event Selection . . . . .	84
5.3.1	Basic Event Selection . . . . .	84
5.3.2	Multivariate Likelihood Analysis . . . . .	88
5.4	Systematic Uncertainties . . . . .	92
5.5	Results . . . . .	95
<b>6</b>	<b>Summary and Outlook</b>	<b>99</b>
<b>A</b>	<b>Track Selection</b>	<b>101</b>
<b>B</b>	<b>Particular Events</b>	<b>103</b>
<b>C</b>	<b>Comparison of Different Jet Quality Criteria</b>	<b>109</b>
<b>D</b>	<b>Shape Difference between Data and Standard Model</b>	<b>113</b>
<b>E</b>	<b>Compatibility of Measurements</b>	<b>115</b>

---

# Introduction

---

The Standard Model (SM) provides a complete theory of the strong and electroweak interactions of elementary particles and has passed many stringent experimental tests in the past decades. On the other hand, the SM leaves many unanswered questions concerning *e.g.* the hierarchy between the electroweak and the gravity scale, the origin of lepton and quark masses, the nature of gravity and the unification of forces. There exist various other theoretical models which overcome the deficiencies of the SM by extending the physics beyond the SM. These extensions of the SM predict new physics which is favoured to occur at the  $\mathcal{O}(\text{TeV})$  scale. A possible discovery of new physics would then be in the reach of current and future high-energy collider experiments.

The electron<sup>1</sup>-proton collider HERA<sup>2</sup> [1] has, in consideration of its high centre-of-mass energy of up to 319 GeV, a sensitivity to many signals of new physics, in particular to processes involving electron-quark, photon-quark, electron-gluon or electron-photon interactions. This work describes both a general and a dedicated search for new phenomena in *ep* collisions at HERA.

The general approach consists of a broad-range search for deviations from the SM prediction in many different event classes which are defined by the number and types of high transverse momentum particles found in *ep* scattering events at HERA. In contrast to a dedicated search for new phenomena, a general search does not rely on a specific final state topology and is in this sense model-independent: a large number of signatures predicted by many different exotic models are coherently searched for in one single analysis, and also unanticipated manifestations of new physics might be discovered. On the other hand, the general search may have an enlarged sensitivity to signals that are weak in one, but present in more than one event class. Consequently, it is crucial to have a reliable SM prediction covering the full phase space of all relevant physics processes at HERA. A new algorithm is used to look in each studied event class for the region with the largest deviation from the SM in the invariant mass and sum of transverse momenta distributions and to give the likelihood to observe this deviation in the considered event class and

---

<sup>1</sup>In this work, "electron" refers to both electrons and positrons if not otherwise stated.

<sup>2</sup>Hadron-Elektron-Ring-Anlage

in all considered event classes. The preliminary results of this analysis are reported in ref. [2]<sup>3</sup>.

The second search is dedicated to  $W$  bosons in the hadronic decay channel. The analysis is triggered by an excess resulting from a search for events with a high energy isolated electron or muon and missing transverse momentum [4]. Within the SM such events are expected to be mainly due to  $W$  boson production with subsequent leptonic decay. Whilst the overall number of events observed in the latter search is broadly in agreement with the number predicted by the SM, there is an excess of events with transverse momentum of the hadronic system,  $P_T^X$ , greater than 25 GeV with ten events found compared to  $2.9 \pm 0.5$  expected. At  $P_T^X > 40$  GeV, the excess is even more significant with six events found compared to an expectation of  $1.08 \pm 0.22$ . In addition, the excess in the muon channel alone is quantified in the aforementioned general search for new phenomena to be the largest deviation in the H1 data. Since an excess of events with final states consistent with leptonic  $W$  decays is observed, it is interesting to search for  $W$  bosons decaying hadronically. Although this channel suffers from high backgrounds, an anomalously large  $W$  production rate could be visible. The results of this analysis are published in ref. [4].

This work is organised as follows. Chapter 2 gives a theoretical overview of high transverse momentum physics at HERA. In chapter 3 the general purpose detector of the H1 experiment at the HERA facility is described. Chapter 4 presents the general search for new phenomena. In chapter 5 follows the search dedicated to  $W$  bosons in the hadronic decay channel. A summary and an outlook are finally given in chapter 6.

---

<sup>3</sup>The final results as well as many complements to this analysis are to be found in ref. [3].



---

# High Transverse Momentum Physics at HERA

---

The high centre-of-mass energy available at HERA gives an experimental access to high transverse momentum physics, where signals of new physics are predicted by many extensions of the SM. This chapter starts with the description of the production of high transverse momentum final states in  $ep$  collisions. It follows an overview of some models beyond the SM which favour the existence of exotic phenomena in the region of high transverse momentum. The last section is related to the so-called Monte Carlo technique, which allows for a comparison of the measured data with the theoretical predictions, and presents the Monte Carlo models used in this work. Almost all arguments in this chapter are taken from textbooks [5] or overview articles [6].

## 2.1 Deep Inelastic Lepton-Proton Scattering

### 2.1.1 Kinematics

Deep inelastic lepton-proton scattering proceeds either via the exchange of a photon, a  $Z$  boson (neutral current (NC) interactions) or a  $W$  boson (charged current (CC) interactions). Fig. 2.1 illustrates lepton-proton scattering. The quantities  $k$  and  $k'$  denote respectively the four-momenta of the incoming and outgoing leptons,  $P$  is the four-momentum of the incoming proton, and  $X$  is the recoiling system. The exchanged particle transfers the four-momentum  $q = k - k'$  to the proton. Lorentz-invariant quantities which are commonly used are described in the following.

- The centre-of-mass energy squared of the lepton-proton system is

$$s = (k + P)^2.$$

- The quantity  $Q^2 = -q^2$  corresponds to the virtuality of the exchanged gauge boson.

- The inelasticity  $y$  is given by

$$y = \frac{P \cdot q}{P \cdot k}.$$

It is the longitudinal energy fraction of the lepton which is carried away by the exchanged particle. In the proton rest frame,  $y$  can be interpreted as the fraction of the lepton's energy loss.

- The Bjorken scaling variable is defined through

$$x = \frac{Q^2}{2P \cdot q}.$$

Its interpretation is given in the next section.

The four introduced kinematic quantities are not independent of each other. Ignoring the electron and proton masses, they are related via

$$Q^2 = sxy.$$

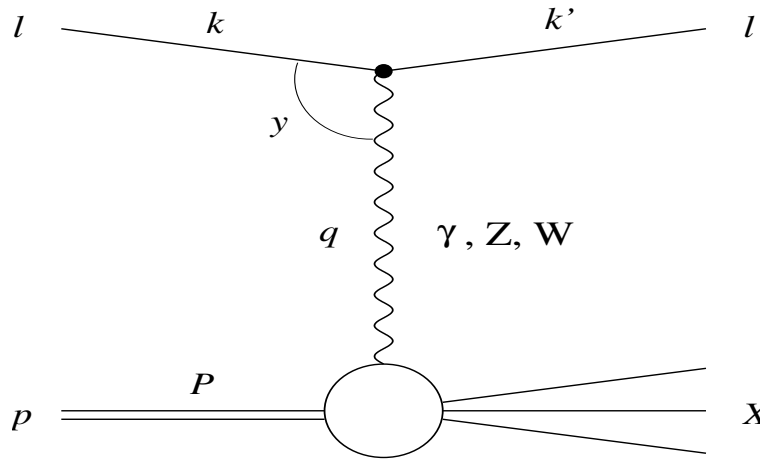


Figure 2.1: Illustration of lepton-proton scattering.

### 2.1.2 Parton Model and Quantum Chromodynamics

In the parton model, which was proposed by Feynman around 1970 [7], the proton is assumed to be made of a small number of constituents, the partons, which can be quarks and anti-quarks or neutral constituents responsible for their binding. In a frame where the proton momentum is very large (infinite momentum frame), the partons have negligible transverse momentum, and the proton can be described by a state of collinear partons which carry only a certain longitudinal

fraction  $\xi$  of the proton's total momentum. The parton density functions (PDFs)  $f_i(\xi)$  give the number density of finding a parton of type  $i$  with a momentum fraction  $\xi$  in the proton.

In the Quark-Parton Model (QPM), all partons are identified with quarks and anti-quarks, and the lepton-proton scattering is interpreted as an incoherent scattering of the lepton off the quark constituents. If one further makes the assumption that the underlying lepton-quark scattering is elastic, the Bjorken scaling variable  $x$  is equivalent to  $\xi$ . One of the most striking predictions of the QPM is that the PDFs and therefore the so-called structure functions, which parametrise the structure of the proton (see next section), scale, *i.e.* they depend only on  $x$  in the Bjorken limit ( $Q^2, P \cdot q \rightarrow \infty$ ). This behaviour is known as Bjorken scaling [8] and is only valid if one assumes that the transverse momentum of the partons in the frame of reference is small.

In the SM, Quantum Chromodynamics (QCD) is the gauge field theory of strong interactions. The quarks come in three colours and the gauge bosons of QCD are eight gluons, carrying a combination of colour and anti-colour. The radiation of hard gluons from the quarks modifies the transverse momentum of the quarks and leads to logarithmic violations of the Bjorken scaling. The PDFs become scale-dependent, *i.e.*  $f_i(\xi) \rightarrow f_i(\xi, \mu^2)$ ; they give the number density of finding a parton of type  $i$  with a momentum fraction  $\xi$  in the proton integrated over the transverse momentum of the radiated gluons up to the factorisation scale  $\mu$ .

### 2.1.3 Inclusive Deep Inelastic Scattering Cross Section

In the SM, a photon or a  $Z$  boson is exchanged in a NC interaction. The cross section for neutral current scattering  $e^\pm p \rightarrow e^\pm X$ , can be expressed as [9]

$$\frac{d^2\sigma_{\text{NC}}^\pm}{dx dQ^2} = \frac{2\pi\alpha^2}{xQ^4} \phi_{\text{NC}}^\pm (1 + \Delta_{\text{NC}}^{\pm, \text{weak}}), \quad (2.1)$$

$$\text{with} \quad \phi_{\text{NC}}^\pm = Y_+ \tilde{F}_2 \mp Y_- x \tilde{F}_3 - y^2 \tilde{F}_L, \quad (2.2)$$

where  $\alpha$  is the fine structure constant. The weak corrections,  $\Delta_{\text{NC}}^{\pm, \text{weak}}$ , are defined in ref. [10] and are typically less than 1% [9]. The helicity dependences of the electroweak interactions are contained in  $Y_\pm = 1 \pm (1 - y)^2$ . The structure function  $\tilde{F}_2$  takes into account the dominant contribution from pure  $\gamma$  exchange, the contributions from pure  $Z$  exchange and its interference with  $\gamma$  exchange.  $\tilde{F}_3$  receives only contributions from pure  $Z$  exchange and  $\gamma Z$  interference. The contributions due to  $Z$  boson exchange only become important at  $Q^2 \gtrsim M_Z^2$ , with  $M_Z$  denoting the mass of the  $Z$  boson. In the region  $Q^2 \ll M_Z^2$ , the latter contributions are negligible and  $\tilde{F}_2$  reduces to the electromagnetic structure function  $F_2$ . In the region  $Q^2 \gtrsim M_Z^2$ , the  $\gamma Z$  interference provokes a difference in the NC cross sections between  $e^+p$  and  $e^-p$  scattering (see fig. 2.2).

The structure functions can be expressed in terms of the PDFs  $f_i(\xi, \mu^2)$ ; the scale  $\mu^2$  is usually chosen to be  $Q^2$ . The longitudinal structure function  $\tilde{F}_L$  is of the order of the strong coupling  $\alpha_s$ . In the QPM, where  $\tilde{F}_L = 0$ , the structure function  $\tilde{F}_2$  ( $\tilde{F}_3$ ) is related to the sum (difference) of the quark and anti-quark momentum distributions,  $xq_i(x)$  and  $x\bar{q}_i(x)$ .

In a CC interaction, a  $W^+$  or  $W^-$  boson is exchanged. The expression of the cross section is similar to that of NC interactions [9]

$$\frac{d^2\sigma_{CC}^\pm}{dx dQ^2} = \frac{G_F^2}{2\pi x} \frac{M_W^4}{(Q^2 + M_W^2)^2} \phi_{CC}^\pm (1 + \Delta_{CC}^{\pm, \text{weak}}), \quad (2.3)$$

$$\text{with } \phi_{CC}^\pm = \frac{1}{2}(Y_+ W_2^\pm \mp Y_- x W_3^\pm - y^2 W_L^\pm), \quad (2.4)$$

where  $M_W$  is the mass of the  $W$  boson,  $G_F$  is the Fermi constant and  $\Delta_{CC}^{\pm, \text{weak}}$  represents the CC weak radiative corrections. The CC structure functions are defined in analogy to the NC structure functions [11]. In the QPM, where  $W_L^\pm = 0$ , the structure functions are related to the quark densities, e.g. for the charged current process  $e^+p \rightarrow \bar{\nu}X$ :

$$W_2^+ = \sum_i 2x(d_i + \bar{u}_i) \quad (2.5)$$

$$xW_3^+ = \sum_i 2x(d_i - \bar{u}_i), \quad (2.6)$$

where the sum runs over all active flavours  $i$ , and where the quark flavour mixing has been neglected. For  $e^-p \rightarrow \nu X$ , the structure functions are obtained by interchanging the up- and down-type quark densities  $u_i$  and  $d_i$ , respectively. The difference between the up- and down-type quark distributions and the  $y$  dependence of the corresponding contributions explain the difference of the CC cross sections between  $e^+p$  and  $e^-p$  scattering. At  $Q^2 \gtrsim 10^4 \text{ GeV}^2$ , the contributions from the photon and  $Z$  exchange to the NC cross section get of similar size to those of  $W^\pm$  exchange. Fig. 2.2 impressively corroborates these effects.

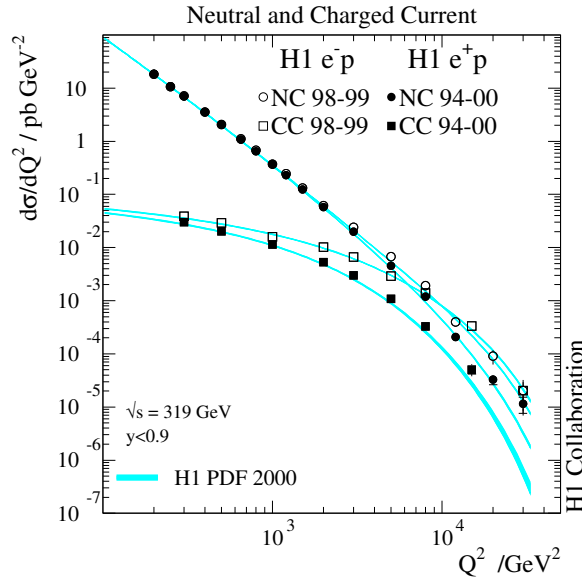


**Figure 2.2:** The  $Q^2$  dependences of the NC (circles) and the CC (squares) cross sections  $d\sigma/dQ^2$  shown for  $e^+p$  (solid points) and  $e^-p$  (open points) data and the corresponding SM expectations (error bands) [9].

### 2.1.4 Production of Jets

At lowest order in  $\alpha_s$  ( $\mathcal{O}(\alpha_s^0)$ ), the  $ep$  deep inelastic scattering (DIS) process produces a final state consisting of  $(1+1)$  jets. One jet arises from the parton emerging out of the hard scattering process and the other from the proton rest (proton remnant). At next order in  $\alpha_s$  ( $\mathcal{O}(\alpha_s)$ ), a gluon participates in the hard scattering process, and a  $(2+1)$  jet final state is produced. The  $\mathcal{O}(\alpha_s)$  diagrams which contribute to this so-called dijet production in DIS are the boson-gluon fusion and the QCD Compton process. They are shown for photon exchange processes in figs. 2.3 and 2.4, respectively, and are similar for  $Z$  and  $W$  boson exchange processes. Higher jet multiplicities in DIS result from higher order QCD effects.

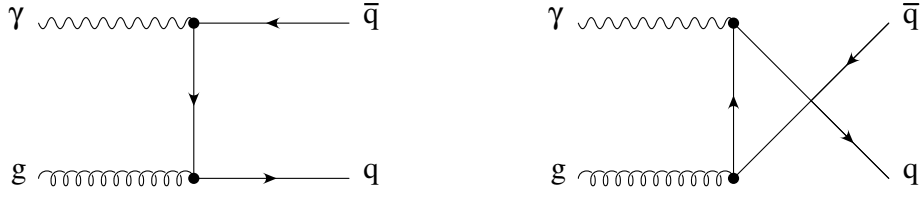


Figure 2.3: Boson-gluon fusion.

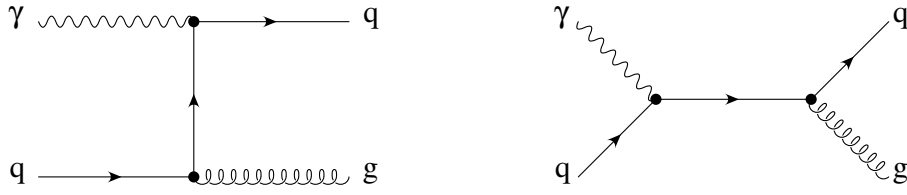


Figure 2.4: QCD Compton scattering.

## 2.2 Photoproduction of Jets

The majority of events at HERA are NC  $ep$  scattering events where the electron is emitted at small angles. The virtuality of the exchanged photon is consequently small ( $Q^2 \lesssim 1 \text{ GeV}^2$ ). This small  $Q^2$  region is usually referred to as the photoproduction region as the proton interacts with quasi-real photons. The flux of photons out of the electron,  $f_{\gamma/e}$ , can be approximated by the integrated Weizsäcker-Williams formula [12, 13, 14]

$$f_{\gamma/e}(y) = \frac{\alpha}{2\pi} \left[ \frac{1 + (1-y)^2}{y} \ln \frac{Q_{\text{max}}^2}{Q_{\text{min}}^2} - 2M_e^2 y \left( \frac{1}{Q_{\text{min}}^2} - \frac{1}{Q_{\text{max}}^2} \right) \right],$$

where  $M_e$  is the electron mass, and

$$Q_{\text{min}}^2 = \frac{M_e^2 y^2}{1-y}$$

is the kinematically smallest accessible virtuality.  $Q_{\max}^2$  is given by experimental conditions. The electron-proton scattering cross section  $\sigma_{ep}$  can be written as convolution of the photon-proton scattering cross section  $\sigma_{\gamma p}$  with the photon flux  $f_{\gamma/e}$ ,

$$\sigma_{ep} = \int dy f_{\gamma/e}(y) \sigma_{\gamma p}(y). \quad (2.7)$$

In QCD, the photoproduction of jets is described by the hard interaction of real photons with partons inside the proton. The photon can either interact directly (direct photoproduction) or first split into partons, and one of the resulting partons subsequently participates with only a fraction of the photon momentum in the hard interaction (resolved photoproduction). This distinction is unambiguously defined only in leading order (LO). Figs. 2.3 and 2.4 show the Born diagrams for the direct photoproduction of dijets and are, apart from the virtuality of the exchanged photon, equal to those in NC DIS. The Born diagrams for the resolved photoproduction of dijets are shown in fig. 2.6. The photoproduction of higher jet multiplicities proceeds via higher order QCD effects.

### 2.3 Prompt Photon Production

The direct as well as the resolved photoproduction of prompt photons proceeds either through direct production or fragmentation. Photons emerging from fragmentation usually lie inside hadronic jets, while directly produced photons tend to be isolated from the final state hadrons. The contribution of fragmentation processes is thus strongly suppressed by an isolation requirement for the photon. Only the production of isolated photons is relevant for this work and considered in the following. Examples of LO diagrams for direct and resolved non-fragmentation processes are depicted in fig. 2.5. Their cross section is of the order  $\alpha^2$ .

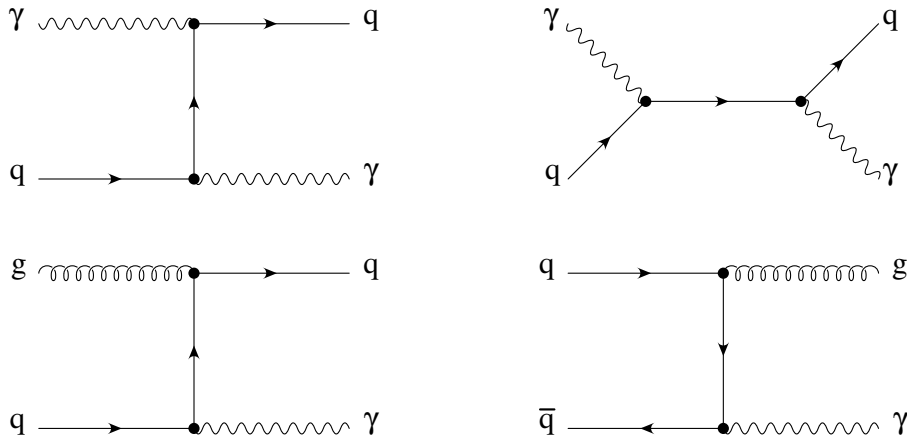


**Figure 2.5:** Examples of LO diagrams for direct (top) and resolved (bottom) prompt photon production.

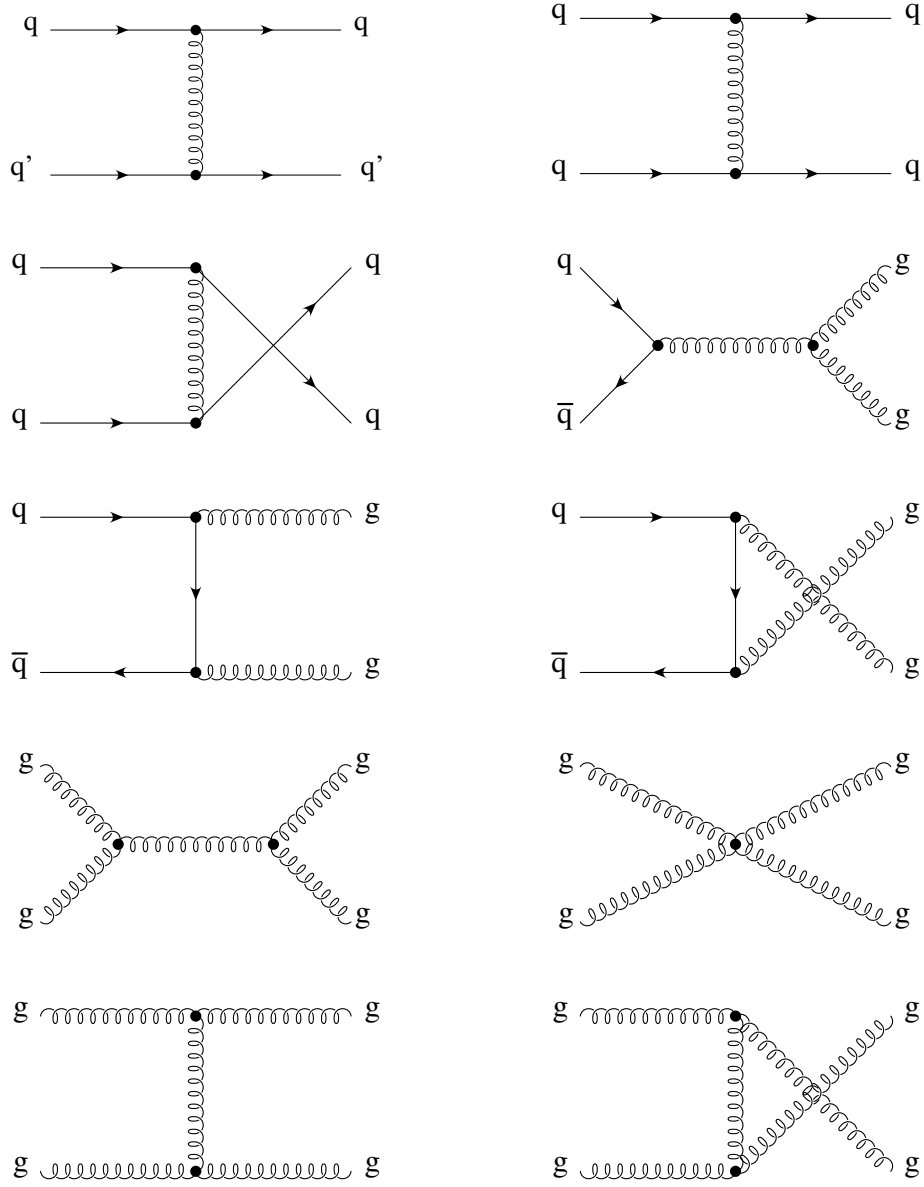


**Figure 2.6:** Born diagrams for resolved photoproduction.

## 2.4 Hard Radiative Processes

The dominant radiative contributions to elastic and inelastic NC  $ep$  scattering arise from the initial and final state radiation of a real photon from the lepton line as depicted in figs. 2.7a and 2.7b, respectively. The inelastic NC  $ep$  scattering processes are usually further divided into processes where a resonant state of the proton is produced (quasi-elastic) and DIS processes (sec. 2.1); in elastic and quasi-elastic processes the proton stays intact.

In analogy to the virtuality  $Q^2$  of the exchanged boson, one defines the virtuality of the exchanged electron as

$$Q'^2 = -q'^2 = \begin{cases} -(k - K)^2 & \text{(fig. 2.7a)} \\ -(k' + K)^2 & \text{(fig. 2.7b)} \end{cases},$$

where  $K$  is the four-momentum of the radiated photon. The presence of a real photon introduces a second propagator from the intermediate virtual electron in the cross section formula

$$\frac{d^2\sigma}{dQ^2 dQ'^2} \sim \frac{1}{Q^4} \frac{1}{(Q'^2 - M_e^2)^2}.$$

Depending on the relative values of  $Q^2$  and  $Q'^2$ , one may differentiate between three kinematic domains:

- $Q^2 \rightarrow 0, Q'^2 \rightarrow 0$ : **Bremsstrahlung**  
Both the final state electron and photon emerge at very small polar angles. The bremsstrahlung processes can be further subdivided into elastic and inelastic processes. The dominant, elastic part of the cross section consists of the Bethe-Heitler process [15], which is used at HERA to measure the luminosity (sec. 3.2.1). The inelastic part, as defined above, forms the radiative photoproduction processes.
- $Q^2 \rightarrow 0, Q'^2 > 0$ : **QED Compton Process**  
The QED Compton scattering is dominated by the elastic process  $ep \rightarrow e\gamma p$ . The scattered electron as well as the radiative photon are emitted under large polar angles. Correspondingly, the QED Compton scattering is sometimes referred to as wide angle bremsstrahlung.
- $Q^2 \gg 0, Q'^2 \rightarrow 0$ : **Radiative DIS Process**  
These processes belong to the radiative corrections of the DIS processes. The angular distribution exhibits two peaks around the direction of the initial and final state electrons. If the photon is radiated by a final state electron, both electromagnetic particles mostly form a common energy cluster which cannot be experimentally disentangled.

In CC DIS  $ep$  scattering, the dominant radiative contribution arises also from the radiation of a real photon from the lepton line, but with the difference that it can only occur in the initial state. The corresponding process is similar to the NC process shown in diagram 2.7a. In a CC interaction, a real photon can also be radiated by the exchanged  $W$  boson.



In contrast to these radiative processes, where the beam electron radiates a photon, the radiation of a photon from the quark line is suppressed due to the relative large effective quark masses. The corresponding diagrams are shown for NC interactions in figs 2.7c and 2.7d. On the other hand, the boson radiated from the lepton or the quark line may also be a  $W$  or a  $Z$  boson, which is however more unlikely in consideration of the high  $W$  and  $Z$  boson masses. The production of  $W$  and  $Z$  bosons is treated in more detail in sec. 2.6 and sec. 2.7, respectively.

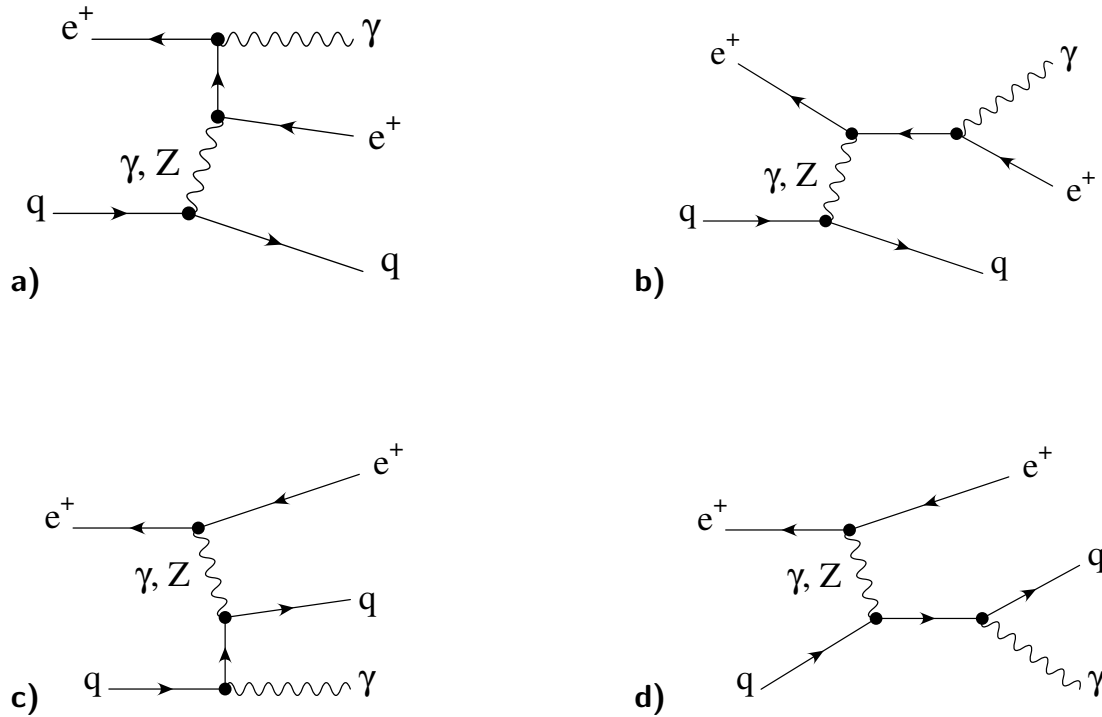


**Figure 2.7:** Radiative NC processes, which may involve a photon conversion. Diagrams a) and b) represent the photon radiation from the lepton, diagrams c) and d) the radiation from the quark side. If the radiated photon converts into a lepton pair, diagram a) is also referred to as Cabibbo-Parisi process and diagram c) as Drell-Yan process (see sec. 2.5).

## 2.5 Lepton Pair Production

Lepton pair production at HERA proceeds mainly through photon-photon scattering. Another source of lepton pair production are radiative processes involving a conversion of the radiated photon or  $Z$  boson into a lepton pair. Both production mechanisms are described in the following.

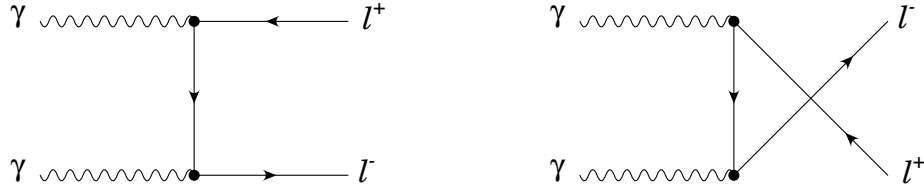


**Figure 2.8:** Lepton pair production via the two-photon process. The  $t$ - and  $u$ -channel contributions are shown on the left and right side, respectively.

### Photon-Photon Scattering

In photon-photon scattering at HERA, the interaction of the initial electron and proton proceeds via the interaction of two photons radiated from the incident electron and proton. Fig. 2.8 shows the Born diagrams for lepton pair production via the corresponding two-photon process. The cross section of the two-photon process  $\sigma_{\gamma\gamma}$  can be related to the  $ep$  cross section via the photon fluxes. The photon flux from the electron  $f_{\gamma/e}$  has already been presented in sec. 2.2. The description of the photon flux from the proton is more complicated: elastic and inelastic scattering have to be distinguished. In the elastic case, the photon spectrum  $f_{\gamma/p}$  radiated by the proton depends on the longitudinal energy fraction  $z_p$  of the proton which is carried away by the photon. The corresponding formula for the photon spectrum is given in ref. [13].

In the deep inelastic case, the photon flux can be expressed within the QPM as a convolution of the photon flux from a quark  $f_{\gamma/q}$  with the probability to find a quark in the proton

$$f_{\gamma/p}(z_p) = \int dx f_{q/p}(x) f_{\gamma/q}\left(\frac{z_p}{x}\right). \quad (2.8)$$

In the photoproduction limit both photons have a vanishing virtuality, and the  $ep$  cross section can be written as a convolution of the photon fluxes from the electron and proton with the two-photon cross section

$$\sigma_{ep} = \int dz_p dy f_{\gamma/p}(z_p) f_{\gamma/e}(y) \sigma_{\gamma\gamma}. \quad (2.9)$$

### Radiative Processes and Photon Conversion

Radiative processes can involve a subsequent conversion of the radiated photon or  $Z$  boson into a fermion pair. In case of a conversion into a lepton pair, they contribute to lepton pair production at HERA. The radiative processes are shown in fig. 2.7. The initial state radiation processes (figs. 2.7a,c) producing a lepton pair are usually further classified:

- **Cabibbo-Parisi Process**

When the photon is radiated from the initial quark line, the underlying lepton pair production process can be interpreted as an internal conversion of the photon followed by an

electron-positron scattering ( $e^+e^- \rightarrow l^+l^-$ ) and is termed Cabibbo-Parisi process. Among all electroweak lepton pair production processes, the cross section of the Cabibbo-Parisi processes strongly depends on the produced lepton flavour. In particular, the electron pair production proceeds through Bhabha scattering ( $e^+e^- \rightarrow e^+e^-$ ) and is here much more enhanced due to the existence of the  $t$ -channel.

- **Drell-Yan Process**

When the photon is radiated from the initial quark line, the underlying lepton pair production process is  $q\bar{q} \rightarrow l^+l^-$  and usually referred to as Drell-Yan process. In the photoproduction regime ( $Q^2 \rightarrow 0$ ), the photon can fluctuate into a hadronic state, and one has to further distinguish between the point-like and the resolved Drell-Yan process. The Drell-Yan process only marginally contributes to the total electroweak lepton pair production cross section. At high transverse momentum of the leptons, it gains nevertheless in importance [16].

## 2.6 $W$ Production

Real  $W$  bosons in  $ep$  scattering are dominantly produced via the reaction  $ep \rightarrow eWX$ . The corresponding LO Feynman graphs are shown in figs. 2.9a-c and figs. 2.9f,g for a quark and a positron in the initial state. The graphs with an anti-quark or an electron in the initial state are similar.

The dominant contribution to the  $ep \rightarrow eWX$  cross section arises from initial state  $W$  radiation (fig. 2.9a) when the photon and the  $u$ -channel quark are close to the mass shell [17]. The final state  $W$  radiation is shown in fig. 2.9b. Diagram 2.9c contains the  $WW\gamma$  vertex. Diagrams 2.9f and 2.9g are suppressed by the second  $W$  boson propagator. Finally, diagrams 2.9d and 2.9e are needed in order to preserve gauge invariance [17].

## 2.7 $Z$ Production

$Z$  production at HERA proceeds mainly through the processes presented in fig. 2.7 in which the radiated photon has to be replaced by a  $Z$  boson. Diagrams 2.7a and 2.7b describe the initial and final state radiation of a  $Z$  boson from the electron line, respectively. The corresponding radiation from the quark line is described by the diagrams 2.7c and 2.7d. In contrast to  $W$  production, the analogue of diagram 2.9c does not exist as the  $ZZ\gamma$  coupling vanishes in the SM. Moreover, non-resonant diagrams like diagrams 2.9d and 2.9e are not needed because the  $Z$  boson does not carry electric charge [17].

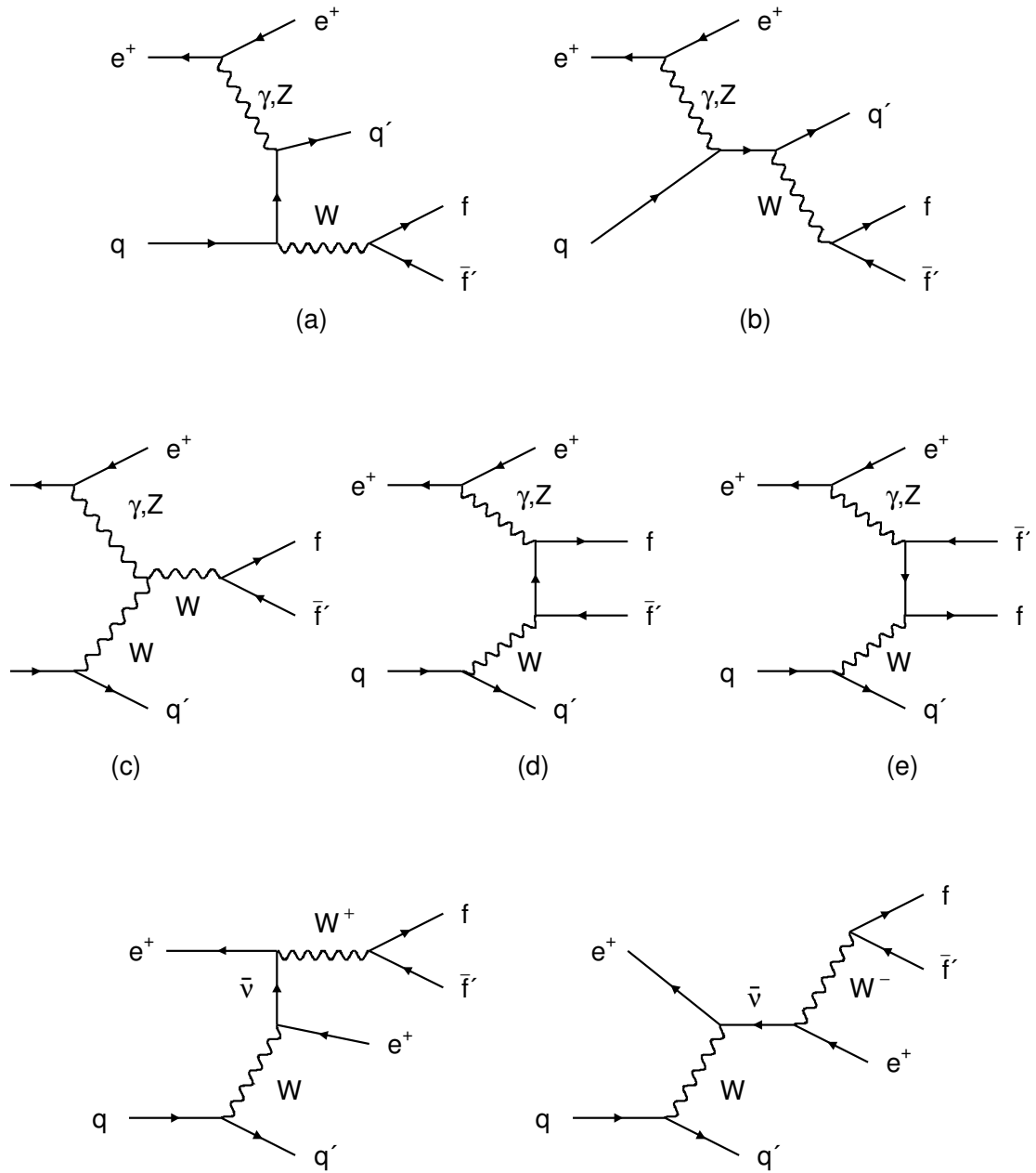


**Figure 2.9:** The main processes for  $W^\pm$  production.

## 2.8 Beyond the Standard Model

High transverse momentum final states may also arise from processes beyond the SM. They may lead to observable deviations of the data from the SM prediction. These deviations may reveal themselves as an excess or a deficit in kinematic spectra, depending on the constructive or destructive interference of the underlying processes with the SM processes. There exists a large variety of SM extensions which predict many different signatures of new physics. From the experimental point of view, a general search in all high transverse momentum final state topologies has thus probably a large potential to discover new physics. This section presents some exotic models whose predicted signatures might be in the discovery reach of HERA.

### Leptoquarks

The apparent symmetry between leptons and quarks cannot be explained within the SM. They appear in three fermion families, each consisting of three singlets and two doublets of the weak interaction. Owing to the three quark colours and the fractional electromagnetic charge of the quarks, the sum of electric charges is exactly neutralised in each generation. This charge quantisation allows an exact cancellation of anomalies arising from the so-called triangle diagrams [5]. In various unifying theories, such as Grand Unified Theories (GUTs) [18, 19, 20], Superstring inspired  $E(6)$  models [21], and in some Compositeness [22] and Technicolour [23] models, the SM gauge group is embedded into larger symmetry groups where quarks and leptons are combined into a common leptoquark multiplet.

Leptoquarks (LQs) are colour-triplet scalar or vector bosons carrying simultaneously lepton number ( $L$ ) and baryon number ( $B$ ), as well as a fractional electromagnetic charge. The coupling of a leptoquark to a lepton-quark pair can be classified according to its fermionic number  $F = L + 3B$ . Couplings to  $e^\pm q$  states yield  $|F| = 0$  or 2.

At HERA, first generation leptoquarks can be resonantly produced in the  $s$ -channel or exchanged in the  $u$ -channel. Example diagrams are shown in fig. 2.10. The  $s$ -channel production of a leptoquark could generate a resonance peak in the mass spectrum, provided that the mass of the leptoquark is smaller than  $\sqrt{s}$ . Contributions to the  $ep$  cross section would also result from  $u$ -channel exchange of a LQ and interference of LQ diagrams with SM gauge boson exchange. LQs would thus produce up- and downward deviations from the SM prediction in the mass or other kinematic spectra, predominately in the electron-jet and neutrino-jet final states. If lepton flavour violation (see below) is involved, the muon-jet and tau-jet final states are also affected. Many specific searches for leptoquarks have been performed at HERA [24, 25]. No evidence for resonance production has been found. Stringent limits have been set on the coupling strength of resonant states.

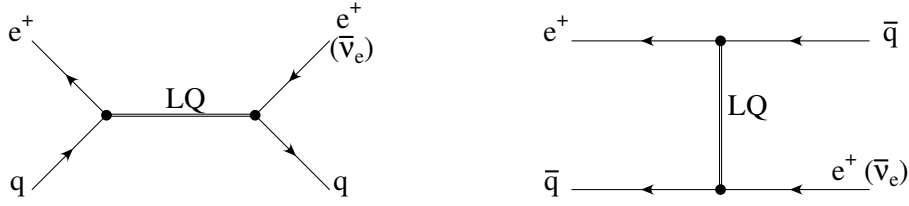


**Figure 2.10:** Processes involving a LQ. The diagram (left side) shows the production of a LQ in the  $s$ -channel, the diagram (right side) displays the exchange of a LQ in the  $u$ -channel.

### Lepton Flavour Violation

In the SM, lepton flavour is conserved. The present results of neutrino oscillation searches, however, favour minimal extensions of the SM which allow for neutrino masses and hence predict neutrino and thereby charged lepton flavour violation. Due to the smallness of the neutrino masses, the rate of lepton flavour violation (LFV) is however so low that it cannot be detected at current collider experiments. On the other hand, many extensions of the SM such as GUT theories [18, 26], models based on Supersymmetry [27, 28], Compositeness or Technicolour enhance LFV processes such that their rates may be observable. Fig. 2.11 shows a  $s$ - and an  $u$ -channel reaction involving LFV through the exchange of a LFV LQ. The final state consists basically of a high transverse momentum jet balancing a muon or tau. Similar as for non-LFV LQs, the underlying processes could yield resonance peaks in the mass spectra and produce up- and downward deviations from the SM prediction in the kinematic spectra. Searches for LFV LQ production have been performed at HERA [29]. No outstanding events have been found and the results of the searches have been used to set exclusion limits for LFV LQs.

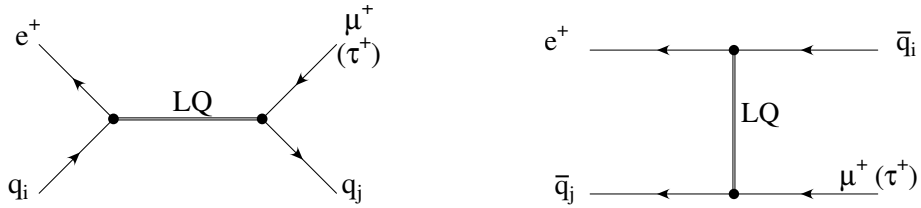


**Figure 2.11:** Processes involving Lepton Flavour Violation through the exchange of a LQ.

### Excited Fermions

If quarks and leptons are not fundamental elementary particles, but are composite objects, new interactions between quarks and leptons should appear at a scale comparable to the constituent binding energies [30]. Within these so-called compositeness scenarios, excited states of fermions may exist. An excited fermion could then transit to its ground state by radiating a SM gauge boson ( $\gamma$ ,  $Z$ ,  $W$  or  $g$ ).

At HERA, the production of excited fermions can proceed both through NC and CC interactions. Typical production and decay modes are shown in fig. 2.12. The final state consists thus basically of a known fermion and a gauge boson. Excited electrons, neutrinos and quarks have been searched for at HERA [31] via the all decay modes, *i.e.*

$$e^* \rightarrow e\gamma, eZ, \nu W$$

$$\nu^* \rightarrow \nu\gamma, \nu Z, eW$$

$$q^* \rightarrow q\gamma, qZ, qW, qg.$$

No significant deviation from the SM prediction has been found, and limits on the characteristic couplings have been derived.

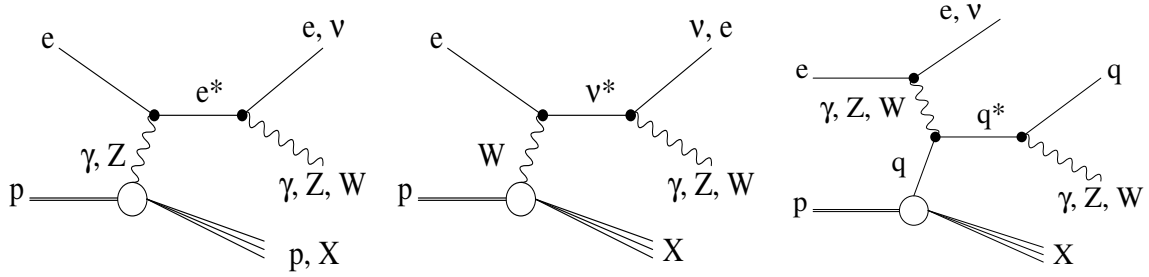


**Figure 2.12:** Typical production and decay modes of excited fermions.

### Flavour Changing Neutral Current Processes and Top Production

In the SM, the transitions between quarks of different generations can occur at tree level only through interactions involving  $W$  bosons. Transitions in flavour-changing neutral current (FCNC) processes are only possible via higher order corrections and are highly suppressed.

Especially, FCNC interactions involving the top quark, which has a mass close to the electroweak symmetry breaking scale, might produce first observable deviations from the SM. At HERA, top quarks can only be singly produced. The SM production of top quarks proceeds through the CC reaction  $ep \rightarrow \nu t \bar{b} X$  and through the FCNC interaction  $ep \rightarrow etX$ , in which a  $\gamma$  or  $Z$  is exchanged with an up-type quark from the proton yielding a top quark (see fig. 2.13). The CC reaction has a negligible cross section of less than 1 fb [32], and the FCNC reaction is, as already mentioned, highly suppressed. Several extensions of the SM, however, predict the top quark to have enhanced FCNC interactions which could lead to observable single top event rates [33]. The basic signature of a top decay is a final state with three high transverse momentum objects, formed by the  $b$ -jet from the top decay  $t \rightarrow bW$  and the leptonic or hadronic decay products of the associated  $W$  boson. Both H1 and ZEUS experiments have performed searches for single top production at HERA [34, 35]. No deviation from the SM prediction has been found. An upper limit on the cross section for single top production via FCNC processes of 0.225 pb has been derived [35].

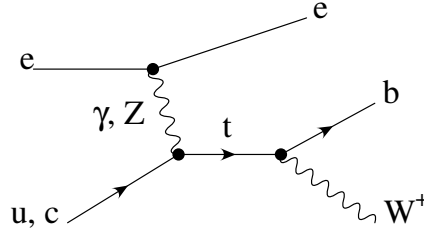


**Figure 2.13:** Anomalous single top production via a FCNC interaction.

## Supersymmetry

The supersymmetric extension of the SM provides a theory for the unification of the gauge couplings at the grand unification scale (GUT scale), while solving major problems of the SM. The so-called fine tuning problem arising from the hierarchy between the electroweak scale  $\mathcal{O}(10^2 \text{ GeV})$  and the GUT scale  $M_{\text{GUT}} \approx \mathcal{O}(10^{16} \text{ GeV})$  is solved: the quantum corrections to the Higgs mass  $M_H$  present in the SM, which are quadratically divergent with the scale  $\Lambda \approx \mathcal{O}(M_{\text{GUT}}) \gg M_H$ , are systematically removed. In Supersymmetry (SUSY), a symmetry relates fermions and bosons such that there are equal numbers of bosons and fermions with identical couplings. Each SM particle is attributed a supersymmetric partner (superpartner) with spin differing by half a unit, and both partners inhabit a common, irreducible representation of the SUSY algebra known as supermultiplet. For instance, the scalar partners of the left- and right-handed electrons  $e_L, e_R$  are the selectrons  $\tilde{e}_L, \tilde{e}_R$ , and similarly squarks  $\tilde{q}_L, \tilde{q}_R$  are the partners of quarks  $q_L, q_R$ . Moreover, all particles belonging to one supermultiplet must have equal masses. As the experimental constraints exclude the existence of e.g. a superpartner of the electron with  $M_e = 0.511 \text{ MeV}$ , SUSY must be broken. Due to the resulting mass differences between the superpartners, the systematic cancellation of the quantum corrections to the Higgs mass is affected. These corrections can however still be controlled if the characteristic scale of SUSY is below  $\mathcal{O}(1 \text{ TeV})$ . There exist many SUSY breaking models, e.g. minimal supergravity [27] and gauge mediated [36] SUSY breaking models. However, the minimal particle content of supersymmetric extensions of the SM is essentially common to all models.

Furthermore, supersymmetric particles are distinguished from SM particles by the so-called R-parity ( $R_p$ ), a multiplicative quantum number defined through  $R_p = (-1)^{3B+L+2S}$ , where  $S$  denotes the spin of the particle. It follows that  $R_p = -1$  for supersymmetric particles and  $R_p = 1$  for SM particles. If  $R_p$  is conserved, supersymmetric particles can only be produced in pairs and the lightest supersymmetric particle is stable. If  $R_p$  is violated ( $\tilde{R}_p$ ), supersymmetric particles can be singly produced and the lightest supersymmetric particle decays into SM particles.  $\tilde{R}_p$  processes are of special interest at HERA, as e.g. squarks could be resonantly produced in the  $s$ -channel via the fusion of the incoming electron and a quark from the incoming proton and could generate a resonance peak in the mass spectrum if their mass is below  $\sqrt{s}$ .

SUSY thus introduces a vast number of new particles. They could be discovered via a



resonance peak in the mass spectrum or through other constructive or destructive interference effects with SM processes. Many different final state topologies can be distinguished, e.g. an electron plus a jet or multiple jets, a neutrino plus a jet or multiple jets or an electron plus another charged lepton plus multiple jets. HERA searches for supersymmetric particles [37] have shown no evidence for a signal and their results have been used to constrain SUSY models.

### Contact Interactions

Evidence for new physics can be directly observed if new resonances are produced. The direct search is limited by kinematics to a mass range below the available centre-of-mass energy. However, effects arising from the virtual exchange of very heavy particles with masses  $\Lambda_X \gg \sqrt{s}$ , could still be detected. These indirect effects are describable as contact interactions [38], i.e. the exchange of heavy particles are reduced to a point-like four-fermion interaction, similar to the formalism proposed by Fermi to explain the beta-decay [39]. This interaction is then determined only by an effective coupling  $g_X^2/\Lambda_X^2$ . Contact interactions can naturally explain a possible compositeness of leptons and quarks. Their indirect effects could be observable in searches for new phenomena, e.g. in NC interactions, the cross section would increase at high  $Q^2$ -values, while the constructive or destructive interference of the new heavy particles with SM  $\gamma$  or  $Z$  bosons would modify the cross section in the intermediate  $Q^2$  region. Dedicated searches have been performed at HERA resulting in exclusion limits on the compositeness scale  $\Lambda_X$  [40].

### Extra Dimensions

The hierarchy problem in the SM arising from the huge difference between the electroweak scale and the gravity scale is solved in many theories embedding the SM into higher symmetry gauge groups, like for instance SUSY. Alternatively, one may generate the hierarchy by the geometry of additional dimensions, which means that our three spatial dimensions form only a subspace of a much larger extra dimensional space. Gravity may thus propagate through a higher dimensional volume, in contrast to the other forces, which are confined to our three-spatial-dimensional subspace, and it may lead to effects at the TeV scale observable at high-energy colliders. The latter effects are predicted by different scenarios based on distinct phenomenology, e.g. the large extra dimensions scenario [41]. The virtual graviton exchange could for instance interfere with ordinary  $\gamma$  and  $Z$  exchange and modify the cross sections of SM processes or lead to the exchange of new heavy gauge bosons, the so-called Kaluza-Klein gauge bosons. Results from HERA experiments on the search for virtual graviton exchange are given in ref. [40].

### New Massive Gauge Bosons

New massive and electrically charged or neutral gauge bosons are predicted in most extensions of the SM. They can also arise in theories involving extra dimensions. Whatever the source, a charged gauge boson is denoted  $W'$  and a neutral gauge boson  $Z'$ . A  $W'$  always couples to different

flavours and is in particular a leptoquark gauge boson if it couples a lepton and a quark. The existence of these new bosons is strongly motivated in left-right symmetric models [26, 42, 43]. These models intend to naturally explain the parity violation in weak interactions. Moreover, they predict two charged gauge bosons ( $W_R^\pm$ ) and one neutral gauge boson ( $Z_R$ ) coupling to right-handed fermions. At HERA, a  $W_R$  can imply the production of a new heavy and unstable right-handed neutral lepton or the modification of the CC cross section via interference effects.

### Doubly Charged Higgs Boson

In some extensions of the SM, namely the left-right symmetric models, new right- and left-handed Higgs boson triplets  $H_{R,L} = (H_{R,L}^0, H_{R,L}^+, H_{R,L}^{++})$  are introduced which act solely in the leptonic sector [44]. The incorporation of two triplets preserves the left-right symmetry in these models. Particularly the right-handed triplet is responsible for the symmetry breaking of  $SU(2)_R$  and the mass generation of the right-handed Majorana neutrinos through the seesaw mechanism. The doubly charged Higgs boson offers an almost background free search channel since it decays into an equally charged lepton pair. The corresponding resonance would give rise to a narrow peak in the mass spectra of multi-lepton final states. The coupling and the mass of a doubly charged Higgs boson have been constrained at HERA [45].

## 2.9 Monte Carlo Generators

The Monte Carlo technique allows for a comparison of the measured data with the theory, the determination of acceptances, efficiencies, as well as resolution effects due to detector constraints. It can moreover be used to estimate background contributions and is indispensable for the tuning of the cuts which separate background and signal. Monte Carlo models are used to generate events, *i.e.* they provide the four-momenta of all partons emerging from the hard scattering. Further higher order effects are taken into account by applying *e.g.* the parton shower model. The non-perturbative fragmentation of the partons to colourless hadrons is simulated by hadronisation models. Finally, the full detector response to the particles is simulated using the H1 simulation package based on the GEANT [46] program. A brief description of the Monte Carlo programs used in this work will be given in the following.

### Neutral Current DIS (RAPGAP)

Event rates from neutral current deep inelastic scattering are calculated using the RAPGAP [47] model. It uses the exact matrix elements for the simulation of  $\mathcal{O}(\alpha_s)$  processes. The QED radiative effects arising from single photon emission off the lepton line and virtual electroweak corrections are simulated with the HERACLES [48] event generator. Higher order QCD effects are taken into account by using the leading logarithmic parton shower approach. The CTEQ5L [49] PDFs have been chosen for the proton to evaluate the nominal NC cross section.

### Charged Current DIS (DJANGO)

SM CC event rates are calculated with the LEPTO [50] program interfaced to HERACLES via the event generator DJANGO [51]. The HERACLES program includes first order electroweak corrections, as explained in the previous paragraph. Parton cascades are modelled with the Colour Dipole Model in ARIADNE [52]. The CTEQ5L PDFs have been chosen to evaluate the nominal CC cross section.

### Photoproduction of Jets and Prompt Photons (PYTHIA)

The direct and resolved photoproduction of jets and prompt photons are modelled with the PYTHIA [53] event generator. It contains the Born level QCD matrix elements. Higher order QCD effects are accounted for by leading logarithmic parton showers. Multiple interactions between the proton and the resolved photon are included through additional interactions between spectator partons within the same event. Both light and heavy flavours have been generated. The hadronisation of the outgoing partons is based on the Lund String model [54]. The GRV LO [55] PDFs have been chosen for the photon and the CTEQ5L PDFs for the proton.

### QED Compton Scattering (WABGEN, RAPGAP)

Elastic and quasi-elastic Compton processes are simulated with the WABGEN [56] generator. The corresponding cross section is numerically calculated using the Monte Carlo package BASES [57]. The deep inelastic contribution is already included in the used NC DIS model RAPGAP.

### Multi-Lepton Production (GRAPE)

Multi-lepton events are generated with the GRAPE [58] model. The cross section calculation is based on the exact matrix elements in the electroweak theory at tree level. The dilepton productions via  $\gamma\gamma$ ,  $\gamma Z$ ,  $ZZ$  collisions, internal photon conversion and via the decay of virtual and real  $Z$  bosons are taken into account. The automatic calculation system GRACE [59] provides the relevant Feynman amplitudes, whereas the fragmentation and hadronisation processes are simulated using the SOPHIA [60] program for the quasi-elastic processes and PYTHIA for the deep inelastic regime. Initial and final state radiation processes (QED and QCD parton showers) are simulated in leading logarithmic approximation. The resolved Drell-Yan process and bremsstrahlung from the proton are not included.

### $W$ Production (EPVEC)

The SM prediction for  $W$  production via  $ep \rightarrow eW^\pm X$  is calculated by using a next to leading order (NLO) QCD calculation [61] in the framework of the EPVEC [17] event generator. Each event generated by EPVEC according to its default LO cross section is weighted by a factor dependent on the transverse momentum and rapidity of the  $W$  [62], such that the resulting cross

section corresponds to the NLO calculation. The ACFGP [63] and CTEQ4M [64] PDFs have been chosen for the photon and the proton, respectively. The renormalisation scale is taken to be equal to the factorisation scale and is fixed to the  $W$  boson mass. Final state parton showers are simulated using the PYTHIA framework [65].

The NLO corrections are found to be of the order of 30% at low  $W$  transverse momenta (resolved photon interactions) and typically 10% at high  $W$  transverse momenta (direct photon interactions) [61]. The NLO calculation reduces the theory error from 30% at LO to 15%. The charged current process  $ep \rightarrow \nu W^\pm X$  is calculated with EPVEC and found to contribute less than 7% to the total  $W$  production cross section [4]. The total predicted  $W$  production cross section amounts to 1.1 pb for an electron-proton centre-of-mass energy of  $\sqrt{s} = 301$  GeV and 1.3 pb for  $\sqrt{s} = 319$  GeV.

### **$Z$ Production (GRAPE, EPVEC)**

$Z$  production with subsequent leptonic and hadronic decays of the  $Z$  boson is simulated with the GRAPE and EPVEC generators, respectively.

---

# H1 Experiment at HERA

---

## 3.1 HERA Collider

The electron-proton storage ring HERA at DESY<sup>1</sup> [66] is a unique facility to study high energy electron-proton collisions and to search for possible new physics.

During the first data taking period 1994–1997 at HERA, positrons of 27.5 GeV energy collided with protons of 820 GeV energy. In 1998 and the beginning of 1999 the lepton beam consisted of electrons and the proton energy was increased to 920 GeV. Since mid of 1999 until the end of the HERA I data taking period in autumn 2000 HERA was again operated with positrons. The centre-of-mass energy amounts to 301 (319) GeV for a proton energy of 820 (920) GeV.

The layout of the HERA accelerator and its pre-accelerators facilities is shown in fig. 3.1. The accelerator ring has a circumference of 6.3 km and is 10 m – 25 m under ground. It consists of two separate storage rings for the electron and proton beams. The electron ring is partly made of superconducting cavities and conducting magnets operating at room temperature. The proton ring has conventional radio frequency cavities and superconducting magnets providing a 4.68 Tesla magnetic field. The beam particles are stored in up to 220 bunches with  $10^{10} - 10^{11}$  particles each. Two subsequent bunch crossings are separated in time by 96 ns, corresponding to a bunch crossing frequency of 10.4 MHz.

In total, there exist four interaction points spaced evenly around the HERA tunnel. Electron-proton collisions take place in the two general purpose detectors H1 [67] and ZEUS [68]. In addition, there are two fixed target experiments, HERA-B [69] and HERMES [70], which use only the proton and the electron beam, respectively.

---

<sup>1</sup>Deutsches Elektronen-Synchrotron

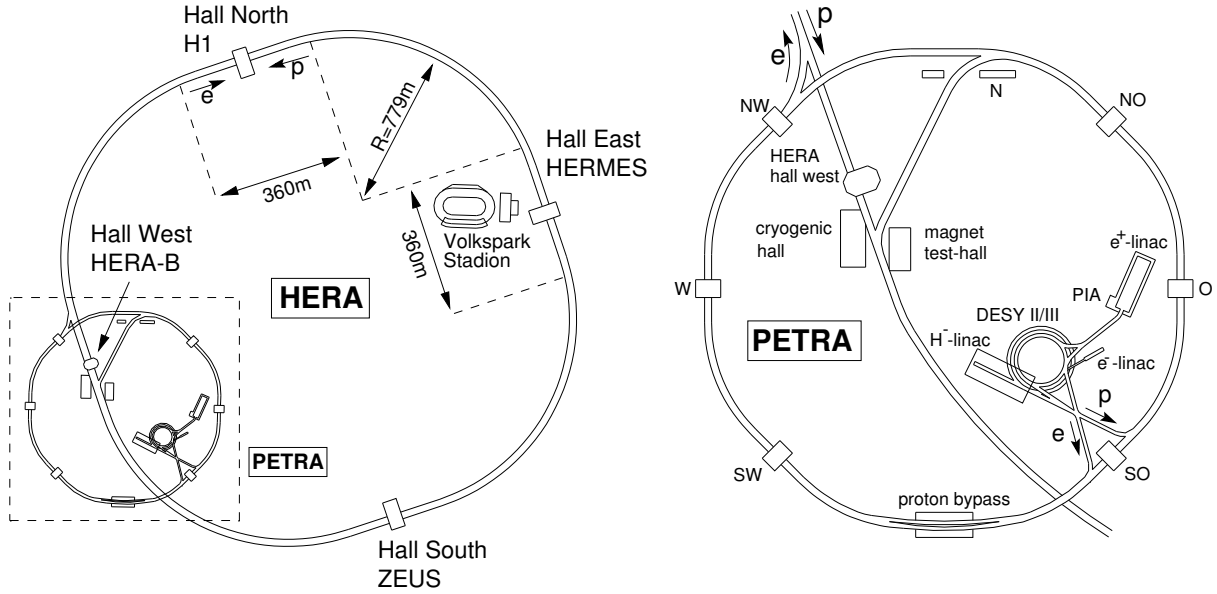


Figure 3.1: The electron-proton collider HERA and its pre-accelerators.

## 3.2 H1 Detector

The H1 detector (fig. 3.2) is a multipurpose apparatus built to measure the complete final state in  $ep$  collisions. The imbalance of the beam energies boosts the  $ep$  centre-of-mass in the proton direction and therefore requires an asymmetric detector configuration. The right-handed coordinate system is centred at the nominal interaction point ( $z = 0$ ) and defines the positive  $z$ -direction along the incident proton beam. The positive  $x$ -axis points to the ring centre, the positive  $y$ -axis points in the upward direction. The polar angle  $\theta$  is defined with respect to the positive  $z$ -axis and the azimuthal angle  $\phi$  such that  $\phi = 0^\circ$  points to the positive  $x$ -axis. An overview of the main components relevant to this analysis is given in the following. A detailed description can be found in ref. [67].

### 3.2.1 Calorimetry

The calorimetry system consists of the main calorimeter (liquid argon (LAr) calorimeter), the backward calorimeter (backward electromagnetic calorimeter (BEMC)/ spaghetti calorimeter (SpaCal)), the forward calorimeter (PLUG), the outer calorimeter (tail catcher) and the very backward calorimeter (electron tagger).

#### Liquid Argon Calorimeter

The LAr calorimeter covers the polar angle range  $4^\circ < \theta < 154^\circ$ . It is located inside the superconducting coil in order to minimise the passive material and provide a good electron recognition

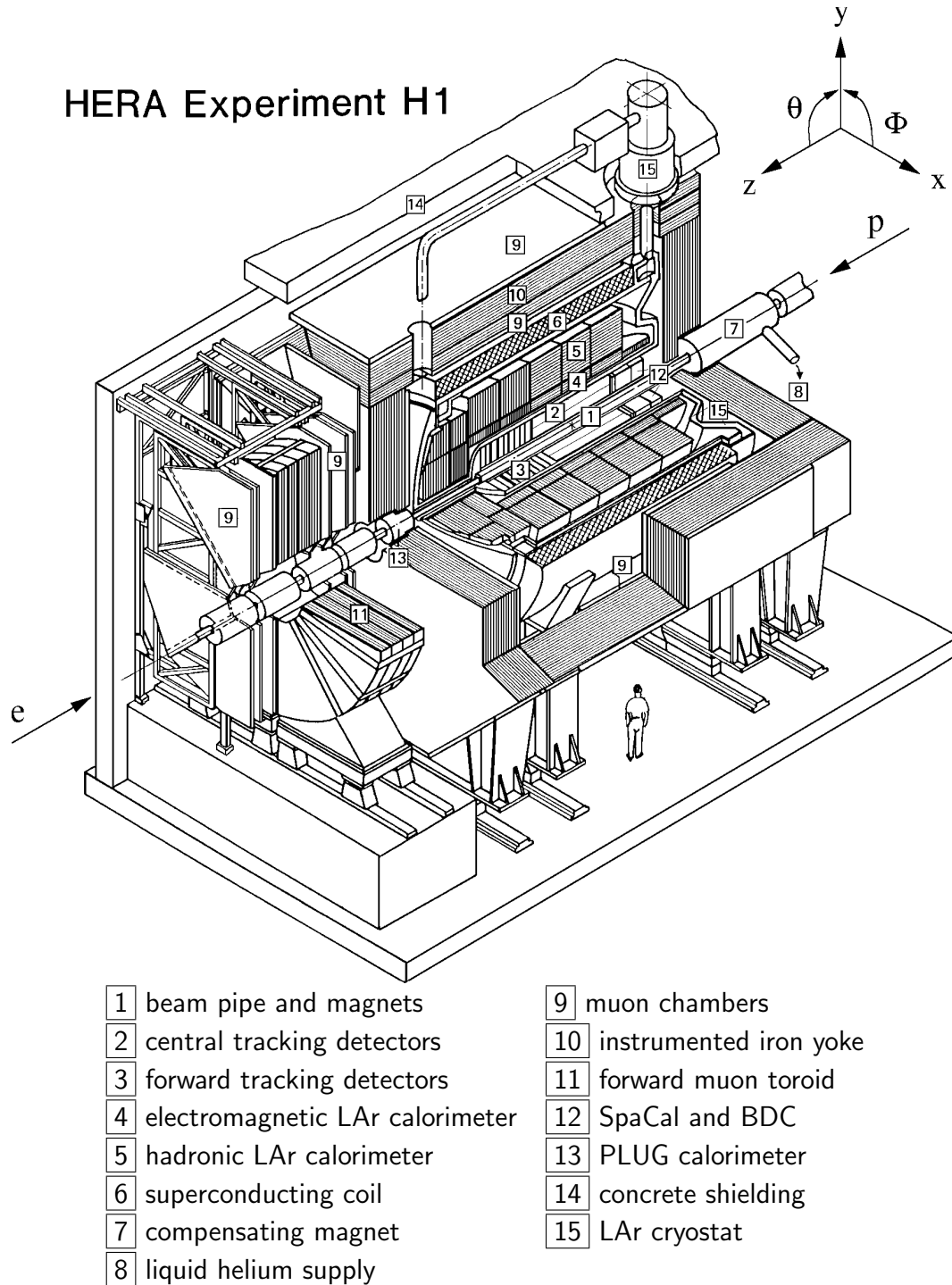


**Figure 3.2:** An isometric view of the H1 detector.

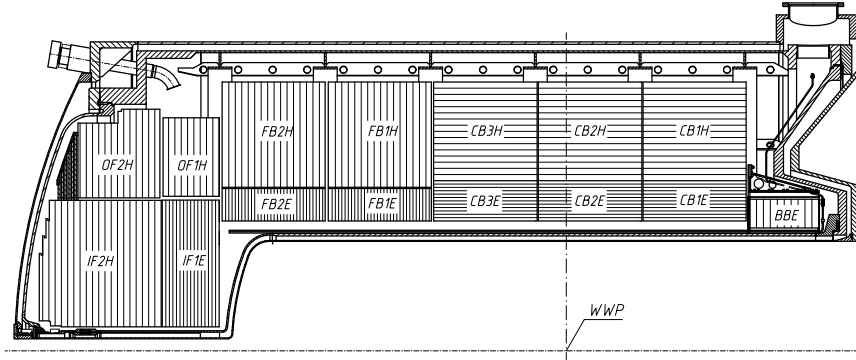


**Figure 3.3:** Side view of the liquid argon calorimeter. It is segmented along the beam axis into eight wheels, labelled BBE, CB1, CB2, CB3, FB1, FB2, OF and IF.

as well as a precise measurement of electromagnetic and hadronic energies. Liquid argon was chosen because of its good stability, ease of calibration, possibility of fine granularity and homogeneity. The calorimeter is segmented along the beam axis into eight wheels (see fig. 3.3), each of them being further subdivided into octants in  $\phi$ . The inner section of the calorimeter is dedicated to the measurement of electromagnetic energy. The outer part comprises the hadronic section. The electromagnetic and hadronic sections are laminated with lead and stainless steel absorber plates, respectively, and both are filled with liquid argon as active material. The calorimeter is 5 to 8 hadronic interaction lengths deep, depending on the polar angle and has an electromagnetic section which is 20 to 30 interaction lengths deep. The energy resolution measured in test beams [71] is  $\sigma(E)/E \approx 12\%/\sqrt{E(\text{GeV})}$  for an electromagnetic shower and  $\sigma(E)/E \approx 50\%/\sqrt{E(\text{GeV})}$  for a hadronic shower. The electromagnetic and hadronic energy scale uncertainties are 0.7 – 3% (see sec. 4.5) and 2% (see sec. 4.6), respectively. The LAr calorimeter is non-compensating, *i.e.* the response to hadrons is about 30% lower than the response to electrons of the same energy. An off-line reweighting technique is used to equalise the response and provide an optimal energy resolution.

## BEMC and SpaCal

The backward region of the LAr calorimeter was complemented with the BEMC, which covers the polar angle range  $151^\circ < \theta < 176^\circ$ . This electromagnetic lead-scintillator sandwich calorimeter was replaced in the 1994–95 shutdown by the SpaCal, a scintillating-fibre calorimeter with lead absorbers [72]. It covers the angular region  $153^\circ < \theta < 177.8^\circ$  close to the beam pipe, and provides high angular and energy resolutions for electrons, as well as the measurement of hadronic energy. The electromagnetic energy resolution is  $\sigma(E)/E \approx 7.1\%/\sqrt{E(\text{GeV})}$  [73]. Hadronic energies are measured with a resolution of  $\sigma(E)/E \approx 30\%/\sqrt{E(\text{GeV})}$ . The hadronic energy scale of the SpaCal is known to 5% [9].



### Tail Catcher

The inner calorimeters are supplemented on the outside by an iron return yoke. It is instrumented with up to sixteen streamer tube layers, some being equipped with strip electrodes to measure penetrating single ionising tracks, or pad electrodes, which measure energy leaking out of the inner calorimeters (tail catcher). In this work, the tail catcher is mainly used for muon detection (see sec. 3.2.3).

### PLUG

The PLUG calorimeter covers the angular range  $0.7^\circ < \theta < 3.3^\circ$ , complementing the calorimetry system in the forward direction. It is not used in this analysis.

### Electron Tagger and Luminosity Measurement

The electron tagger is located beside the electron beam pipe at  $z = -33.4$  m covering the angular range  $\theta > 179.7^\circ$ . It detects electrons at very low scattering angles and is part of the luminosity system. The luminosity is determined separately for each run<sup>2</sup> by measuring the large and precisely known cross section of the elastic bremsstrahlung process  $ep \rightarrow ep\gamma$  (Bethe-Heitler, see sec. 2.4). The final state photon is detected in coincidence with the final state electron by the photon detector situated at  $z = -102.9$  m.

## 3.2.2 Inner Tracking System

The inner tracking system consists of the two central jet chambers (CJC1 and CJC2), central inner and outer trackers for measuring the  $z$ -coordinate (CIZ and COZ), central multiwire proportional chambers (CIP and COP), forward (FTD) and backward (BPC/BDC) tracking detectors and central and backward silicon microvertex detectors (CST and BST). The tracking system is surrounded by the calorimeters and the superconducting coil, which provides a uniform magnetic field of 1.15 Tesla along the  $z$ -direction for momentum measurement. Fig. 3.4 shows an overview of the main components of the inner tracking system, which are now briefly discussed.

### Central Tracking System

Fig. 3.5 shows a transverse section through the central tracking system. The CJC consists of two concentric cylindrical drift chambers, coaxial with the beam-line, with a polar angle coverage of  $15^\circ < \theta < 165^\circ$ . The spatial resolution is  $170 \mu\text{m}$  in the  $r - \phi$  plane, the  $z$ -coordinate is measured with an accuracy of  $\sigma_z = 22 \text{ cm}$ . The transverse momentum  $P_T$  of charged tracks

<sup>2</sup>A fresh filling of the electron and proton bunches into the HERA ring is called luminosity fill. A luminosity fill is further subdivided into so-called runs, which last at maximum two hours each. The quality of a run is characterised as good, medium, bad or unknown, depending on the detector conditions.

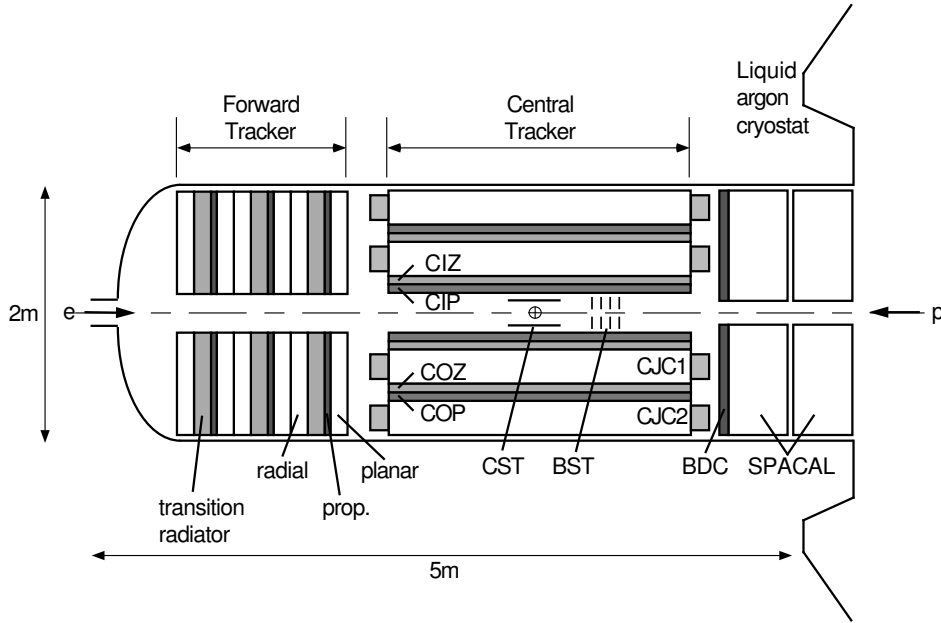


**Figure 3.4:** Schematic overview of the inner tracking system.

can be determined from their curvature in the magnetic field with a momentum resolution of  $\sigma(P_T)/P_T^2 < 0.005 \text{ GeV}^{-1}$ .

Two thin drift chambers (CIZ and COZ) have sense wires perpendicular to the beam axis which provide a precise measurement of the  $z$ -coordinate ( $\sigma_z \approx 350 \mu\text{m}$ ). Each of the  $z$ -chambers is supported by the proportional chambers (CIP and COP), which deliver a fast trigger signal. The CST builds the innermost part of the tracking system and was fully commissioned in 1997. It covers a polar angle range from  $30^\circ < \theta < 150^\circ$  and measures track trajectories with a high precision. The CST information is used to achieve a higher accuracy in the determination of track quantities and the vertex position.

### The Forward Tracking System

The FTD covers the polar angle range  $7^\circ < \theta < 25^\circ$  and consists of three supermodules. Each supermodule includes three planar drift chambers, rotated to each other by  $60^\circ$  in azimuth, a multiwire proportional chamber, a transition radiation detector region and a radial drift chamber.

### The Backward Tracking System

The backward proportional chamber (BWPC) measures the angle of the electron in the range  $155^\circ < \theta < 174^\circ$ . The BWPC has been replaced in the 1994–95 shutdown by an eight layer drift chamber (BDC), which extends the polar acceptance to  $155.1^\circ < \theta < 177.5^\circ$ .

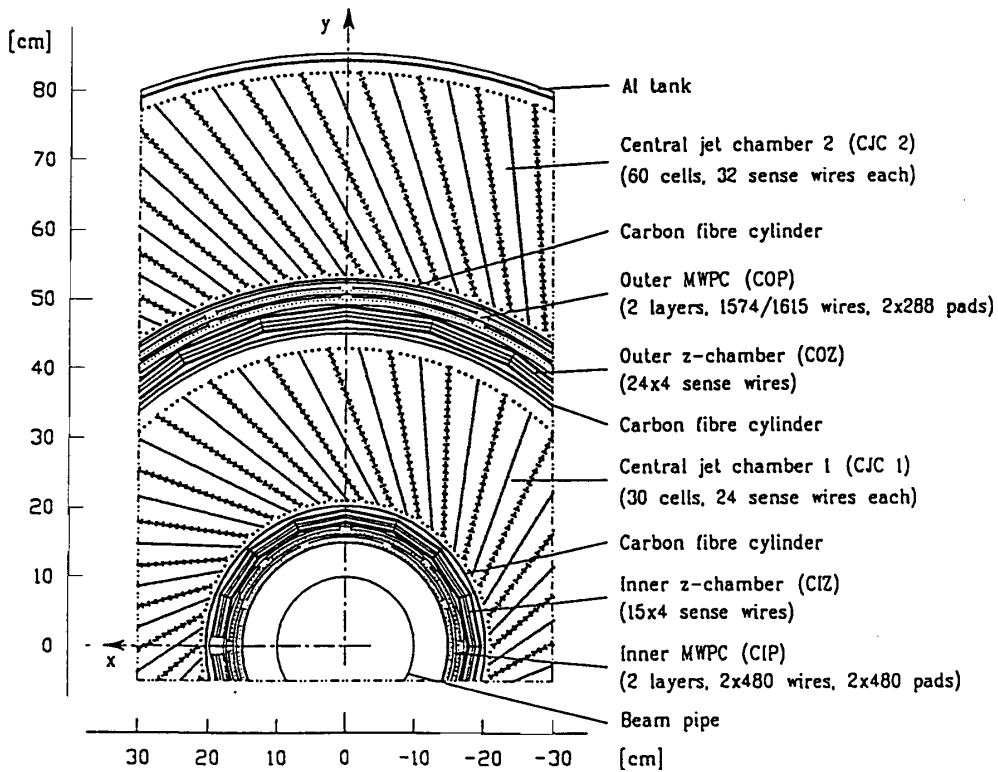


Figure 3.5: Transverse section through the central tracking system.

### 3.2.3 Muon Detectors

The muon system consists of the central muon detector, which surrounds all major detector components, and the forward muon detector.

#### Central Muon Detector

The central muon detector covers the polar angle range  $5^\circ < \theta < 175^\circ$  and is implemented in the iron yoke, which is divided into 64 modules. Each module is instrumented with 10 layers of streamer tubes and may be bordered, by three additional layers of streamer tubes (inner and outer muon boxes, respectively). Fig. 3.6 shows the structure of a module. Penetrating tracks are reconstructed from their hit pattern in the streamer tubes. The signal wires in the streamer tubes provide a measurement of the muon position perpendicular to the wires with an accuracy of 3 to 4 mm. The position parallel to the wires is measured by strip electrodes present in five of the streamer tubes with a resolution of 10 to 15 mm. Some of the layers inhabit additional pad electrodes, which can measure the deposited energy and improve the track measurement. The instrumented iron is also used as a backing calorimeter to measure the energy of hadrons which are not fully absorbed in the inner calorimeters (see also sec. 3.2.1).

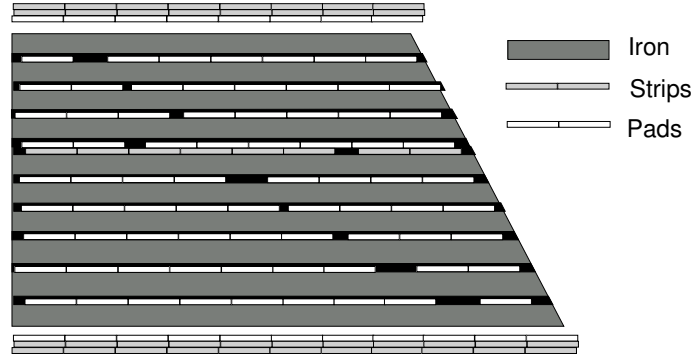


**Figure 3.6:** A module of the central muon detector.

### Forward Muon Detector

The forward muon detector complements the muon detection in the angular range  $3^\circ \leq \theta \leq 17^\circ$ . It consists of six double layers of drift chambers, three mounted on either side of a toroidal magnet, which provides a magnetic field of roughly 1.6 Tesla. The drift chamber planes are oriented such that four (two) of the planes essentially measure the polar (azimuthal) angle. Due to energy losses in the inner detectors and the toroid, only muons with a momentum above 5 GeV can be detected.

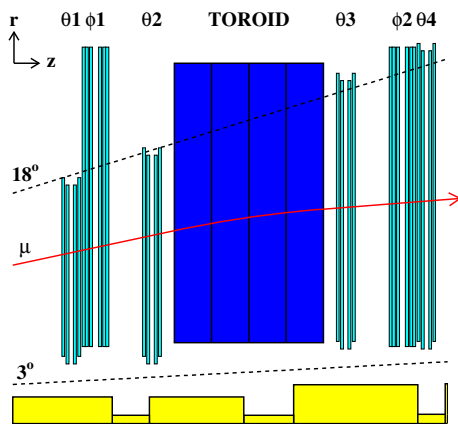


**Figure 3.7:** Schematic view of the forward muon detector. The drift chambers are labelled  $\theta_1 - \theta_4$  and  $\phi_1 - \phi_2$ .

### 3.2.4 H1 Trigger System

The trigger system is able to provide a fast separation of interesting physics events from background events. The rate of background events is about 50 kHz for proton interactions with gas in the beam pipe (beam-gas) and with material of the beam tube (beam-wall). Beam-halo muons and muons from cosmic showers also contribute. In contrast, the rate of physics processes is

much smaller, reaching from tagged photoproduction with a rate of 20 – 30 Hz to rare processes at high transverse momenta, which occur only a few times per day or week.

The H1 Trigger System is based on four levels (L1 to L4) in order to filter the interesting events. The L1 trigger system decides within  $2\ \mu\text{s}$  whether an event should be kept or not by using the information of different subdetectors (trigger elements). The central trigger logic combines these trigger elements to 128 subtriggers. The L2 trigger system reaches a decision within  $20\ \mu\text{s}$  by utilising neural networks and topological correlations. The L3 trigger system has not yet been used in H1. The L4 trigger system is based on a fast event reconstruction using the whole detector information. The events accepted by L4 are written to tape with a rate of about 15 Hz.



---

# General Search for New Phenomena

---

## 4.1 Introduction

At HERA electrons and protons collide with a centre-of-mass energy of up to 319 GeV. The high centre-of-mass energy and the unique types of colliding particles provide an ideal testing ground for the Standard Model (SM). The H1 experiment at HERA has accumulated data corresponding to more than  $100 \text{ pb}^{-1}$  of integrated luminosity in the HERA I data taking period (1994–2000) consisting of  $e^+p$  collisions recorded at  $\sqrt{s} = 301 \text{ GeV}$  and  $\sqrt{s} = 319 \text{ GeV}$ , as well as  $e^-p$  collisions recorded at  $\sqrt{s} = 319 \text{ GeV}$ . During the last decades a large variety of extensions of the SM have been constructed. They predict many different new phenomena at high energies or large transverse momenta. The HERA I data has been used to test some of these models and upper limits on cross sections of new processes have been derived. These analyses have been optimised to detect the anticipated experimental signatures of the extensions.

A complementary approach is described in this work, consisting in a broad-range search for deviations from the SM prediction at large transverse momentum ( $P_T$ ). The analysis covers phase space regions where the SM prediction is sufficiently precise to detect anomalies and does not rely on assumptions concerning the characteristics of the SM extension. Such a model-independent search might therefore also discover unexpected manifestations of new physics. To fully exploit the discovery potential, all high  $P_T$  final state configurations are systematically investigated. A related strategy for a model-independent search was presented by the D0 collaboration [74, 75, 76].

In this work, all final states are analysed having at least two objects with a transverse momentum above 20 GeV and lying in the polar angle range  $10^\circ < \theta < 140^\circ$ . The considered objects are electron ( $e$ ), muon ( $\mu$ ), photon ( $\gamma$ ), jet ( $j$ ) and neutrino ( $\nu$ )<sup>1</sup>. Moreover, the objects are required to be isolated versus each other by a minimum distance  $R = \sqrt{(\Delta\eta)^2 + (\Delta\phi)^2}$  of 1 unit in the pseudorapidity<sup>2</sup>-azimuth ( $\eta - \phi$ ) plane. In order to avoid bias, the object phase space requirements have been defined a priori and no additional criteria (except topological back-

---

<sup>1</sup>In this chapter, “neutrino ( $\nu$ )” refers to non-interacting particles in general.

<sup>2</sup>The pseudorapidity  $\eta$  is a function of the polar angle:  $\eta = -\log(\tan(\theta/2))$ .

ground finding) enter the event selection. The object quality criteria are defined according to our knowledge of SM processes and detector performances. The analysis uses the complete HERA I data sample corresponding to an integrated luminosity of  $115.3 \text{ pb}^{-1}$ . All selected events are then classified into exclusive event classes (e.g.  $e$ - $j$ ,  $j$ - $j$  and  $j$ - $\nu$  event classes) according to the number and types of objects detected in the final state. Exclusive event classes ensure a clear separation of final states and an unambiguous statistical interpretation.

In a first step, the global event yields of all measurable event classes are compared to the SM expectation. Selection efficiencies are derived to quantify the finding potential and are helpful to set rough exclusion limits for new physics signals. Moreover, the fraction of properly reconstructed events is given per event class to estimate the purity of the selections.

In a second step, the invariant mass  $M_{\text{all}}$  and the scalar sum of transverse momenta  $\sum P_T$  of high  $P_T$  final state objects are investigated. A new algorithm is used to search for the largest deviation from the SM prediction in these distributions. Finally, the likelihood to find the deviation with the algorithm in a given event class and in all studied event classes is derived.

## 4.2 Standard Model Expectation

A search for deviations from the SM requires a precise and reliable estimate of all relevant processes. Hence, several Monte Carlo (MC) programs are used to generate a large number of events in all event classes, carefully avoiding double-counting of processes. All events were passed through a full detector simulation as described in sec. 2.9. All processes were generated with an integrated luminosity  $L_{\text{int}}$  at least 8 times higher than the one of the data in the considered phase space and up to 100,000 times higher at very high  $P_T$ .

Tab. 4.1 presents the MC sets generated for and used in this analysis. The specific processes and the corresponding models are described in sec. 2.9. The statistical uncertainty at high  $P_T$  and  $M_{\text{all}}$  is reduced by generating events especially for the relevant phase space regions. The PYTHIA samples have been generated for different values of the transverse momentum  $\hat{P}_T$  of the particles emerging from the subprocess, the DJANGO and RAPGAP samples for different  $Q^2$  values and the WABGEN sample for different values of the invariant mass  $M_{e\gamma}$  of the electron and photon involved in the QED Compton process. The GRAPE sample has been separately generated for each lepton pair flavour ( $ee$ ,  $\mu\mu$  and  $\tau\tau$ ). The EPVEC sample consists of  $L_{\text{int}} = 200 \text{ fb}^{-1}$  for the leptonic  $W$  decay ( $W \rightarrow l\bar{l}'$ ) and  $L_{\text{int}} = 200 \text{ fb}^{-1}$  for the hadronic decay ( $W \rightarrow q\bar{q}'$ ).

The prediction of processes with two or more high transverse momentum jets (e.g.  $ep \rightarrow jj$ ) is scaled by a factor of 1.2 to re-weight the normalisation of the LO Monte Carlos to that of NLO QCD calculations [77].



Process(es)	Model	Phase Space/ Subprocess	$L_{\text{int}}/\text{fb}^{-1}$
Photoproduction	PYTHIA	$\hat{P}_T > 10 \text{ GeV}$	0.2
		$\hat{P}_T > 15 \text{ GeV}$	2
		$\hat{P}_T > 25 \text{ GeV}$	20
		$\hat{P}_T > 40 \text{ GeV}$	20
		$\hat{P}_T > 75 \text{ GeV}$	300
		$\hat{P}_T > 95 \text{ GeV}$	10000
Prompt Photon Production	PYTHIA	$\hat{P}_T > 10 \text{ GeV}$	11
		$\hat{P}_T > 20 \text{ GeV}$	70
		$\hat{P}_T > 40 \text{ GeV}$	3000
Neutral Current DIS	RAPGAP	$Q^2 > 4 \text{ GeV}^2$	0.8
		$Q^2 > 100 \text{ GeV}^2$	0.8
		$Q^2 > 400 \text{ GeV}^2$	3.1
		$Q^2 > 1000 \text{ GeV}^2$	2.4
		$Q^2 > 5000 \text{ GeV}^2$	19
		$Q^2 > 10000 \text{ GeV}^2$	100
		$Q^2 > 20000 \text{ GeV}^2$	1100
Charged Current DIS	DJANGO	$Q^2 > 100 \text{ GeV}^2$	9
		$Q^2 > 10000 \text{ GeV}^2$	450
Lepton Pair Production	GRAPE	$ee$	60
		$\mu\mu$	100
		$\tau\tau$	200
QED Compton Scattering	WABGEN	$M_{e\gamma} > 10 \text{ GeV}$	3.4
		$M_{e\gamma} > 50 \text{ GeV}$	124
		$M_{e\gamma} > 100 \text{ GeV}$	1900
$W$ Production	EPVEC	$W \rightarrow l\bar{l}'$	200
		$W \rightarrow q\bar{q}'$	200

**Table 4.1:** List of Monte Carlo sets used in this analysis. Most of the samples have been generated particularly for this study.

### 4.3 Data Selection

The data selection requires at least one isolated electromagnetic cluster, muon or jet to be found anywhere in the used detector components. Only runs with good and medium quality where all essential subsystems were operational are selected. To reduce several kinds of background events, it is demanded that the event vertex is reconstructed within 35 cm of the nominal  $z$ -position of the vertex<sup>3</sup> ( $z_{\text{vertex}}$ ) and that  $\sum_i E_i - P_{z,i} < 75$  GeV, where  $E_i$  is the energy and  $P_{z,i}$  is the  $z$ -component of the particle momentum. The index  $i$  runs over all hadronic objects, electromagnetic clusters and muons found in the event. Due to energy-momentum conservation, a typical HERA event is expected to have a value of  $\sum_i E_i - P_{z,i} = 55$  GeV if the complete final state has been detected or if only longitudinal momentum along the proton direction has been undetected.

Furthermore, the event timing  $T_0$  is required to be consistent with the HERA clock within the interval  $|\Delta T_0| < 11.4$  ns, and the H1 software package QBGFMAR [78] is used to tag non-collision background. QBGFMAR provides 26 background finders to identify cosmic and beam-halo events. Depending on the event class, different background finder bits are used. In particular in the  $\mu$  event classes, the background finders are very inefficient [79] and thus not considered. Finally, the basic event selection criteria are summarised in tab. 4.2.

good, medium runs full functionality of subsystems: LAr, SpaCal, CJC1 and CJC2, CIP and COP, central muon detector, luminosity system
$-36 \text{ cm} < z_{\text{vertex}} < 34 \text{ cm}$ in 1994–1997 data sample $-35 \text{ cm} < z_{\text{vertex}} < 35 \text{ cm}$ in 1998–2000 data sample
$\sum_i E_i - P_{z,i} < 75 \text{ GeV}$
$ \Delta T_0  < 11.4 \text{ ns}$
event must be classified into one event class (as defined in sec. 4.4)
QBGFMAR bits 0 – 8 false for all event classes (except $\mu$ event classes) QBGFMAR bits 0 – 9 false for all $\nu$ event classes (except $\mu$ event classes) all 26 QBGFMAR bits false for $j$ - $\nu$ and $\nu$ - $\gamma$ event classes

**Table 4.2:** *The event selection criteria.*

### Luminosity Determination

The integrated luminosities as determined for this analysis are presented in tab. 4.3. Starting from the total raw luminosity, the restriction of the run quality to good and medium, the correction for the functionality of the subsystems (HV correction) and for satellite bunches ( $z_{\text{vertex}}$  correction) lead to a total integrated luminosity of  $115.3 \text{ pb}^{-1}$  for the 1994–2000 data sample.

<sup>3</sup>This is not required for the event classes containing only photons.

Fig. 4.1 displays the number of selected events per luminosity interval as a function of the accumulated luminosity for the 1994–1997 data sample (left side) and for the 1998–2000 data sample (right side). The selection is stable over the entire data taking period. The drop in the distribution for the 1998–2000 data sample between  $26 \text{ pb}^{-1}$  and  $34 \text{ pb}^{-1}$  is due to broken wires in the CJC in the second part of the 1999  $e^+$  run period. The inefficiencies of the CJC are, however, accounted for by the MC simulation.

Period	$L_{\text{int}}$ total raw	$L_{\text{int}}$ run quality	$L_{\text{int}}$ HV correction	$L_{\text{int}}$ $z_{\text{vertex}}$ correction
1994 $e^+$	3.17	3.02	2.86	2.73
1995 $e^+$	5.88	5.27	4.43	4.26
1996 $e^+$	9.83	9.60	8.11	7.51
1997 $e^+$	27.92	24.53	22.72	21.23
1998 $e^-$	5.71	4.54	3.24	3.15
1999 $e^-$	15.73	14.81	10.85	10.54
1999 $e^+$	24.78	23.36	19.30	18.22
2000 $e^+$	59.26	56.02	49.91	47.63

**Table 4.3:** Integrated luminosities from 1994 to 2000 in  $\text{pb}^{-1}$ . The total and final integrated luminosity from 1994 to 2000 amounts to  $115.3 \text{ pb}^{-1}$ .

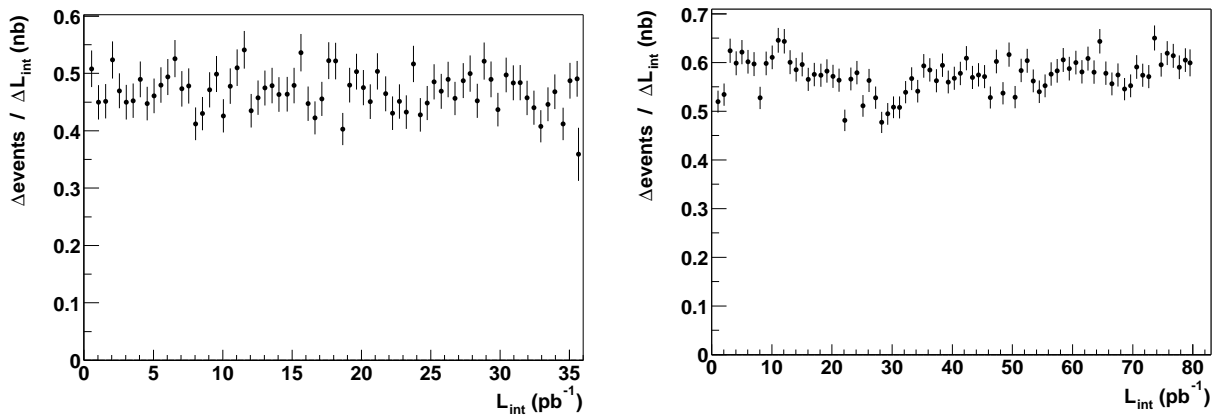


**Figure 4.1:** The number of accumulated events per luminosity interval as a function of the accumulated luminosity for the 1994–1997 (left) and 1998–2000 (right) data samples.

## 4.4 Object Definitions and Event Classification

The event analysis is based on uniquely defined objects. Objects are electrons, muons, photons, jets and neutrinos. These objects are defined by a set of object requirements. All selected events are grouped, depending on the number and types of objects, into exclusive event classes. No further phase space requirements are demanded on event classes to avoid any bias. Hereby, an unambiguous statistical interpretation and a well-defined separation of final state configurations are ensured.

The object definition consists of two parts: the object criteria and the quality criteria. With the object criteria the objects are identified, e.g. part of the object criteria are the identification and reconstruction algorithms, the required polar angle range and the  $P_T$  cut. In the next step, the quality criteria are applied to ensure that these objects were not misidentified. If one of the quality criteria is not passed, the full event is rejected because it cannot be unambiguously assigned to one event class. For example, an electron can fake a jet. If in a 3-jet event one high  $P_T$  jet is found which fails the jet quality criteria, it is likely that this jet is in fact an electron. This event can neither be clearly assigned to the 3-jet class nor to any other event class. Thus this event is rejected. In general, events with a compact, isolated object in the considered phase space which is not identified as a jet, an electron or a photon are rejected by the quality criteria. The quality criteria thus minimise wrong classification of events. The definitions of all considered objects are described in the next sections.

Finally, each event is assigned to one single event class. All selected events are grouped into event classes according to the number and types of objects which have been defined in the event. An event can only belong to one event class because the classification is exclusive. All possible event classes with two or more objects are considered.

### 4.4.1 Jet Identification

Jets are reconstructed using the theoretically and experimentally favoured inclusive  $k_\perp$  algorithm as proposed in ref. [80]. The application of this algorithm has become standard in jet analyses at HERA. It utilises a definition of jets in which not all particles are assigned to hard jets. Here, it is applied in the laboratory frame with the separation parameter set to 1 and using a  $P_T$  weighted recombination scheme where the jets are treated as massless.

The jet identification proceeds using well-calibrated combined objects (see sec. 4.6). Jets are defined by requirements on the transverse momentum (above 20 GeV) and on the polar angle,  $10^\circ < \theta < 140^\circ$ . The  $P_T$  cut ensures that the trigger efficiency for events with jets is at least 90% (see sec. 4.7), and it reduces contributions of higher order QCD radiation and non-perturbative effects like hadronisation or soft underlying events [81]. There are also various experimental reasons to restrict the polar angle range. First, the jets have to be well contained in the LAr calorimeter, which has a polar angle range of  $4^\circ < \theta < 154^\circ$ . Second, the jet energy calibration is not well described by the MC predictions for  $\theta < 10^\circ$ . A third reason is the high fake jet

contribution at high polar angle values (see below).

Due to inefficiencies of the electron finder the scattered electron may fake or be part of a jet, especially in detector regions where the amount of dead material is significant. This effect is important for multi-jet events, in particular at high transverse momenta or invariant masses of the jets. Several criteria, described below, have been studied and developed to reject these events. Fig. 4.2 illustrates the fake background and the impact of the designed cuts for the  $j$ - $j$  event class. In this figure and in the upcoming control distributions, the HERA I data sample is compared to the SM prediction for the  $j$ - $j$  event class, which is dominated by photoproduction events. The contribution of events where the generated electron lies within a cone of  $R = 1$  inside the reconstructed jet is labelled “Generator match”. At the top of fig. 4.2, the distribution of the invariant mass of the two jets  $M_{\text{all}}$  is shown before and after the application of jet quality criteria. It can clearly be seen that the fake contribution increases towards high masses. At  $M_{\text{all}} \gtrsim 200$  GeV, the SM contribution consists almost entirely of fake jet events. After the application of the jet quality criteria, the fake jet events contribute less than 15% to the SM prediction. At the bottom of fig. 4.2, the distribution of the polar angle of the second highest  $P_T$  jet corroborates a larger fake contribution at larger polar angles.

In the following, the developed cuts are described:

- The invariant mass  $M^{\text{Jet}}$  of a jet is defined as:

$$M^{\text{Jet}} = \sqrt{(\sum_i p_i^\mu)^2}.$$

The sum runs over the four-momentum  $p_i^\mu$  of each object  $i$  belonging to the jet. The invariant mass of the jet from the  $k_\perp$  algorithm is, however, zero by definition and differs from  $M^{\text{Jet}}$ . Following ref. [81],  $M^{\text{Jet}}$  is found to be a good discriminating variable against fake jets having mainly small  $M^{\text{Jet}}$  values. The discriminating power can be further increased by normalising the mass of a jet to its energy  $E^{\text{Jet}}$ . The resulting  $M^{\text{Jet}}/E^{\text{Jet}}$  distributions are shown for the leading and second highest  $P_T$  jet at top of fig. 4.3. Normalising the mass of the jet to its transverse momentum ( $M^{\text{Jet}}/P_T^{\text{Jet}}$ ) is an even more discriminating quantity. Therefore, depending on the fraction of the jet energy which is attributed to the electromagnetic section of the LAr calorimeter,  $EM_{\text{frac}}^{\text{Jet}}$ , (see fig. 4.3), different criteria are applied:

- $M^{\text{Jet}}/P_T^{\text{Jet}} > 0.1$
- $M^{\text{Jet}}/P_T^{\text{Jet}} > 0.15$  if  $EM_{\text{frac}}^{\text{Jet}} > 0.9$ .

The corresponding  $M^{\text{Jet}}/P_T^{\text{Jet}}$  distributions are shown in fig. 4.4, where the applied cuts are indicated by a dashed line.

- Jets faked by electrons are often very collimated and have a high electromagnetic fraction. The radial width varies as a function of the transverse momentum of a jet and can be

quantified with the radial moment [82]

$$\langle R \rangle = \frac{\sum_i P_{T,i} R_i^{\text{Jet}}}{\sum_i P_{T,i}}.$$

The sum runs over the transverse momentum  $P_{T,i}$  of each object  $i$  belonging to the jet. Their distance in the  $\eta - \phi$  plane to the jet axis is denoted by  $R_i^{\text{Jet}}$ .

Based upon these facts, the following quality criteria have been found to be very effective in rejecting electrons misidentified as jets:

- $\langle R \rangle > 0.02$
- $\langle R \rangle > 0.04$  if  $EM_{\text{frac}}^{\text{Jet}} > 0.9$ .

The corresponding  $\langle R \rangle$  distributions are shown in fig. 4.5, where the applied cuts are indicated by a dashed line.

According to MC studies, these cuts reject less than 1% of events where all selected jets are genuine and about 76% of events where an electron is misidentified as a jet in the  $j$ - $j$  event class. The rejection power for different event classes is shown in tab. 4.4. In addition, efficiencies and purities<sup>4</sup> before and after the cuts are depicted in fig. 4.6 for the  $j$ - $j$  event class. The probability to have a fake jet is much larger in pure jet event classes ( $j$ - $j$ ,  $j$ - $j$ - $j$  and  $j$ - $j$ - $j$ - $j$  event classes) than in event classes where the scattered electron is identified with a high efficiency (e.g.  $e$ - $j$  event class). In the latter event classes, the purity is therefore almost not affected by the cuts. The minimal loss in efficiency in all jet event classes is, however, acceptable considering the gain in purity, which is in particular very high in the pure jet event classes. Other jet selection criteria have also been tested and found to be less powerful. Their studies are summarised in app. C for completeness. The final jet selection criteria are summarised in tab. 4.5.

---

<sup>4</sup>Efficiencies and purities are defined in sec. 4.9.

Event Class	Fake Rejection (%)	Non-Fake Rejection (%)
$j$ - $j$	76.1	0.9
$e$ - $j$	31.1	0.9
$\mu$ - $j$	93.9	4.0
$j$ - $\nu$	89.1	1.6
$j$ - $\gamma$	61.8	0.8
$j$ - $j$ - $j$	57.3	1.8
$e$ - $j$ - $j$	15.2	1.2
$j$ - $j$ - $\nu$	85.7	2.6

**Table 4.4:** Rejection power of the cuts against fake jets. Listed is the percentage of rejected events with a least one fake jet (Fake Rejection) and with only genuine jets (Non-Fake Rejection).

object criteria
$P_T > 20 \text{ GeV}$
$10^\circ < \theta < 140^\circ$
reconstructed with inclusive $k_\perp$ algorithm
quality criteria
$M^{\text{Jet}}/P_T^{\text{Jet}} > 0.1$
$M^{\text{Jet}}/P_T^{\text{Jet}} > 0.15$ if $EM_{\text{frac}}^{\text{Jet}} > 0.9$
$\langle R \rangle > 0.02$
$\langle R \rangle > 0.04$ if $EM_{\text{frac}}^{\text{Jet}} > 0.9$

**Table 4.5:** The jet selection criteria.

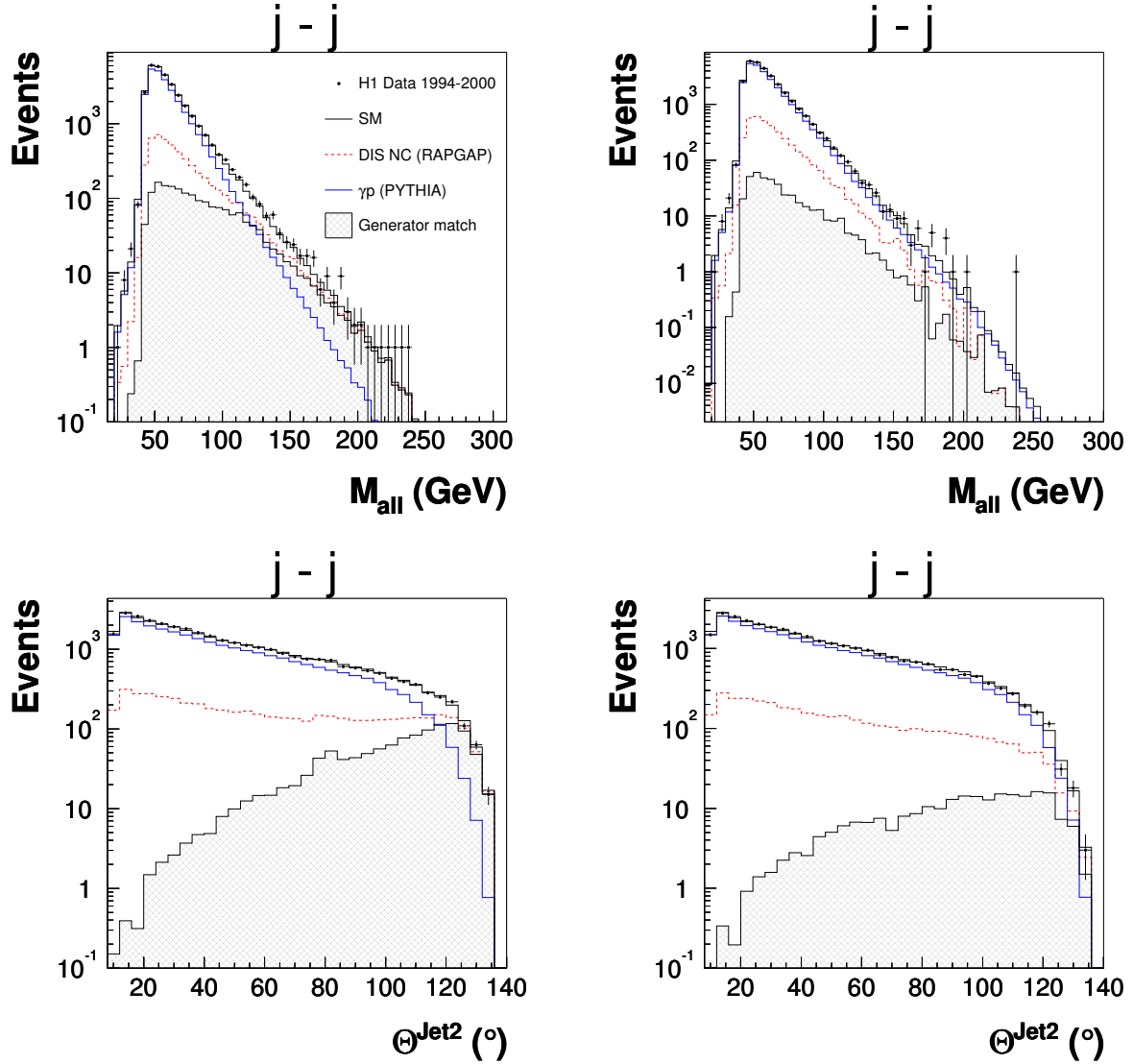


**Figure 4.2:** The left side shows the distribution of the invariant mass of the two jets (top) and of the polar angle of the second highest  $P_T$  jet (bottom) before the application of the jet quality criteria. The corresponding distributions after the application are shown on the right side. In this figure and in the upcoming control distributions, the HERA I data sample is compared to the SM prediction for the  $j$ - $j$  event class; the contributions from DIS NC and photoproduction processes are also shown. The shaded contribution labelled “Generator match” represents the events where the generated electron lies within a cone of  $R = 1$  inside the reconstructed jet. In particular at high invariant masses and at high jet polar angles, the fake jet contribution is considerably reduced.



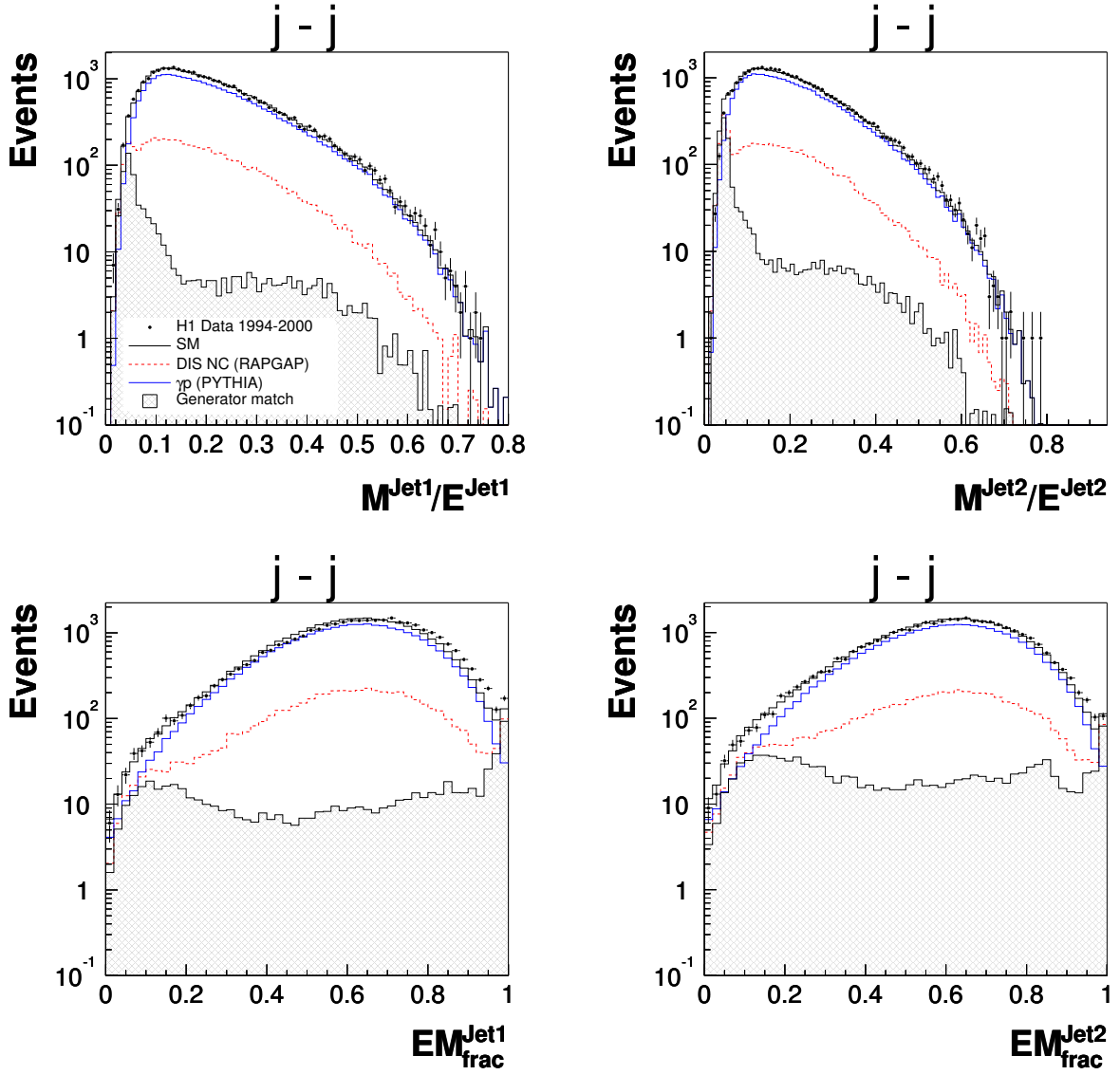


**Figure 4.3:** The mass normalised to the energy for the two selected jets (top). The electromagnetic fraction of the jets is shown at the bottom.

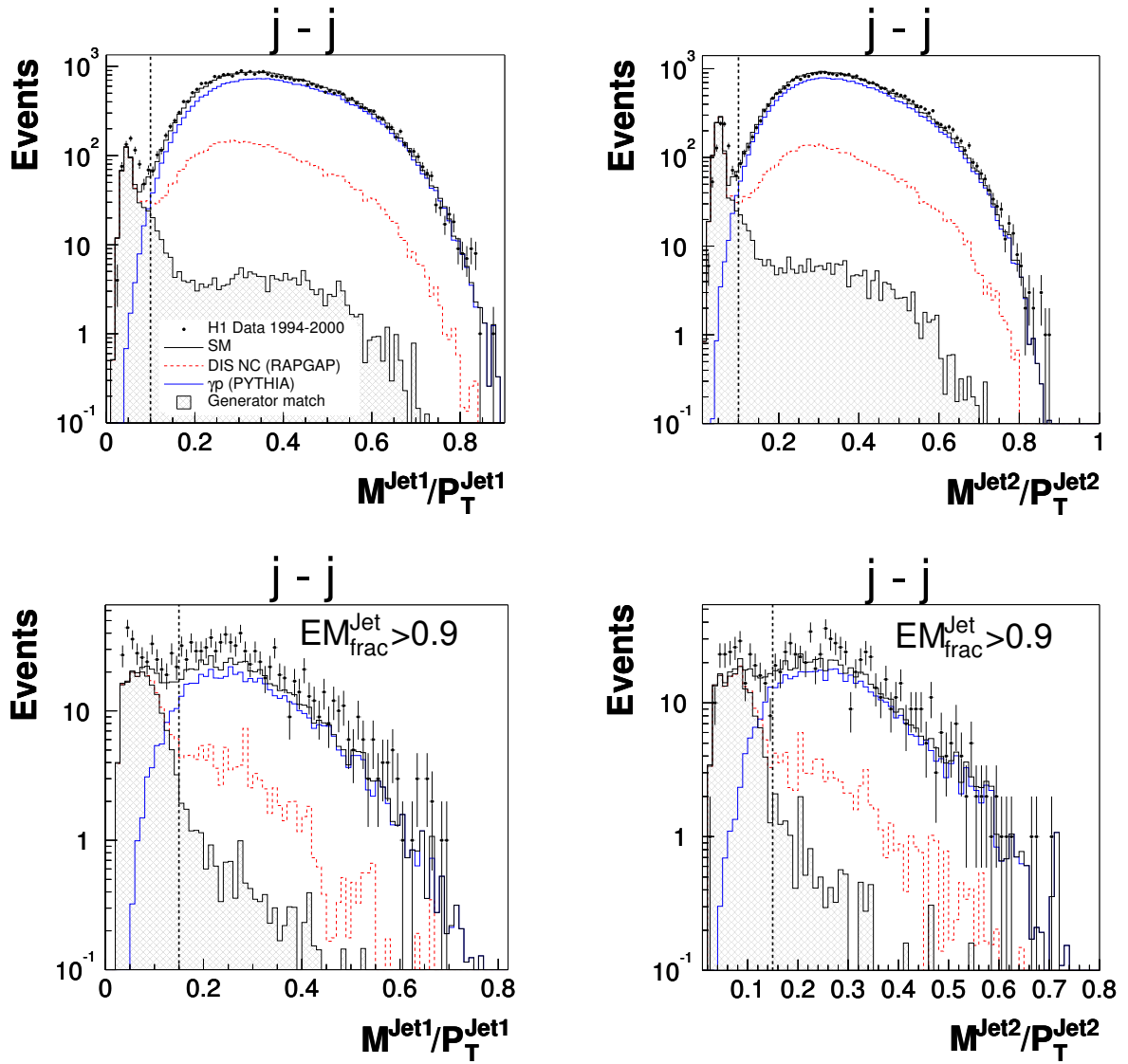


**Figure 4.4:** The mass  $M^{\text{Jet}}$  of the jet normalised to its transverse momentum  $P_T^{\text{Jet}}$ . The quantity is plotted on the left side for the leading jet and on the right for the jet with the second highest  $P_T$  without (top) and with (bottom) the requirement  $EM_{\text{frac}}^{\text{Jet}} > 0.9$ .

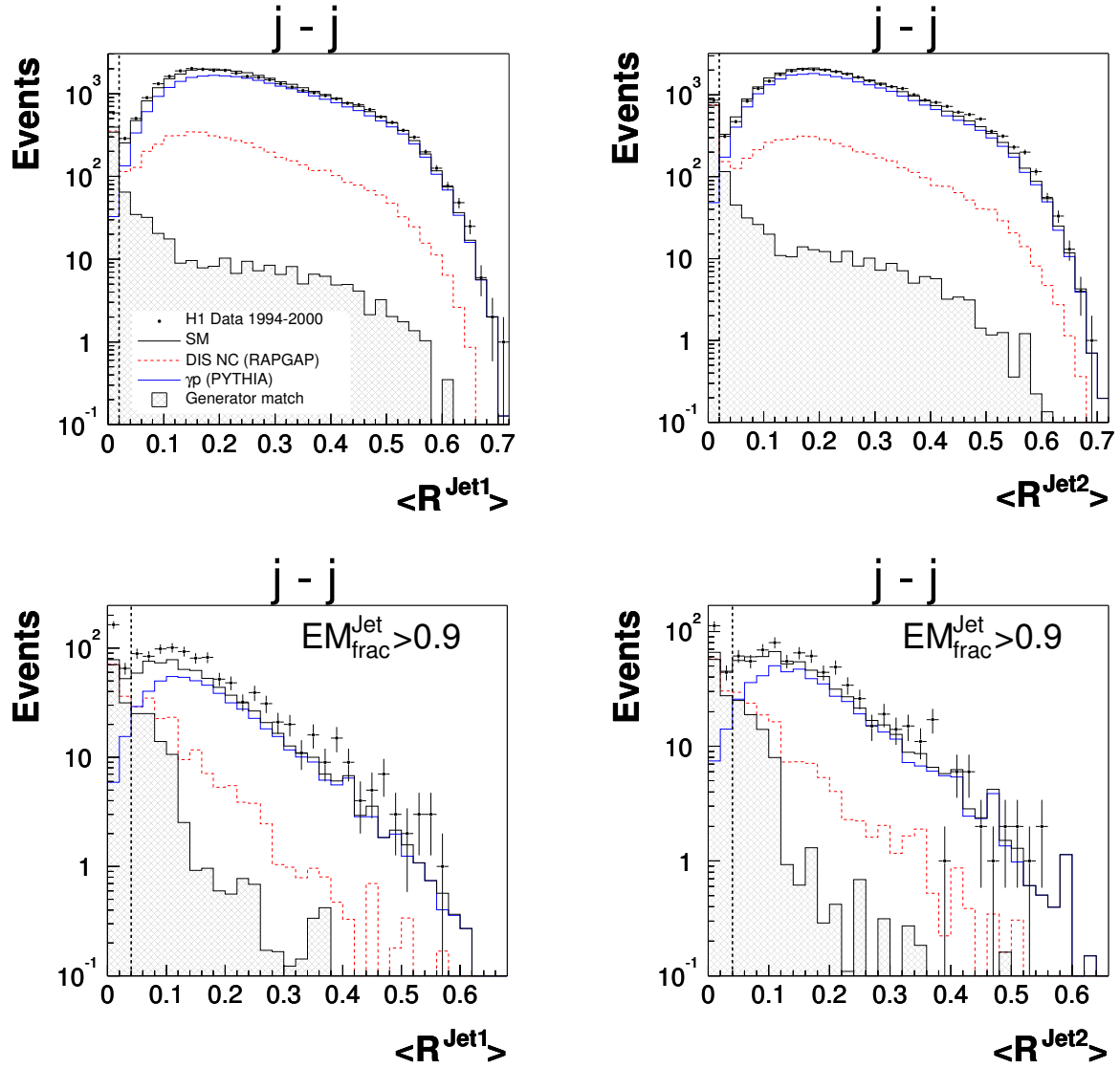


**Figure 4.5:** The radial moment of the leading jet (left side) and of the jet with the second highest  $P_T$  (right side) without (top) and with (bottom) the requirement  $EM_{\text{frac}}^{\text{Jet}} > 0.9$ .

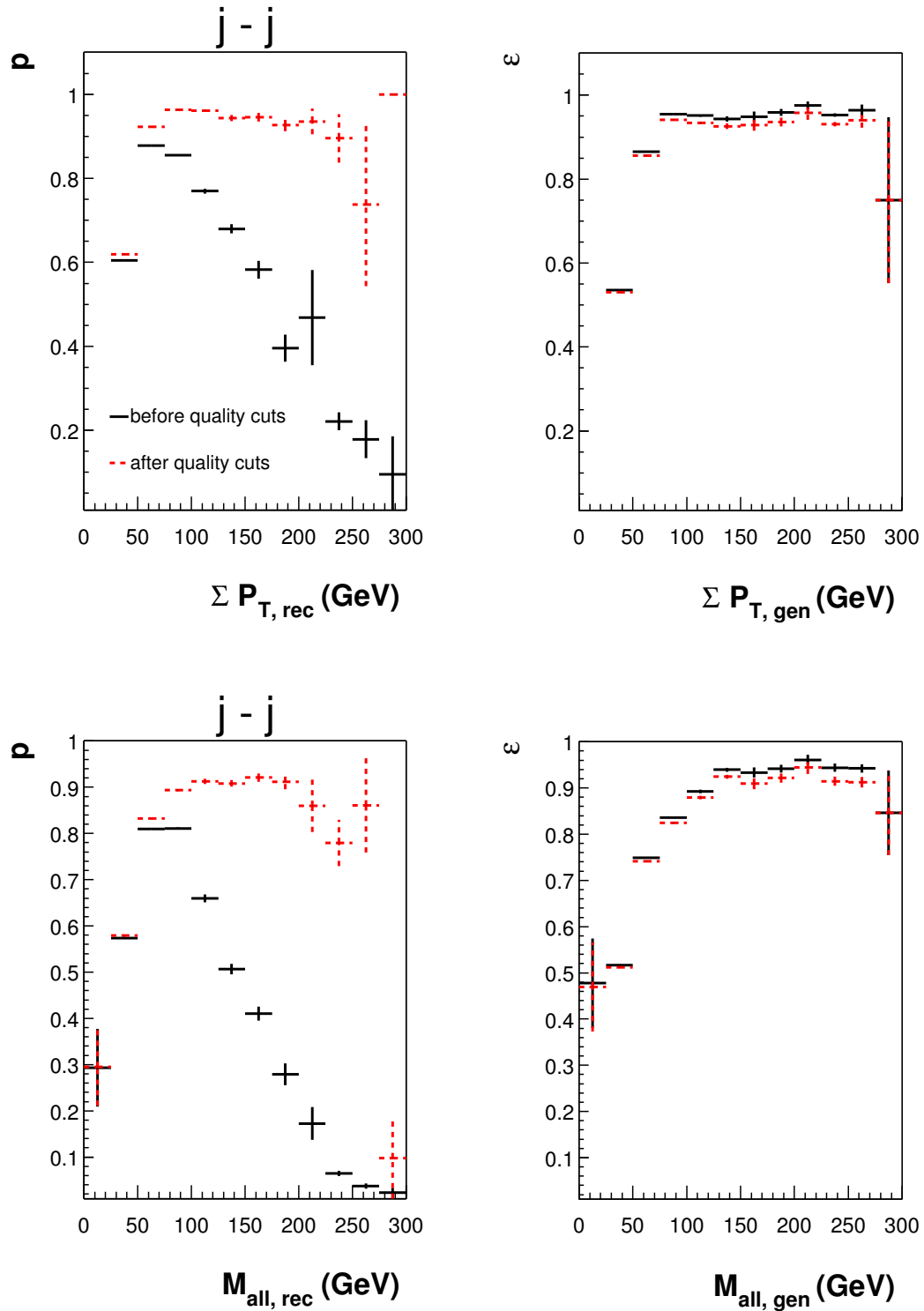


**Figure 4.6:** Efficiencies and purities before and after the application of the jet quality criteria as a function of  $\Sigma P_T$  and the invariant mass  $M_{\text{all}}$  of the two selected jets in the  $j-j$  event class. The subscripts *rec* and *gen* denote the reconstructed and generated quantities, respectively.

### 4.4.2 Electron Identification

This section briefly describes the electron identification. The corresponding, complete studies can be found in refs. [3, 83] and references therein. To identify electron candidates, the search algorithm QECFWD [84] is used. The algorithm is part of the electron finder QESCAT [85], which is implemented in the physics analysis library H1PHAN [86].

The electron identification is based on the measurement of a compact and isolated electromagnetic shower in the LAr calorimeter. The electron candidate must have a transverse momentum above 20 GeV and be in the polar angle range  $10^\circ < \theta < 140^\circ$ . The hadronic energy within  $R = 0.75$  around the electron is required to be below 2.5% of the electron energy ( $E_{R=0.75}/E^e < 2.5\%$ ). This calorimetric electron identification is complemented by tracking conditions. It is required that a high quality track geometrically matches the electromagnetic cluster within a distance of closest approach ( $DCA_{cl}^{tk}$ ) to the cluster centre-of-gravity of 12 cm. Tracks from both BOS [87] banks called DTRA and DTNV are considered. The DTRA (DTNV) bank contains vertex (non-vertex) fitted tracks. No other good track<sup>5</sup> is allowed within  $R = 0.5$  around the electron direction ( $R_{cl}^{gk} > 0.5$ ). Electrons scattered into partially inefficient regions, such as cracks between calorimeter modules ( $\phi$ -cracks) or wheels ( $z$ -cracks) are not considered ( $|\phi^e - \phi_{crack}| > 2^\circ$ ,  $|z^e - z_{crack}| > 2$  cm).

In the region  $20^\circ < \theta < 140^\circ$ , the starting radius of the measured track, defined as the distance in the  $xy$ -plane between the first measured point in the central drift chambers and the beam axis,  $R_{start}$ , is required to be below 30 cm in order to reject photons which convert late in the central tracker material. In addition, the transverse momentum measured from the associated track  $P_T^{e_{tk}}$  is required to match the calorimetric measurement  $P_T^e$  with  $1/P_T^{e_{tk}} - 1/P_T^e < 0.02 \text{ GeV}^{-1}$ . Due to higher material density in the forward region, the electrons are more likely to shower. In the region not fully covered by the central drift chambers ( $10^\circ < \theta < 37^\circ$ ), a tighter calorimetric isolation cone of  $R = 1$  is required to reduce the contribution of fake electrons from hadrons ( $E_{R=1}/E^e < 2.5\%$ ). The identification is further complemented by the requirement of hits in the central inner proportional chamber (CIP) within a distance  $\Delta z_{CIP} < 10$  cm to the extrapolated  $z$ -impact of the electromagnetic cluster to the CIP surface.

Finally, certain  $\phi$ -regions are excluded for both the electron and photon identifications. In the data taking period 1997  $e^+$  and 1999  $e^+$ , the  $\phi$ -regions of the CJC corresponding to the interval  $230^\circ \lesssim \phi \lesssim 250^\circ$  and  $190^\circ \lesssim \phi \lesssim 280^\circ$ , respectively, were inefficient due to hardware problems. As tracks cannot be reconstructed for these periods and  $\phi$ -regions, an electron candidate cannot be distinguished from a photon candidate. The affected 1997  $e^+$  and 1999  $e^+$  data samples correspond to an integrated luminosity of  $\approx 21 \text{ pb}^{-1}$  and  $\approx 8 \text{ pb}^{-1}$ , respectively, and are thus not considered in the electron and photon candidate selections.

The resulting electron finding efficiency is approximately 85% in the central region and 70% in the forward region. The electron selection criteria are summarised in tab. 4.6.

<sup>5</sup>A good track is a DTRA track fulfilling the quality criteria described in app. A.

object criteria		
$P_T > 20 \text{ GeV}$		
$10^\circ < \theta < 140^\circ$		
identified with the finder QESCAT		
quality criteria		
not in $\phi$ -region and time period affected by CJC failure		
electron cluster criteria		
$10^\circ < \theta < 37^\circ$		$37^\circ < \theta < 140^\circ$
$E_{R=1}/E^e < 2.5\%$		$E_{R=0.75}/E^e < 2.5\%$
$ \phi^e - \phi_{\text{crack}}  > 2^\circ$ , with $\phi_{\text{crack}} \in \{0^\circ, 45^\circ, 90^\circ, 135^\circ, 180^\circ, 225^\circ, 270^\circ, 315^\circ\}$		
$ z^e - z_{\text{crack}}  > 2 \text{ cm}$ , with $z_{\text{crack}} \in \{-64.63 \text{ cm}, 23.17 \text{ cm}\}$		
electron track criteria		
$10^\circ < \theta < 20^\circ$	$20^\circ < \theta < 37^\circ$	$37^\circ < \theta < 140^\circ$
$DCA_{cl}^{tk} < 12 \text{ cm}$		
$R_{cl}^{gtk} > 0.5$ (DTRA)		
$\Delta z_{\text{CIP}} < 10 \text{ cm}$	$R_{\text{start}} < 30 \text{ cm}$	good quality (DTRA)
	$1/P_T^{etk} - 1/P_T^e < 0.02 \text{ GeV}^{-1}$	$R_{\text{start}} < 30 \text{ cm}$
	$\Delta z_{\text{CIP}} < 10 \text{ cm}$	$1/P_T^{etk} - 1/P_T^e < 0.02 \text{ GeV}^{-1}$

**Table 4.6:** The electron selection criteria. The track conditions apply to both DTRA and DTNV tracks if not otherwise stated and are only rejective if the photon anti-track criteria are not fulfilled.

### 4.4.3 Photon Identification

This section briefly describes the photon identification. The corresponding, complete studies can be found in refs. [3, 83] and references therein.

Photon candidates must have a transverse momentum above 20 GeV and be in the angular range  $10^\circ < \theta < 140^\circ$ . The photon identification relies on the same measurement of an electromagnetic shower and the same calorimetric isolation criteria against hadrons as the electron identification. In addition no jet with a  $P_T > 5$  GeV in the vicinity of the photon candidate, *i.e.* within a distance of  $R = 1$ , should be present ( $R_{cl}^{\text{Jet}} > 1$ ). Vetoes on any charged track pointing to the electromagnetic cluster are applied. No track (neither DTRA nor DTNV) with a  $DCA_{cl}^{tk}$  below 24 cm or within  $R = 0.5$  should be present ( $R_{cl}^{tk} > 0.5$ ). To account for possible inefficiencies of the inner tracking system, an additional veto on any hits in the CIP is applied, *i.e.*  $\Delta z_{\text{CIP}} > 10$  cm.

Furthermore, the misidentification efficiency for electrons is important for the photon identification. It has been studied in refs. [3, 83]. As already explained in sec. 4.4.2, certain  $\phi$ -regions are not considered in the data taking period 1997  $e^+$  and 1999  $e^+$ . Finally, all photon selection criteria are summarised in tab. 4.7.

object criteria	
$P_T > 20$ GeV	
$10^\circ < \theta < 140^\circ$	
identified with the finder QESCAT	
quality criteria	
not in $\phi$ -region and time period affected by CJC failure	
photon cluster criteria	
$10^\circ < \theta < 37^\circ$	$37^\circ < \theta < 140^\circ$
$E_{R=1}/E^\gamma < 2.5\%$	$E_{R=0.75}/E^\gamma < 2.5\%$
$ \phi^e - \phi_{\text{crack}}  > 2^\circ$ , with $\phi_{\text{crack}} \in \{0^\circ, 45^\circ, 90^\circ, 135^\circ, 180^\circ, 225^\circ, 270^\circ, 315^\circ\}$	
$ z^e - z_{\text{crack}}  > 2$ cm, with $z_{\text{crack}} \in \{-64.63 \text{ cm}, 23.17 \text{ cm}\}$	
$R_{cl}^{\text{Jet}} > 1$	
photon anti-track criteria	
$10^\circ < \theta < 140^\circ$	
$DCA_{cl}^{tk} > 24$ cm	
$R_{cl}^{tk} > 0.5$	
$\Delta z_{\text{CIP}} > 10$ cm	

**Table 4.7:** The photon selection criteria. The track conditions always apply to both DTRA and DTNV tracks and are only rejective if the electron track criteria are not fulfilled.

#### 4.4.4 Muon Identification

In this analysis, muon candidates are selected in the phase space given by the transverse momentum requirement  $P_T > 20 \text{ GeV}$  and the polar angle range  $10^\circ < \theta < 140^\circ$ . Furthermore, they must have a track in the inner tracking system which matches at least one of the following signatures:

- a track in the central muon detector
- an energy deposit in the tail catcher calorimeter
- a track in the forward muon detector.

In addition, in the polar angle range  $\theta < 12.5^\circ$ , muon candidates are also selected if they solely have a track in the forward muon detector.

The track selection in the inner, *i.e.* forward and central, tracking system is based on standard quality requirements which are summarised in app. A. In order to reduce hadronic background, different isolation criteria are applied. First, muon candidates are required to be isolated against jets which have a  $P_T$  above  $5 \text{ GeV}$  ( $R^{\text{Jet}} > 1$ ) and against good tracks ( $R^{\text{gtrk}} > 0.5$ ). Second, the muon candidate must fulfil a calorimetric isolation: the energy  $E_{R=0.5}^{\text{LAr}}$  deposited in the LAr calorimeter in a cylinder of  $R = 0.5$  centred on the muon direction associated with its track, must be less than  $8 \text{ GeV}$ . Other additional requirements for the muon selection depend on the location and type of the signals and are called “basic muon selection criteria” hereinafter. The final selection criteria are summarised in tab. 4.8. The resulting identification efficiency is established to be greater than  $90\%$  [4]. In the following, the basic muon selection criteria are described separately for each of the signatures mentioned at the beginning of this section.

object criteria
basic muon selection criteria
$P_T > 20 \text{ GeV}$
$10^\circ < \theta < 140^\circ$
$R^{\text{Jet}} > 1$
$R^{\text{gtrk}} > 0.5$
$E_{R=0.5}^{\text{LAr}} < 8 \text{ GeV}$
quality criteria
cosmic and beam halo background rejection cuts

**Table 4.8:** *The muon selection criteria.*



### Muons in the Central Muon Detector

Muons reaching the instrumented iron produce signals in the limited streamer tubes. These signals are grouped by a pattern recognition program into associations, which are used as input to a track fit delivering the final kinematic values of the track in the muon system. The tracks reconstructed in the instrumented iron which are successfully linked to a track in the inner system build a hypothesis for a muon candidate. In order to increase the purity of the muon candidates, a maximal distance of the track extrapolation from the vertex and hits in a minimal number of layers are required. Tab. 4.9 summarises the conditions for the muon identification. The details are described in ref. [79] and references therein.

Muons in the Central Muon Detector			
Condition	Barrel	Forward Endcap < 25°      > 25°	Backward Endcap
<b>I</b>	$\rho < 100 \text{ cm}$	$\rho_x < 100 \text{ cm}$	$\rho_x < 100 \text{ cm}$
<b>II</b>	$z_0 < 100 \text{ cm}$	$\rho_y < 100 \text{ cm}$	$\rho_y < 100 \text{ cm}$
<b>III</b>	$N_{\text{first}}$	$\leq 5$	$\leq 5$
	$N_{\text{layer, iron}}$	$\geq 3$	$\geq 3$
<b>IV</b>	$N_{\text{total}}$	$\geq 5$	$\geq 5$

- $\rho, \rho_{x,y}$ : minimal radial distance of the track in the central muon detector extrapolated to the vertex and the corresponding  $x$ - and  $y$ -components, respectively
- $z_0$ :  $z$ -coordinate of the first measured point of the track in the central muon detector
- $N_{\text{first}}$ : layer number of first layer which has been hit
- $N_{\text{layer, iron}}$ : number of hit streamer tube layers excluding the muon boxes
- $N_{\text{total}}$ : total number of hits, *i.e.* the sum of hits in all streamer tube layers (including the muon boxes) and of hits in the strip and pad electrodes

**Table 4.9:** Conditions for muon identification. Conditions I and II together with condition III or IV have to be fulfilled.

### Muons in the Tail Catcher Calorimeter

The tail catcher increases the muon finding efficiency in regions of the instrumented iron where the track reconstruction is limited due to geometrical acceptance, like *e.g.* in the transition regions between the barrel and the endcaps. An energy deposit in the instrumented iron is required to match an inner track within a distance of  $R = 0.5$ . Hadronic showers leaking in the tail catcher are further suppressed by requiring that the minimum depth of  $E_{R=0.5}^{\text{LAR}}$  is  $\geq 40 \text{ cm}$  and that

the number of LAr clusters contributing to  $E_{R=0.5}^{\text{LAr}}$  is at least one. The selection criteria are summarised in tab. 4.10 and described in detail in ref. [88].

Muons in the Tail Catcher Calorimeter	
$\eta - \phi$ distance of inner track to tail catcher cluster	$\leq 0.5$
minimum depth of $E_{R=0.5}^{\text{LAr}}$	$\geq 40$ cm
number of LAr clusters contributing to $E_{R=0.5}^{\text{LAr}}$	$\geq 1$

**Table 4.10:** Conditions for muon candidates identified by their tail catcher signal. The extra conditions required for the energy deposit in the LAr calorimeter suppresses hadronic background [88].

### Muons in the Forward Muon Detector

In the polar angle range  $3^\circ \leq \theta \leq 17^\circ$ , high energetic muons can be measured by the forward muon detector. The curvature of the muon track in the toroidal magnetic field can be used to determine the transverse momentum of the muon candidate. The measurement of the forward muon detector is used in this analysis if the polar angle of the muon candidate is below  $12.5^\circ$  and if there was no track measurement for the muon candidate from the inner tracking system. Forward muon candidates must fulfil a certain track quality, and the  $z$ -coordinate of the first measured point of the track in the forward muon detector ( $z_0$ ) must be in the range  $-400 \text{ cm} < z_0 < 300 \text{ cm}$ . The selection criteria applied to forward muon candidates are summarised in tab. 4.11.

Muons in the Forward Muon Detector	
track quality	1 or 2
$z_0$	$-400 \text{ cm} < z_0 < 300 \text{ cm}$

**Table 4.11:** Conditions for muon identification in the forward muon detector.

### Cosmic and Beam Halo Background Rejection

The basic ideas for the rejection of muon candidates originating from cosmic radiation or the beam halo are briefly outlined in the following. A detailed description can be found in ref. [79]. Cosmic background is rejected by applying several cuts summarised in tab. 4.12. A cut on the track opening angles  $\alpha_{\text{DTNV}, \text{DTRA}}$  and polar angle sum of muon pairs ( $\theta_{\text{DMUO}}^{\mu 1} + \theta_{\text{DMUO}}^{\mu 2}$ ) is intended to discard events with muons coming from cosmic rays. These angular conditions use information from the inner tracking system (DTRA and DTNV tracks) and the central muon detector (DMUO tracks). The event timing condition for muon events is more restricted and the cut on the track timing difference between the muon track in the upper and lower part of the detector,  $T_{\text{upper}}^\mu - T_{\text{lower}}^\mu$ , rejects the cosmic muons residing at high values of this quantity. Beam halo events are rejected by requiring that the muons originate from the vertex.

Opening angle	$\alpha_{\text{DTNV, DTRA}} < 165^\circ$
Polar angle sum (if $\alpha_{\text{DTNV, DTRA}} > 150^\circ$ )	$ \theta_{\text{DMUO}}^{\mu 1} + \theta_{\text{DMUO}}^{\mu 2} - 180^\circ  > 10^\circ$
Event timing	$ \Delta T_0  < 3.8 \text{ ns}$
Track timing	$T_{\text{upper}}^\mu - T_{\text{lower}}^\mu < 3.8 \text{ ns}$

**Table 4.12:** Cosmic background rejection. The collinear cosmic events are suppressed by the cuts on the opening angles  $\alpha_{\text{DTNV, DTRA}}$  and the sum  $\theta_{\text{DMUO}}^{\mu 1} + \theta_{\text{DMUO}}^{\mu 2}$ . To improve the cosmic rejection additional timing cuts are applied.

### 4.4.5 Neutrino Identification

For the reconstruction of the neutrino kinematics, it is assumed that all missing momentum is carried away by exactly one neutrino. The energy  $E^\nu$  and the polar angle  $\theta^\nu$  of the neutrino are calculated as in ref. [25], i.e.

$$E^\nu = \frac{\not{p}_T^2 + (E - P_Z)_\nu^2}{2(E - P_Z)_\nu} \quad \text{and} \quad \cos \theta^\nu = \frac{\not{p}_T^2 - (E - P_Z)_\nu^2}{\not{p}_T^2 + (E - P_Z)_\nu^2},$$

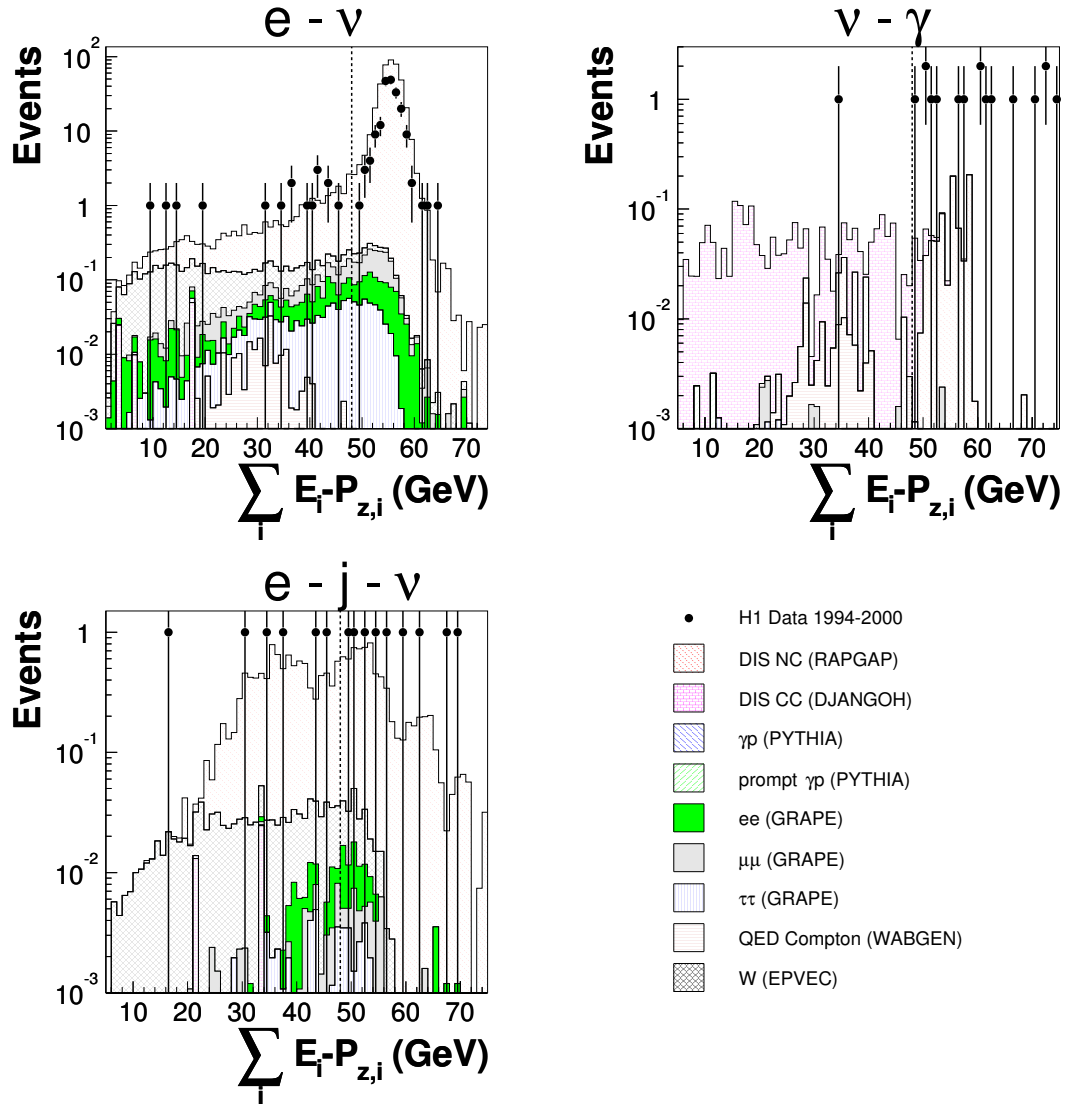
where  $(E - P_Z)_\nu = 2E_{\text{beam}}^e - (\sum_i E_i - P_{z,i})$ ,  $\not{p}_T$  is the missing transverse momentum, and  $E_{\text{beam}}^e$  is the energy of the beam electron.

A neutrino candidate is defined in events with a missing transverse momentum above 20 GeV. The missing momentum is derived from all identified particles and energy deposits in the event. A neutrino candidate is only assigned to the event if  $\sum_i E_i - P_{z,i} < 48 \text{ GeV}$ . This requirement discards neutrino candidates where the missing momentum is mostly caused by energy leakage in the forward direction. Figs. 4.7 and 4.8 show the distribution of  $\sum_i E_i - P_{z,i}$  for various event classes and corroborate that mainly events with a non-genuine neutrino have  $\sum_i E_i - P_{z,i} > 48 \text{ GeV}$ . The latter events are predominantly NC DIS events where the electron is identified and hadronic energy is partly lost in the beam pipe in forward direction. The neutrino phase space is only defined by the  $P_T$  and  $\sum_i E_i - P_{z,i}$  requirements.

Missing transverse momentum may also arise from mismeasurement of an identified object. This effect is reduced by isolating the neutrino in the  $\eta - \phi$  plane against all identified objects with a transverse momentum above 20 GeV ( $R^\nu > 1$ ). However, an additional criterion is applied to reduce NC and lepton pair background events where one particle's energy is mismeasured. These events typically have values of  $\Delta\phi(l - X_{\text{tot}})$  of  $180^\circ$ .  $\Delta\phi(l - X_{\text{tot}})$  is the azimuthal angle difference between the lepton and the direction of the system  $X_{\text{tot}}$  build of all energies measured in the calorimeters. It is only calculated if the sum of these energies is above 5 GeV in order to guarantee a good calorimetric measurement. If one electron or muon is found in the event which fulfils the object criteria, a neutrino candidate is only assigned to the event if  $\Delta\phi(l - X_{\text{tot}}) < 170^\circ$ . Fig. 4.9 shows the distribution of  $\Delta\phi(l - X_{\text{tot}})$  for the affected event classes, after the the requirement  $\sum_i E_i - P_{z,i} < 48 \text{ GeV}$ . For the  $e - \nu$  event class, the bin at  $\Delta\phi(l - X_{\text{tot}}) = 199^\circ$  contains all events where the sum of the calorimetric energies is below 5 GeV. Finally, fig. 4.10 displays the neutrino isolation in the  $\eta - \phi$  plane after the above requirements. All selection criteria for the neutrino are summarised in tab. 4.13.

object criteria
$\cancel{p}_T > 20 \text{ GeV}$
$\sum_i E_i - P_{z,i} < 48 \text{ GeV}$
$R^\nu > 1$
$\Delta\phi(l - X_{\text{tot}}) < 170^\circ$ if $\#e = 1$ or $\#\mu = 1$

Table 4.13: The neutrino selection criteria.

Figure 4.7: Distribution of  $\sum_i E_i - P_{z,i}$  for various event classes.

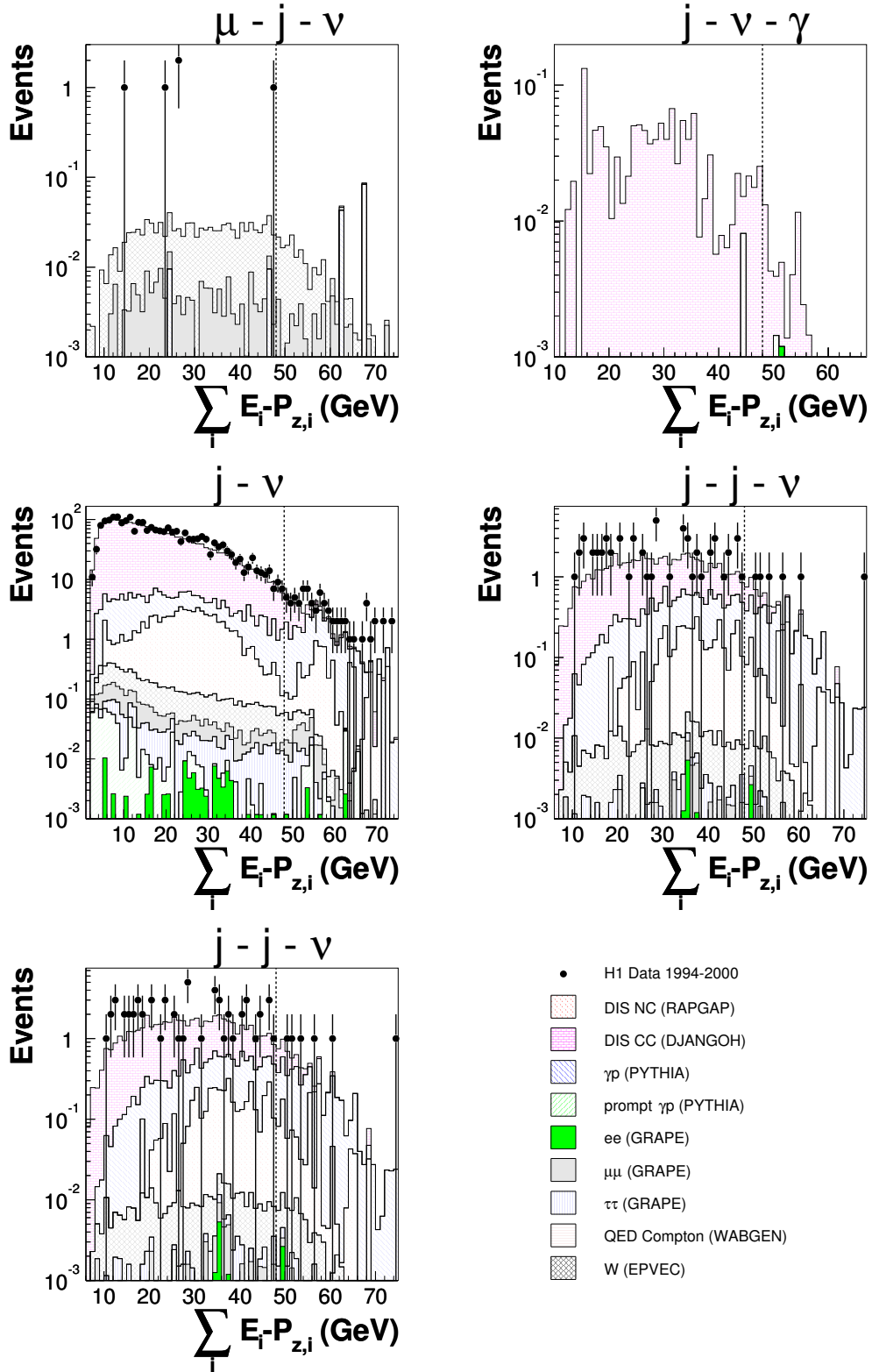
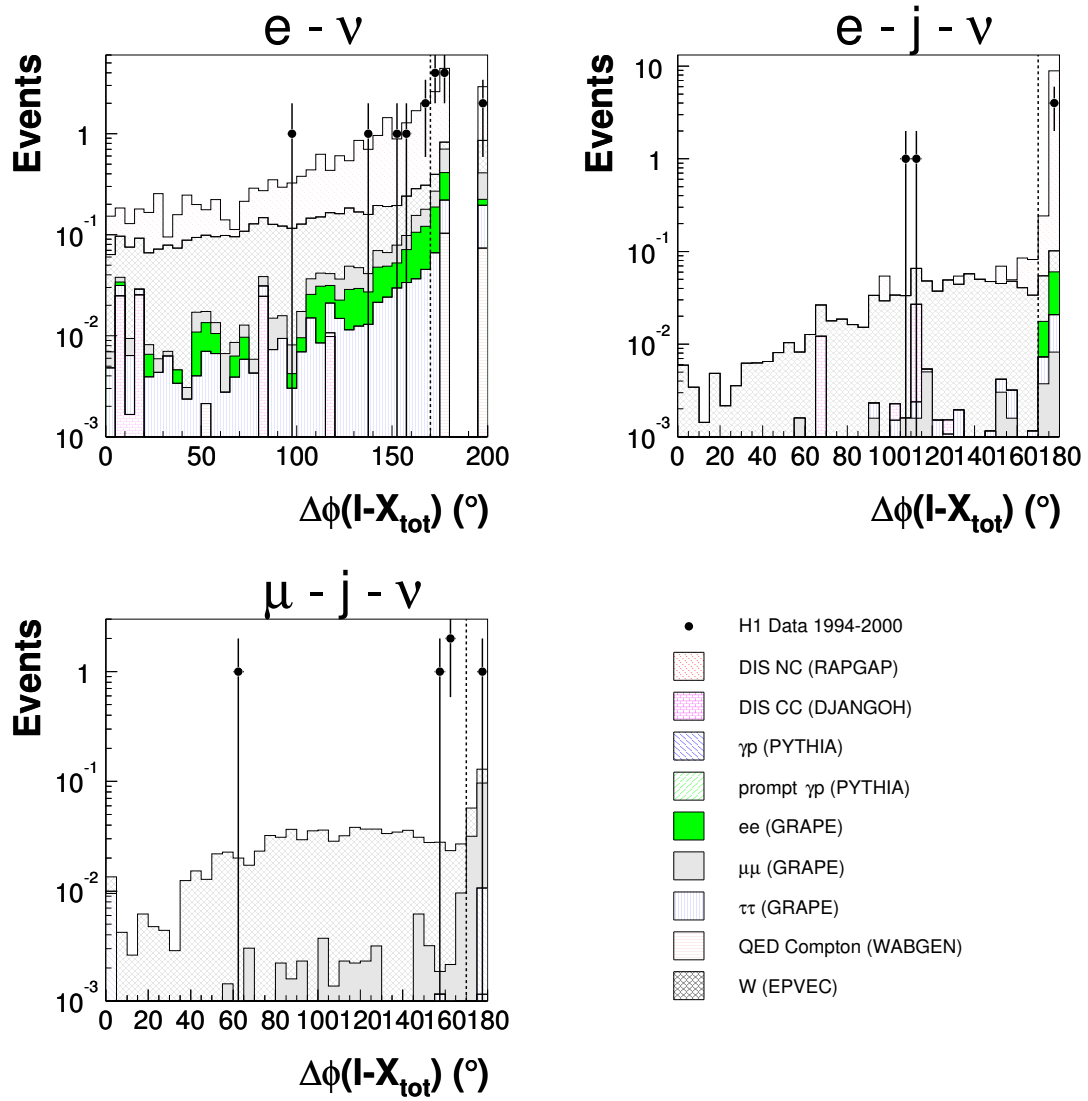
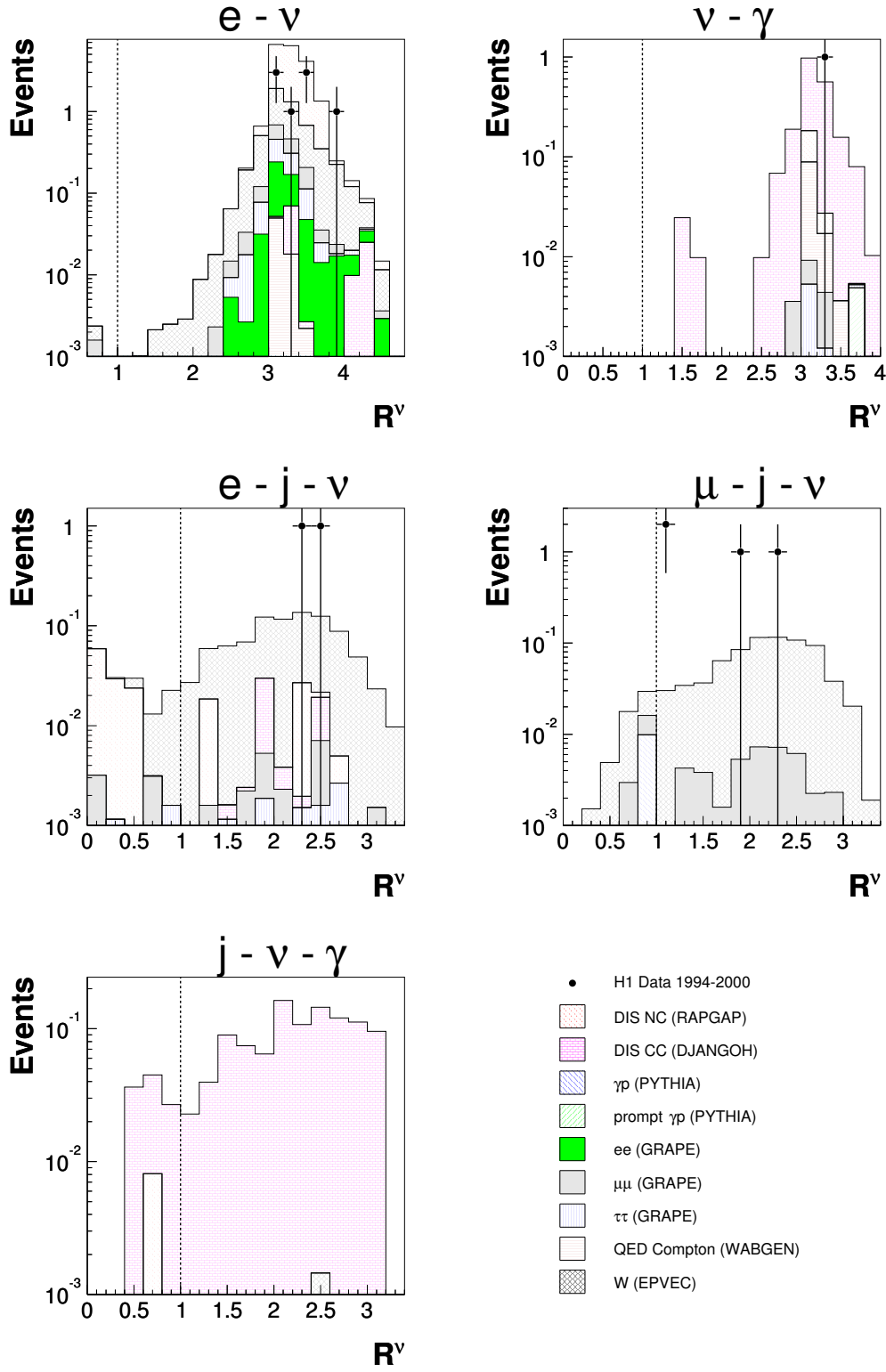


Figure 4.8: Distribution of  $\sum_i E_i - P_{z,i}$  for various event classes.



**Figure 4.9:** Distribution of  $\Delta\phi(l - X_{\text{tot}})$  for various event classes. For the  $e - \nu$  event class, the bin at  $\Delta\phi(l - X_{\text{tot}}) = 199^\circ$  contains all events where  $\Delta\phi(l - X_{\text{tot}})$  is not calculated because the sum of the calorimetric energies is below 5 GeV (see text).

Figure 4.10: Distribution of  $R^\nu$  for various event classes.

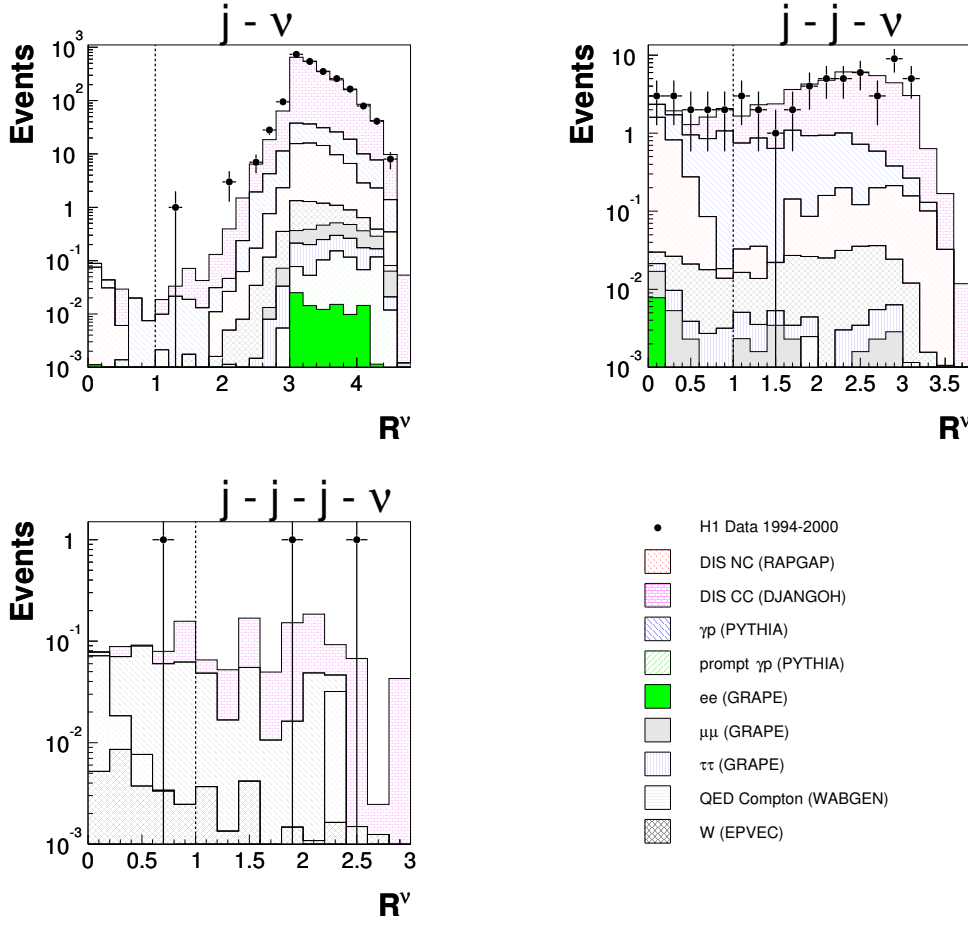


Figure 4.11: Distribution of  $R^\nu$  for various event classes.

## 4.5 Electron Calibration

In this analysis, electrons have been calibrated with a  $z$ , octant and year dependent high  $Q^2$  calibration as described in ref. [89]. The calibration has been revised for this analysis with a NC DIS sample in ref. [90]. The electromagnetic energy scale uncertainty is 1% if the  $z$ -position of the electromagnetic particle's impact on the calorimeter is in the backward part ( $z < -145$  cm), 0.7% in the CB1 and CB2 wheels ( $-145 < z < 20$  cm), 1.5% for  $20 < z < 100$  cm and 3% in the forward part ( $z > 100$  cm).

## 4.6 Hadronic Final State Reconstruction and Calibration

The hadronic final state is measured using the energy deposits in the LAr calorimeter, in the SpaCal, in the instrumented iron, as well as the track measurement in the inner tracking system. The reconstruction is performed by the algorithm FSCOMB [91, 92], which exploits the fact that the precision of the momentum measurement with the calorimeters increases with increasing



momentum, whereas the measurement of low momentum charged particles is much more precise with the inner tracking system. Therefore tracks which have a transverse momentum below 2 GeV and have been constrained to the primary vertex are extrapolated to the calorimeter front face. All energy deposits in the electromagnetic (hadronic) section of the calorimeter within a cylinder of radius 25 cm (50 cm) concentric to the extrapolated track are assigned to the track. If the energy in the cylinder is greater than the track energy, the calorimetric energy measurement is used and the track is discarded. Otherwise the track is taken and the clusters with the smallest distance of closest approach to the track are discarded until their energy is approximately equal to the track energy.

The calibration of these combined objects is done via a recently developed energy weighting scheme of the LAr calorimeter as described in ref. [92] and references therein. In addition, reweighting factors have been applied to the reconstructed jets in order to match their reconstructed transverse momentum  $P_{T,\text{rec}}^{\text{Jet}}$  to their generated transverse momentum  $P_{T,\text{gen}}^{\text{Jet}}$ . The reweighting factors have been derived from the investigation of a NC DIS sample using the RAP-GAP model. The selection criteria for the NC DIS sample are listed in tab. 4.14 and similar to those used in ref. [89]. The kinematic quantities  $y$  and  $Q^2$  have been reconstructed using the electron method which uses only the energy and polar angle of the reconstructed electron (see e.g. ref. [89]). Jets are selected as described in sec. 4.4.1. The electron selection criteria (tab. 4.6) have been slightly modified, *i.e.* the  $P_T$  requirement for the electron has been replaced by a cut on the electron energy ( $E^e > 15$  GeV). Fig. 4.12 shows that the  $P_{T,\text{rec}}^{\text{Jet}}/P_{T,\text{gen}}^{\text{Jet}}$  balance lies within 2%, corroborated by both the  $P_{T,\text{rec}}^{\text{Jet}}$  and the polar angle distributions. In the framework of this analysis, the resulting jet calibration has also been studied in ref. [3] by looking at the jet-electron  $P_T$  balance in NC DIS events.

Essential for a jet analysis is also the description of the jet calibration by the simulation for multi-jet events, whose main contribution arises from photoproduction processes (see sec. 2.2). Therefore it is reasonable to verify the jet calibration in the regime of photoproduction. A di- and a 3-jet photoproduction sample have been studied. The corresponding selection criteria are listed in tab. 4.15. The  $P_T$  requirements for the 3-jet sample have been chosen with respect to the analysis presented in chap. 5.

$\cancel{P}_T < 15 \text{ GeV}$
QBGFMAR background finder bits number 0-8 required to be false
$E^e > 15 \text{ GeV}$
electron selection criteria (tab. 4.6)
$0.1 < y < 0.9$
$Q^2 < 200 \text{ GeV}^2$
$45 \text{ GeV} < \sum_i E_i - P_{z,i} < 65 \text{ GeV}$

**Table 4.14:** The selection criteria for the NC DIS sample.

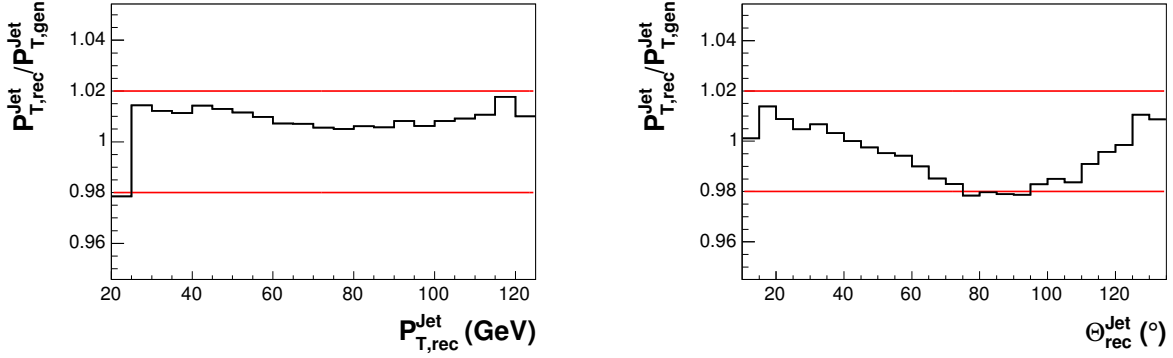


**Figure 4.12:** Jet calibration.  $P_{T,rec}^{Jet}/P_{T,gen}^{Jet}$  balance for the selected RAPGAP sample as a function of the  $P_{T,rec}^{Jet}$  (left) and polar angle  $\Theta_{rec}^{Jet}$  (right).

Figs. 4.13a and 4.13c show the jet-jet  $P_T$  balance ( $P_{T,bal}$ ) for a photoproduction dijet sample as a function of the pseudorapidity  $\eta^{Jet1}$  and the transverse momentum  $P_T^{Jet1}$  of the leading jet, respectively, for both HERA I data and MC (PYTHIA) samples. To reduce the effect that the leading jet has a higher  $P_T$  than the second jet,  $P_{T,bal}$  is calculated as the ratio of the  $P_T$  of the jet with the highest  $\phi$ -value to the  $P_T$  of the other jet. Figs. 4.13e and 4.13g display the relative hadronic energy scale, *i.e.* the cross-ratio of the  $P_T$  balance of the data ( $P_{T,bal}^{Data}$ ) and the  $P_T$  balance of the MC ( $P_{T,bal}^{MC}$ ) as a function of  $\eta^{Jet1}$  and  $P_T^{Jet1}$ . Both distributions of the relative hadronic energy scale are described within an uncertainty of 2%. Figs. 4.13b,d, f and 4.13h show the analogue distributions for the  $P_T^{bal}$  of the leading jet with the hadronic rest. The hadronic rest consists of the total hadronic system excluding the leading jet. Also these figures suggest a relative hadronic energy scale uncertainty of 2%. Figs. 4.14a-h show the corresponding figures for a 3-jet photoproduction sample. For the jet-jet  $P_T$  balance, the  $P_T$  of the jet with the highest  $\phi$ -value is balanced with the other two selected jets. The relative hadronic energy scale uncertainty is again described within 2%.

The hadronic calibration plots from the NC DIS [3] and photoproduction samples show that the data is described by the simulation in all regions of the detector. They justify a systematic uncertainty of the relative hadronic energy scale in the LAr calorimeter of 2%.

$p_T < 20 \text{ GeV}$
QBGFMAR background finder bits number 0-8 required to be false
$E^e < 5 \text{ GeV}$
dijet sample: $P_T^{Jet1, Jet2} > 20 \text{ GeV}$
3-jet sample: $P_T^{Jet1, Jet2, Jet3} > 25, 20, 5 \text{ GeV}$
jet quality criteria as defined in section 4.4.1
$-0.5 < \eta^{Jet} < 2.5$
$0.1 < y_{JB} < 0.9$

**Table 4.15:** The selection criteria for the di- and 3-jet photoproduction samples.

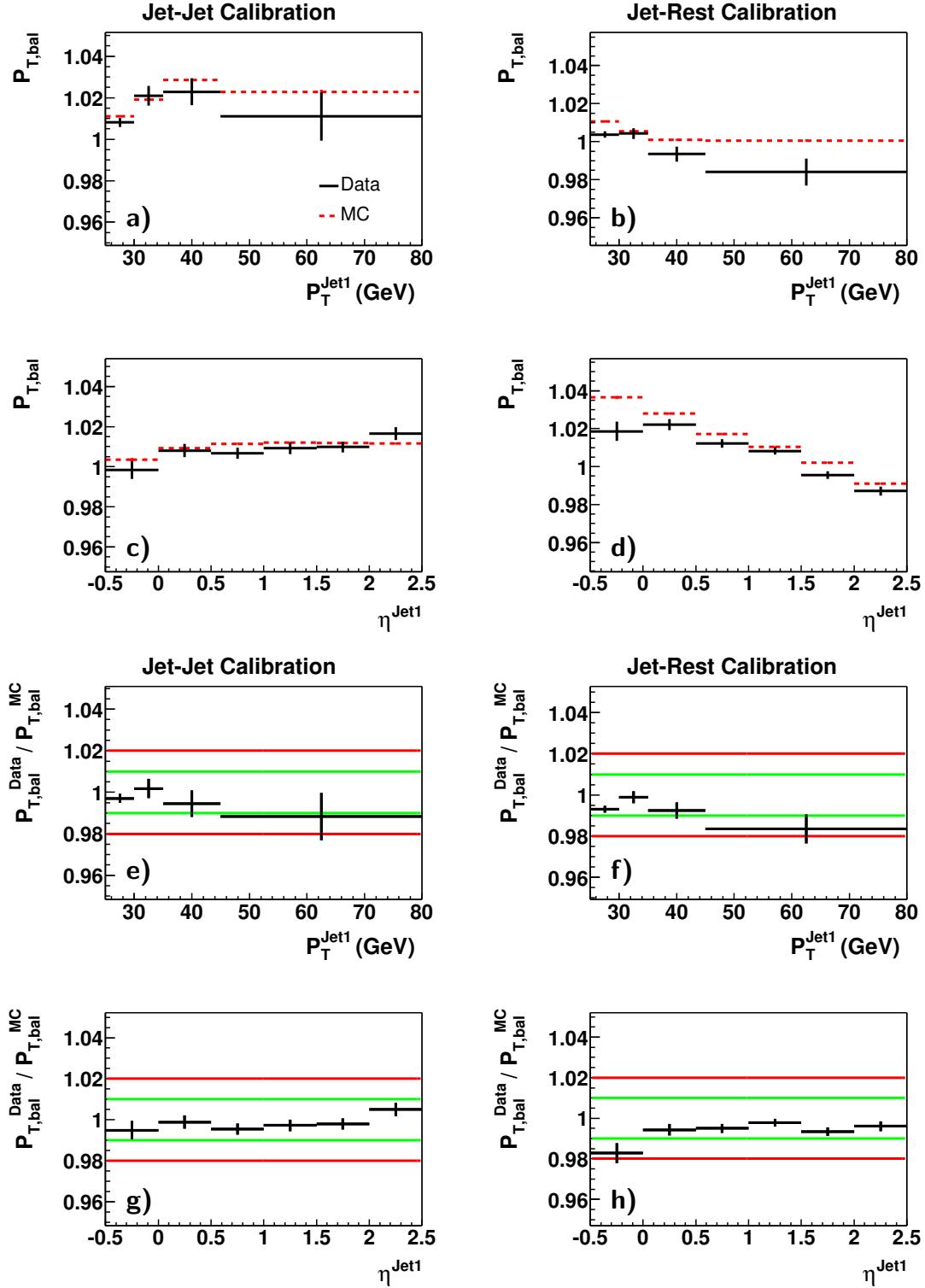


**Figure 4.13:** Mean jet-jet and jet-rest  $P_T$  balance distributions for data and MC (PYTHIA) samples as a function of the  $P_T$  and the pseudorapidity  $\eta$  of the leading jet (figs. a, b, c and d). A dijet photoproduction data sample is used. Figs. c, d, e and f show the ratio of the jet-jet and jet-rest  $P_T$  balance of the data to the corresponding MC generator prediction as a function of  $P_T$  and  $\eta$  of the leading jet.

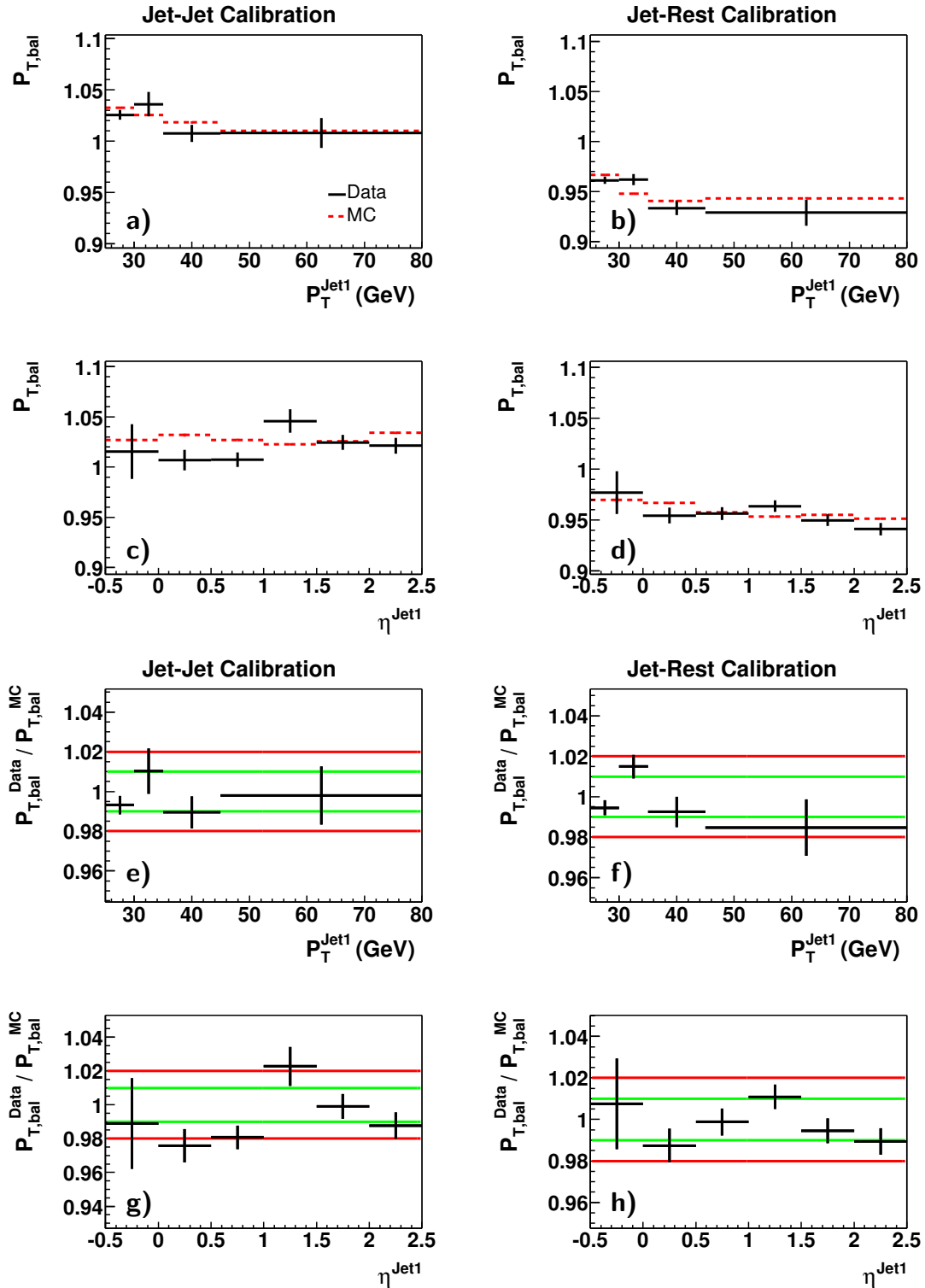


**Figure 4.14:** Mean jet-jet and jet-rest  $P_T$  balance distributions for data and MC (PYTHIA) samples as a function of the  $P_T$  and the pseudorapidity  $\eta$  of the leading jet (figs. a, b, c and d). A 3-jet photoproduction data sample is used. Figs. c, d, e and f show the ratio of the jet-jet and jet-rest  $P_T$  balance of the data to the corresponding MC generator prediction as a function of  $P_T$  and  $\eta$  of the leading jet.

## 4.7 Trigger

The main trigger for events with high transverse momentum is provided by the LAr calorimeter. The trigger efficiency is close to 100% for events having an electromagnetic deposit in the LAr calorimeter originating from an electron or a photon with a  $P_T$  greater than 20 GeV [9]. Events triggered only by jets have a trigger efficiency above 90% for  $P_T > 20$  GeV and nearly 100% for  $P_T > 25$  GeV [81]. For events with high  $\cancel{P}_T$ , determined from an imbalance in transverse momentum measured in the calorimeter  $P_T^{\text{calo}}$ , the trigger efficiency is  $\gtrsim 90\%$  for  $P_T^{\text{calo}} > 20$  GeV [93]. Events only triggered by muons have a trigger efficiency above 70% [94].

## 4.8 Resolution

The search algorithm used in this analysis and described in sec. 4.12.1 needs the resolutions of the researched quantities  $\sum P_T$  and  $M_{\text{all}}$  as input parameters. Therefore, the resolution of these observables have to be studied. In addition, the resolution allows to see if observables are measured systematically too low or too high. The resolutions of  $\sum P_T$  and  $M_{\text{all}}$ , as well as their dependence on  $\sum P_T$  and the  $M_{\text{all}}$ , respectively, are investigated in detail within the framework of this analysis in ref. [3].

## 4.9 Efficiencies and Purities

Resulting from the object identification criteria purities and efficiencies are estimated with the SM MC samples (see tab. 4.1). A purity  $\mathcal{P}$  is defined for each event class as the ratio of SM events reconstructed in the event class in which they have been generated to the total number of reconstructed events in this class, *i.e.*

$$\mathcal{P} = \frac{N_{\text{rec} \wedge \text{gen}}(\text{event class})}{N_{\text{rec}}(\text{event class})},$$

where  $N_{\text{rec}}$ ,  $N_{\text{gen}}$  and  $N_{\text{rec} \wedge \text{gen}}$  are the number of events reconstructed, generated and both reconstructed and generated in the considered event class, respectively. For event classes populated by SM processes the purity is the fraction of rightly reconstructed events and is given in tab. 4.16. Event classes without a sizeable SM expectation (*e.g.*  $\gamma\text{-}\gamma$  or  $\mu\text{-}\mu\text{-}\mu$  event class) are often only populated by a very small fraction of background events and therefore a definition of purity makes no sense for these event classes.

The selection efficiency is defined as the ratio of SM events reconstructed in the event class in which they have been generated to the total number of generated events in this class, *i.e.*

$$\mathcal{E} = \frac{N_{\text{rec} \wedge \text{gen}}(\text{event class})}{N_{\text{gen}}(\text{event class})}.$$

These efficiencies can be used to derive a rough limit for new physics processes.

Both the efficiency and purity are derived as a function of the sum of transverse momenta  $\sum P_T$  and as a function of the invariant mass  $M_{\text{all}}$  of the objects. These distributions can be found in ref. [3]. Mean values are given in tab. 4.16 for all event classes with a sizeable SM expectation. The object phase space requirements have also been applied on generator level. Most purities and efficiencies are above 60%. The highest efficiencies are above 90% for the  $j$ - $j$  and  $j$ - $j$ - $j$  event classes. The  $j$ - $\gamma$  and  $j$ - $j$ - $\gamma$  event classes have purities of less than 40%. This is due to the large background of NC DIS events in these event classes.

Event class	Purity $\mathcal{P}$ (%)	Efficiency $\mathcal{E}$ (%)
$j$ - $j$	80-100	80-100
$e$ - $j$	90-100	70
$\mu$ - $j$	80-90	50-55
$j$ - $\nu$	85-95	75-90
$e$ - $\nu$	50-80	40-50
$e$ - $e$	30-70	40-50
$e$ - $\mu$	90	40-50
$\mu$ - $\mu$	95-100	25-30
$j$ - $\gamma$	20-40	30-50
$e$ - $\gamma$	70	50-60
$\nu$ - $\gamma$	70-80	20-40
$j$ - $j$ - $j$	70-80	80-95
$e$ - $j$ - $j$	70-90	60
$j$ - $j$ - $\nu$	60-80	60-85
$e$ - $e$ - $j$	40-70	20
$e$ - $e$ - $e$	30-70	20-70
$j$ - $\mu$ - $\mu$	50-90	20-50
$e$ - $\mu$ - $\mu$	60-70	20-40
$e$ - $j$ - $\nu$	50-70	40-50
$\mu$ - $j$ - $\nu$	65	40-50
$j$ - $j$ - $\gamma$	5-25	10-20
$e$ - $j$ - $\gamma$	40-60	30-45
$j$ - $\nu$ - $\gamma$	70-100	30-50
$j$ - $j$ - $j$ - $j$	70-90	60-80
$e$ - $j$ - $j$ - $j$	50-80	30-70
$j$ - $j$ - $j$ - $\nu$	30-90	30-80
$e$ - $j$ - $j$ - $j$	100	20

**Table 4.16:** Mean values of efficiencies  $\mathcal{E}$  and purities  $\mathcal{P}$  in the  $M_{\text{all}}$  and  $\sum P_T$  distributions for some event classes.

## 4.10 Systematic Uncertainties

This section describes the experimental and theoretical systematic uncertainties which are considered. Experimental systematic uncertainties arising from the measurement of the objects are presented in tab. 4.17. The experimental quantities are varied by the specified numbers for all objects.

- The electromagnetic energy scale uncertainty is determined to be 1% if the  $z$  position of the electromagnetic particle's impact on the LAr calorimeter is in the backward part ( $z < -145$  cm), 0.7% in the central part ( $-145 < z < 20$  cm), 1.5% for  $20 < z < 100$  cm and 3% in the forward part ( $z > 100$  cm) (see sec. 4.5). The polar angle uncertainty of collimated electromagnetic clusters varies, depending on the polar angle, between 1 and 3 mrad [9]. The corresponding uncertainty on the azimuthal angle is 1 mrad [4]. The electron and photon identification efficiencies have uncertainties arising from inaccuracies in the simulation of tracks in the inner tracking system and of hits in the CIP. The measured tracking efficiency is described by the simulation to a precision ranging from 2% for polar angles above  $37^\circ$  to 7% in the forward region [3]. The measured and the simulated hit efficiency of the CIP agree within 0.5% [3].
- The hadronic energy scale of the LAr calorimeter has an uncertainty of 2% (sec 4.6). The uncertainty on the jet polar angle determination is 5 mrad for  $\theta < 30^\circ$  and 10 mrad for  $\theta > 30^\circ$ .
- The muon energy scale uncertainty amounts to 5% [4]. The uncertainty on the polar and azimuthal angle determinations are 3 mrad and 1 mrad, respectively [4].
- The uncertainties on the trigger efficiencies are taken into account according to the object with the highest trigger efficiency. The uncertainty on the trigger efficiency is estimated to be 3% if the event is triggered by a jet [77], and 5% if it is triggered by a muon [94]. Otherwise, the uncertainty on the trigger efficiency is negligible.
- An overall normalisation uncertainty of 1.5% results from the luminosity measurement.

Object	Energy Scale Unc.	$\theta$ Unc. (mrad)	$\phi$ Unc. (mrad)	Identification Efficiency Unc.
Jet	2%	5 – 10	–	–
Electron	0.7 – 3%	1 – 3	1	2 – 7%(Tracking) $\oplus$ 0.5%(CIP)
Photon	0.7 – 3%	1 – 3	1	2 – 7%(Tracking) $\oplus$ 0.5%(CIP)
Muon	5%	3	1	5%

**Table 4.17:** *The uncertainties attributed to the object measurements.*

Depending on the dominant production process, different theoretical uncertainties are used. They are listed in tab. 4.18. An additional theoretical uncertainty of 20% is applied for each jet dominantly produced by parton shower processes (e.g.  $j$ - $j$ - $j$  event class). A model uncertainty of 50% is added to NC DIS events with missing transverse momentum above 20 GeV and a high  $P_T$  electron. This uncertainty is estimated by a comparison of low  $P_T$  NC DIS events with the SM prediction [3].

Process(es)	Uncertainty
$ep \rightarrow jjX$ and $ep \rightarrow j\gamma X$	15%
$ep \rightarrow j\nu X$ and $ep \rightarrow jeX$	10%
$ep \rightarrow jj\nu X$ and $ep \rightarrow jjeX$	15%
$ep \rightarrow \mu\mu$ and $ep \rightarrow ee$	3%
$ep \rightarrow WX$ and $ep \rightarrow WjX$	15%
$ep \rightarrow e\gamma X$ and $ep \rightarrow e\gamma j$	10%
$ep \rightarrow e\gamma p$	5%

**Table 4.18:** The uncertainties attributed to the different processes of the SM expectation.

All systematic errors are added in quadrature. The resulting total uncertainty on the predicted number of events varies e.g. for the  $e$ - $j$  event class between 10% and 35% and for the  $j$ - $j$  event class between 20% and 60%, increasing with  $P_T$ . Essentially for the search algorithm (sec. 4.12.1) are smooth systematic uncertainties as a function of the researched observable. Therefore all systematic uncertainties considered as a function of a researched observable are fitted. Fig. 4.15 shows the fitted distribution of the systematic uncertainties on the predicted number of events as a function of  $M_{\text{all}}$  for various event classes. The figures in ref. [95] show the distributions as a function of  $M_{\text{all}}$  and of  $\sum P_T$  for the event classes or distributions which have not been presented in this section.



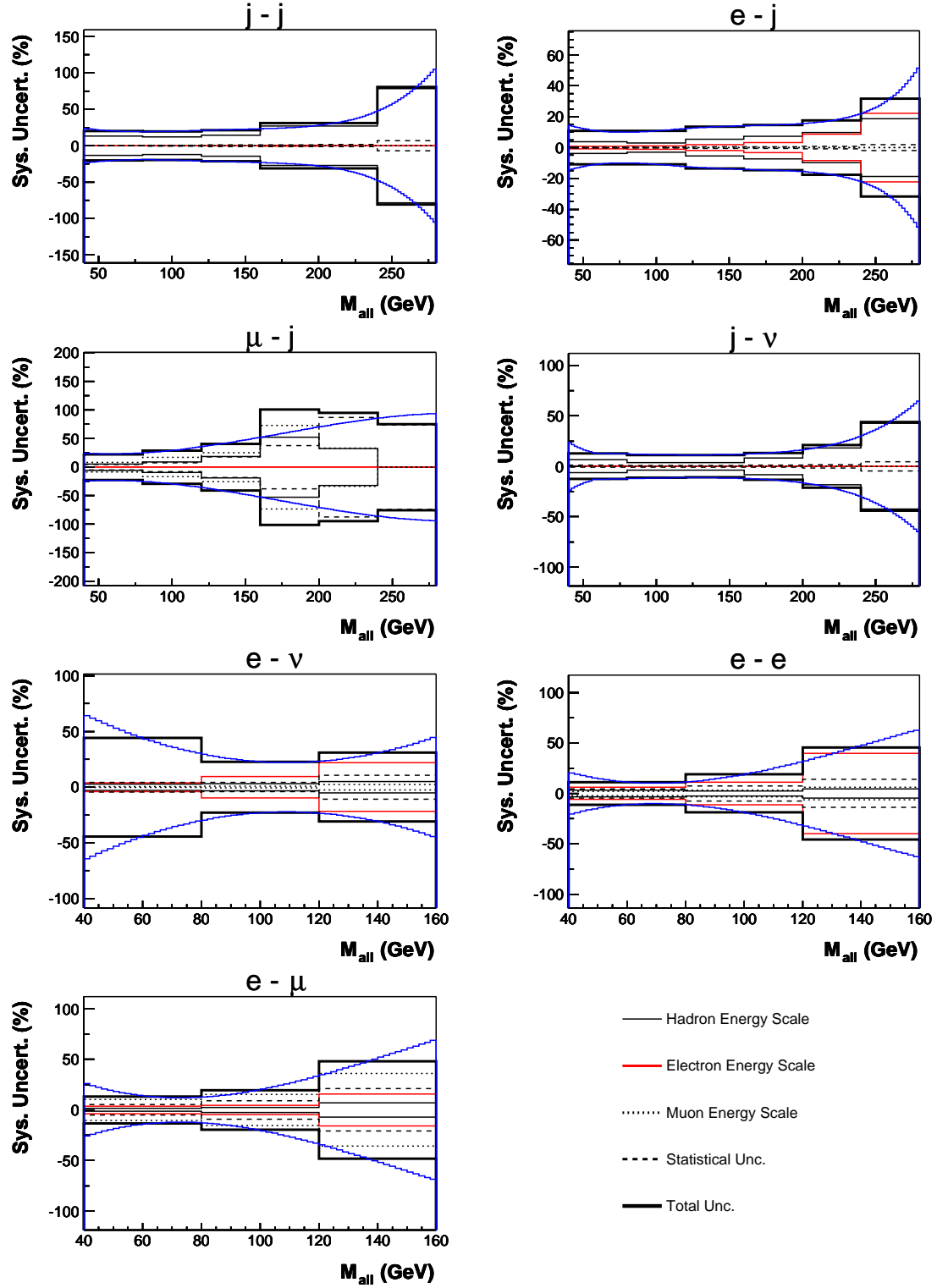


**Figure 4.15:** Systematic uncertainties on the predicted number of events as a function of  $M_{\text{all}}$  for different event classes. Only the total uncertainty and the corresponding fit, as well as the uncertainties arising from the energy scales and the statistics are shown.

## 4.11 Results

All experimentally measurable event classes have been investigated. The  $\mu\nu$  event class was found to be overwhelmed by background from low  $P_T$  photoproduction and was unmeasurable. It was discarded from the analysis procedure [3]. The event yields for data and SM expectation are presented for all event classes in fig. 4.16. A good overall agreement between data and SM expectation is observed for most of the event classes. In the following discussion only the event classes having a SM expectation greater than 0.1 events will be considered (see fig. 4.17). All the other event classes do not contain any data events. As a complement to this analysis, the control distributions of the kinematical quantities of the selected objects are presented for all event classes in ref. [95].

The dominant processes at HERA, *i.e.* photoproduction, NC DIS and CC DIS processes, can be found in the  $j$ - $j$ ,  $e$ - $j$  and  $j$ - $\nu$  event class, respectively. The data event yields in these event classes are in good agreement with the SM expectation. Likewise, the  $j$ - $j$ - $j$ ,  $e$ - $j$ - $j$ ,  $e$ - $j$ - $j$ - $j$ ,  $j$ - $j$ - $\nu$  and  $j$ - $j$ - $j$ - $\nu$  event classes correspond to the same dominant processes with the inclusion of additional jet production due to higher order QCD processes. The event yields of these event classes are also well described by the SM prediction. Event classes containing a radiative photon are the  $j$ - $j$ - $\gamma$ ,  $e$ - $j$ - $\gamma$  and  $\nu$ - $\gamma$  event classes and correspond, respectively, to photoproduction, NC DIS and CC DIS processes with the radiation of a photon. These event classes also agree with the expectation. The  $e$ - $\gamma$  event class, which is dominated by QED Compton scattering processes (95%), is also in good agreement with the expectation. No radiative CC DIS event is observed in the  $j$ - $\nu$ - $\gamma$  event class for  $1.0 \pm 0.2$  expected. The  $j$ - $\gamma$  event class is well described by the SM, but the purity is low (20 – 40%) due to the high NC DIS background in this event class.

A discrepancy between data and SM expectation is observed in the  $\mu$ - $j$ - $\nu$  event class, where four events are found for an expectation of  $0.7 \pm 0.2$ . This event class corresponds to typical event topologies arising from  $W$  production with subsequent leptonic decay. The deviation was already investigated in ref. [4] and will be further discussed in sec. 4.12 and chap. 5. Similarly, the  $e$ - $\nu$  and  $e$ - $j$ - $\nu$  event classes are also populated by events arising from  $W$  production. In the  $e$ - $\nu$  event class a slight deficit of eight data events compared to an expectation of  $19.9 \pm 8.0$  is observed. This event class is dominated by background events from NC DIS where possible fluctuations in the hadronic energy measurement or limited detector acceptance can produce missing transverse momentum. In the  $e$ - $j$ - $\nu$  event class, two data events are observed for an expectation of  $0.9 \pm 0.2$ . Most of the interesting  $e$ - $j$ - $\nu$  events reported in ref. [4] have an electron with a  $P_T$  below 20 GeV and are therefore not selected in the present analysis (app. B).

Another discrepancy to the SM expectation has been reported by the H1 collaboration concerning multi-electron events at high transverse momenta [96]. In the present analysis, the  $e$ - $e$  event class is populated with 85% by electron pair production with eight measured data events for an expectation of  $10.7 \pm 1.1$ . All di-electron events mentioned in the dedicated multi-electron search and available in the phase space of this analysis are selected; no tri-electron event is identified due to the requirement of high transverse momentum (app. B). In the region

$M_{\text{all}} > 100 \text{ GeV}$ , three events are observed and  $1.15 \pm 0.25$  are expected. The higher SM prediction compared to ref. [96] is due to background coming from fake electrons with  $\theta < 20^\circ$  and a higher di-electron selection efficiency due to the increased phase space.

The  $e\text{-}\mu$  and  $\mu\text{-}\mu$  event classes are dominated by muon pair production from two-photon reactions to approximately 95% and 100%, respectively. The  $e\text{-}\mu$  event class is populated when the scattered electron and only one of the muons are selected. In the  $e\text{-}\mu$  and  $\mu\text{-}\mu$  event classes, four and five events are observed compared to an expectation of  $4.9 \pm 0.6$  and  $2.6 \pm 0.6$ , respectively. Muon pair production processes also contribute to  $\approx 85\%$  in the  $\mu\text{-}j$  event class, where again a good agreement is found.

Some discrepancies on the total event yields can be observed in the  $j\text{-}j\text{-}j\text{-}j$  and  $e\text{-}j\text{-}j\text{-}j\text{-}j$  event classes between data and SM expectation. For the  $e\text{-}j\text{-}j\text{-}j\text{-}j$  event class, a low SM expectation of  $\approx 0.05$  is estimated [3]. Events with four high  $P_T$  jets are investigated for the first time at HERA. Since these spectacular events can – in the current MC programs – only be produced via parton shower, it cannot be ensured that the prediction is reliable. No events are found in all other event classes in good agreement with the SM expectation. The expectation of  $\approx 1$  event in the  $\gamma\text{-}\gamma$  event class is dominated by electron-photon events where the electron is misidentified because of cluster track association inefficiency. Contributions of higher order QED processes which could lead to two high transverse momentum photons are not considered. A simple minded count of orders of the electromagnetic coupling  $\alpha$  leads to an expectation of  $\lesssim 1$  event. Finally, the event displays of some outstanding events are presented in app. B.

## 4.12 Search for Deviations from the Standard Model

### 4.12.1 Search Algorithm

In order to quantify the level of agreement between the data and the SM expectation and to identify regions of possible deviations, a new search algorithm has been developed [3]. The calculation of a global significance per event class has been inspired by ref. [74].

Quantities sensitive to new physics signals and easy to measure are the sum of transverse momenta and the invariant mass of all objects. Detailed studies have shown that both quantities have a large finding potential by mixing various signals of new physics into data and MC distributions [3]. The algorithm described in the following was run on these pseudo data samples and was successful in finding the signals. Hence, the invariant mass  $M_{\text{all}}$  and the scalar sum of transverse momenta  $\sum P_T$  of all particles are investigated, considering that signals of new physics are likely to manifest themselves at certain transverse momentum or invariant mass. It turned out that both quantities complement each other in the search for these signals.

The basic design of the search algorithm is very simple:

**Definition of regions** A region is defined as a sample of connected histogram bins. The number of data events  $N_{\text{obs}}$  of a region is given by the sum of all entries found in the bins of the

data histogram. Similarly, the SM expectation  $N_b$  with its total systematic uncertainty  $\delta N_b$  are determined in the same region of the SM histogram. All possible connected regions which have at least the size of twice the resolution are considered.

**Estimation of the probability for each region** A statistical estimator  $p$  is defined to judge which region is of most interest. This estimator is derived from the convolution of the Poisson probability density function (pdf) to account for statistical errors with a Gaussian pdf,  $G(b; N_b, \delta N_b)$ , to include the effect of non-negligible systematics uncertainties and defined via

$$p = \begin{cases} A \int_0^\infty db G(b; N_b, \delta N_b) \sum_{i=N_{\text{obs}}}^\infty \frac{e^{-b} b^i}{i!} & \text{if } N_{\text{obs}} \geq N_b \\ A \int_0^\infty db G(b; N_b, \delta N_b) \sum_{i=0}^{N_{\text{obs}}} \frac{e^{-b} b^i}{i!} & \text{if } N_{\text{obs}} < N_b. \end{cases}$$

The mean of the Gaussian pdf is given by  $N_b$  and the corresponding width by  $\delta N_b$ .  $A$  is a normalisation factor to ensure that the pdf is normalised to unity. If the Gaussian pdf  $G$  is replaced by a Dirac delta function  $\delta(b - N_b)$ , the estimator  $p$  results in an usual Poisson probability. The value of  $p$  gives an estimate of the probability that the SM expectation fluctuates upwards or downwards to the data.

**Determination of the most interesting region** A possible sign of new physics is found (in this search ansatz) if the expectation significantly disagrees with the data. This disagreement is quantified with the estimator  $p$ . The region of greatest interest (of greatest deviation) is the region having the smallest  $p$ -value,  $p_{\text{min}}$ . This method finds narrow resonances, single outstanding events as well as signals spread over large regions of phase space in distributions of any shape.

**Global significance per event class** The fact that somewhere in the studied distribution a fluctuation with a value  $p_{\text{min}}$  occurs is taken into account using the following method.  $\hat{P}$  is defined as the probability to observe a deviation with a  $p$ -value  $p_{\text{min}}$  at any position and width of a region (or with this algorithm) in the investigated distribution. Thus  $\hat{P}$  is the central measure of the significance of the found deviation. To determine  $\hat{P}$ , hypothetical data histograms are produced by dicing in each bin a random event number according to the pdfs of the expectation (again a convolution of Poisson and Gaussian pdfs). For each hypothetical data histogram the algorithm is run to find the region of greatest deviation and to calculate  $p_{\text{min}}$ . The probability  $\hat{P}$  can then be defined as the fraction of hypothetical data histograms with a  $p_{\text{min}}$ -value smaller than the  $p_{\text{min}}$ -value obtained with the real data. This fraction  $\hat{P}$  can be used to compare results of different event classes if the event classes are independent. An event class with small  $\hat{P}$  is of more interest than an event class with large  $\hat{P}$ . Consequently, the event class of most interest for a search is the one with the smallest  $\hat{P}$ -value.

To compare the obtained  $\hat{P}$ -values with an expectation, the data distributions are replaced by distributions from MC experiments. These MC distributions are again hypothetical data distributions. The complete algorithm is applied on these independent sets of MC experiments. In the case that deviations from the SM arise only from statistical or systematical fluctuations, the distribution of  $\hat{P}$ -values obtained in data events are compatible with the distribution of  $\hat{P}$  arising from these MC experiments.

### 4.12.2 Search Results

The final  $\hat{P}$ -values obtained for all event classes are summarised for the  $M_{\text{all}}$  and  $\sum P_T$  distributions in tab. 4.19 and tab. 4.20, respectively. The  $\hat{P}$ -values of the event classes with no data event and a SM expectation  $\lesssim 1$  are 1. Distributions of the invariant mass  $M_{\text{all}}$  and the sum of transverse momenta  $\sum P_T$  together with the regions selected by the algorithm are presented in figs. 4.18-4.22. The  $j$ - $j$ - $j$ - $j$  and  $e$ - $j$ - $j$ - $j$  event classes are not considered in this statistical analysis because their SM prediction is less reliable. The values are compared to the distribution of  $\hat{P}$ -values obtained in MC experiments in fig. 4.23 for the invariant mass distributions and in fig. 4.24 for the  $\sum P_T$  distributions. The distribution of the negative decade logarithm of the  $\hat{P}$ -values,  $-\log \hat{P}$ , is presented. Most  $\hat{P}$ -values range from 0.01 to 0.99 corresponding to event classes where no significant discrepancy between data and SM expectation is observed. These results are in agreement with the expectation from MC experiments.

The largest deviation of the analysis occurs in the  $\mu$ - $j$ - $\nu$  event class, where  $\hat{P}$ -values of 0.010 and 0.0008 are found corresponding to the high  $M_{\text{all}}$  and high  $\sum P_T$  region, respectively. The mass region contains two data events for an expectation of  $0.05 \pm 0.02$ . In the chosen  $\sum P_T$  region, three data events are found, while only  $0.07 \pm 0.03$  are expected. This discrepancy has been studied in ref. [4] and is also discussed in chap. 5.

It is interesting to note that there are four deviations with a  $\hat{P}$ -value  $\lesssim 0.02$  in the  $\sum P_T$  distributions. In the following, the remaining three are briefly discussed. A deficit is observed in the  $e$ - $j$  event class in the  $\sum P_T$  distribution at  $180 \text{ GeV} < \sum P_T < 210 \text{ GeV}$ . For a SM expectation of  $30.4 \pm 5.0$ , only 12 data events are measured, and the derived  $\hat{P}$ -value is 0.02. A  $\hat{P}$ -value of 0.02 is found in the  $e$ - $e$  event class, where three events are observed in the region at high  $\sum P_T$   $100 \text{ GeV} < \sum P_T < 110 \text{ GeV}$  and only  $0.2 \pm 0.08$  are expected. In the  $M_{\text{all}}$  distribution, there is also an excess due to the same events but it is less pronounced ( $\hat{P} = 0.28$ ). The deviation corresponds to an excess of data events also identified in ref. [96]. In the  $\sum P_T$  distribution of the  $\mu$ - $\mu$  event class, two events are measured in the region  $95 \text{ GeV} < \sum P_T < 115 \text{ GeV}$  compared to an expectation of  $0.07 \pm 0.03$  events yielding a  $\hat{P}$ -value of 0.02.

This analysis studies a large number of event classes. Thus there is some chance that a  $\hat{P}$ -value can be small. The likeliness can be calculated that the smallest probability found in the investigated  $M_{\text{all}}$  or  $\sum P_T$  distributions may occur. This is the fraction of MC experiments with a smaller  $\hat{P}$ -value than the smallest one found in the data. This value is found to be about 0.25 for the set of  $M_{\text{all}}$  distributions and about 0.02 for the set of  $\sum P_T$  distributions.

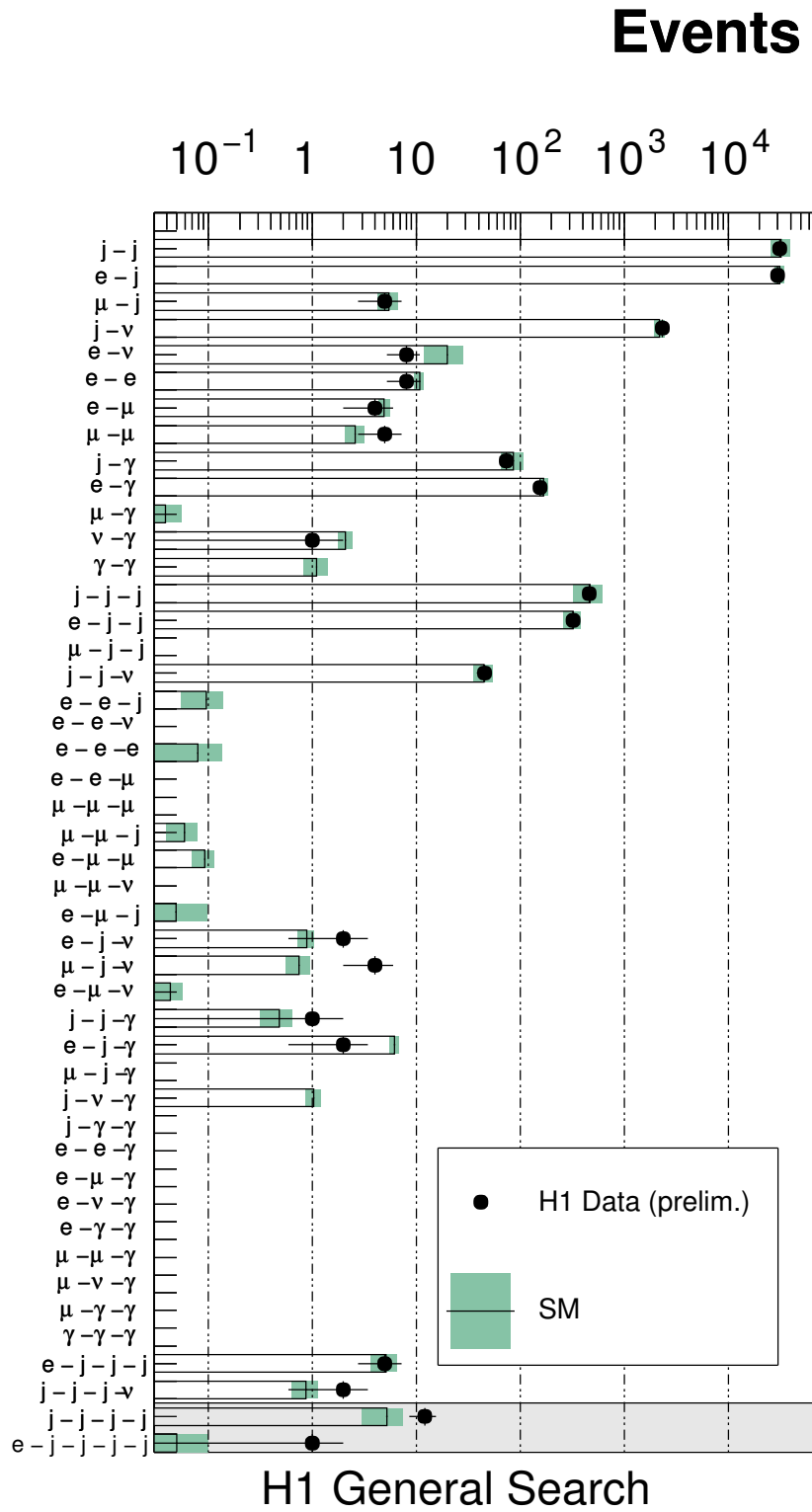


**Figure 4.16:** The data and SM expectation for all 2- and 3-object event classes, as well as for all 4- and 5-object event classes with data. The  $j-j-j-j$  and  $e-j-j-j-j$  event classes (grey area) are not passed through the statistical analysis because the corresponding SM prediction is less reliable.

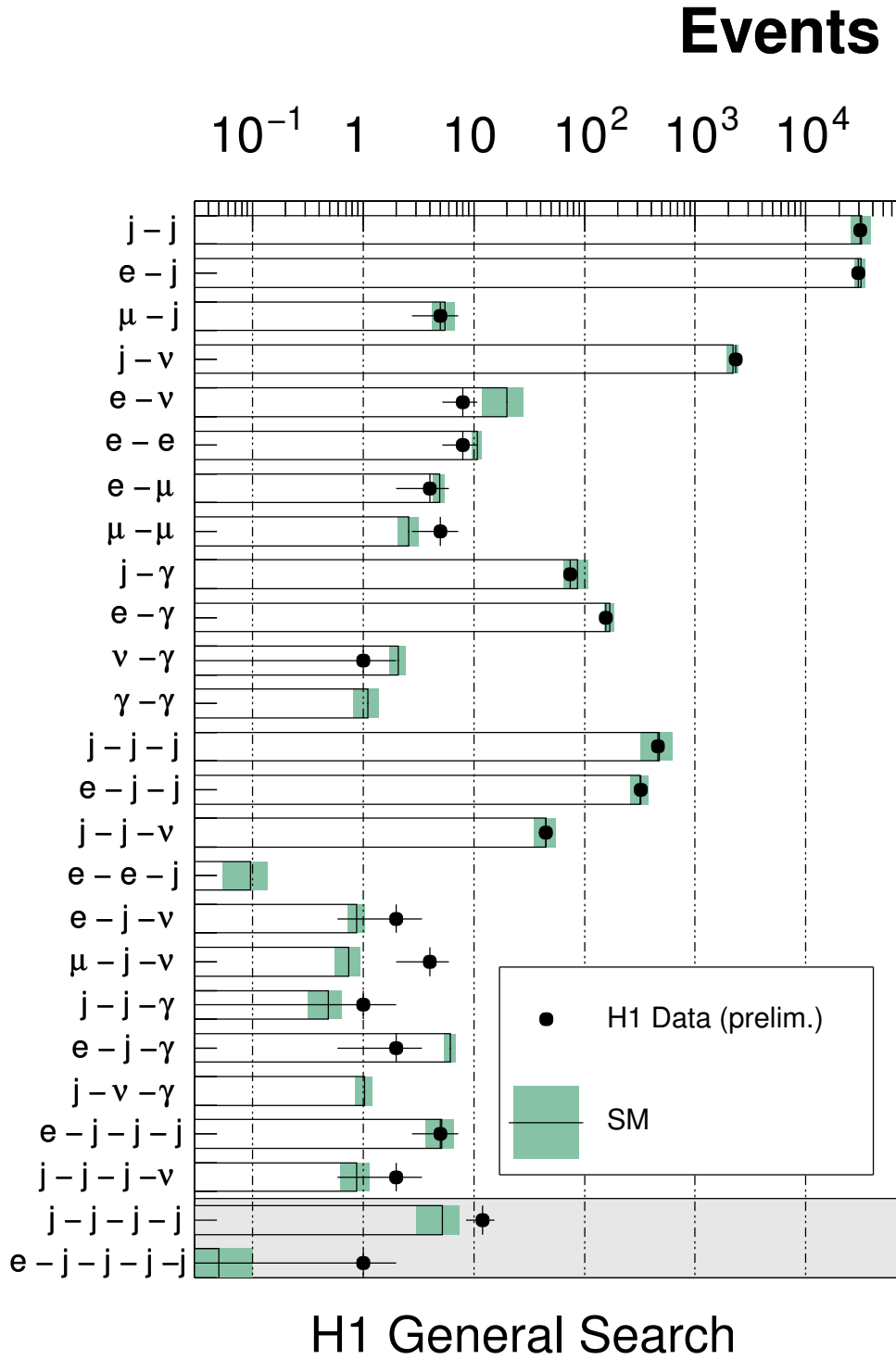


**Figure 4.17:** The data and SM expectation for all event classes with a SM expectation greater than 0.1 events. The  $j-j-j-j$  and  $e-j-j-j-j$  event classes (grey area) are not passed through the statistical analysis because the corresponding SM prediction is less reliable.

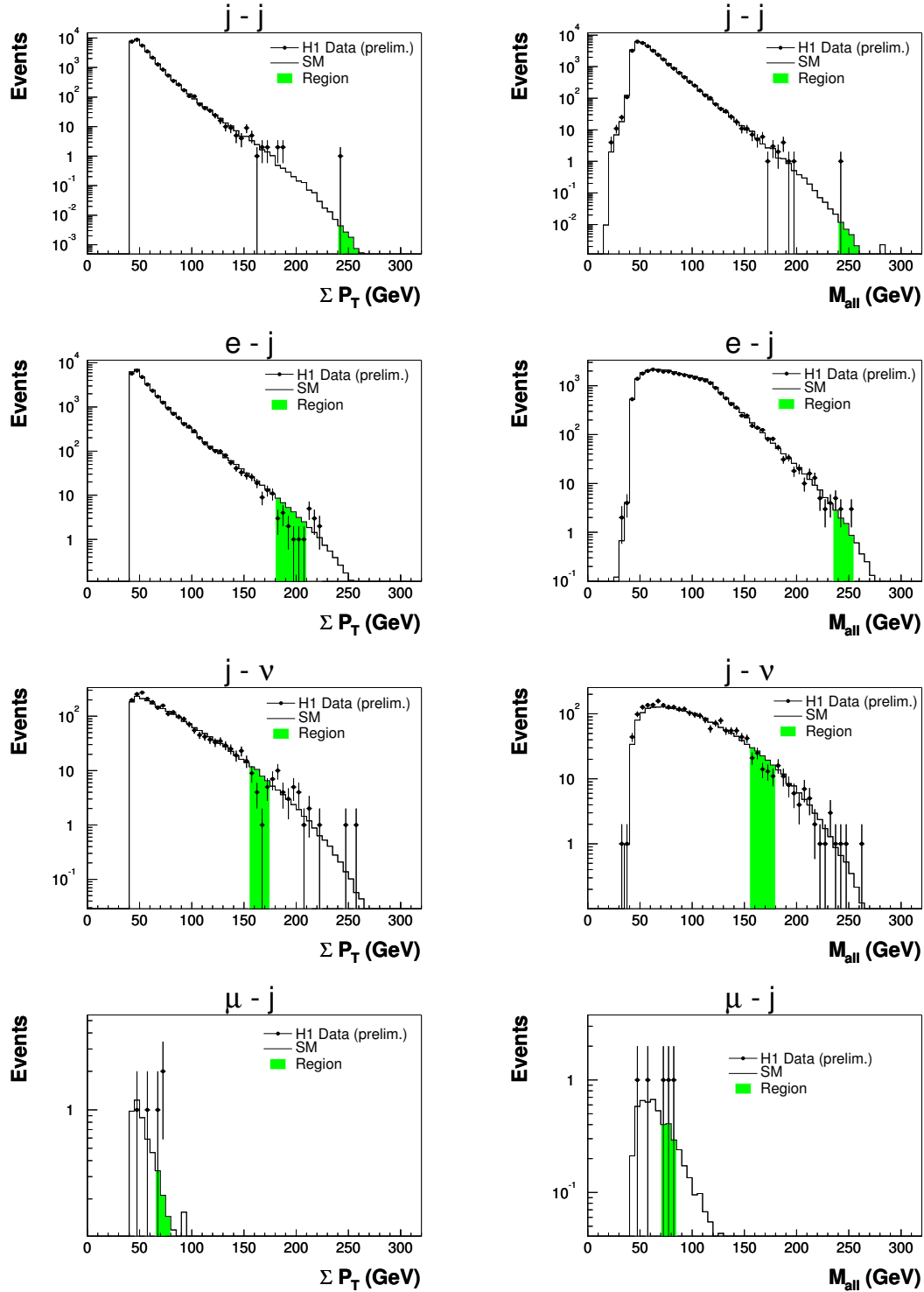


**Figure 4.18:** The number of data events and the SM expectation for various event classes as a function of  $\Sigma P_T$  and of  $M_{all}$ . The shaded regions show the regions of greatest deviation chosen by the search algorithm.



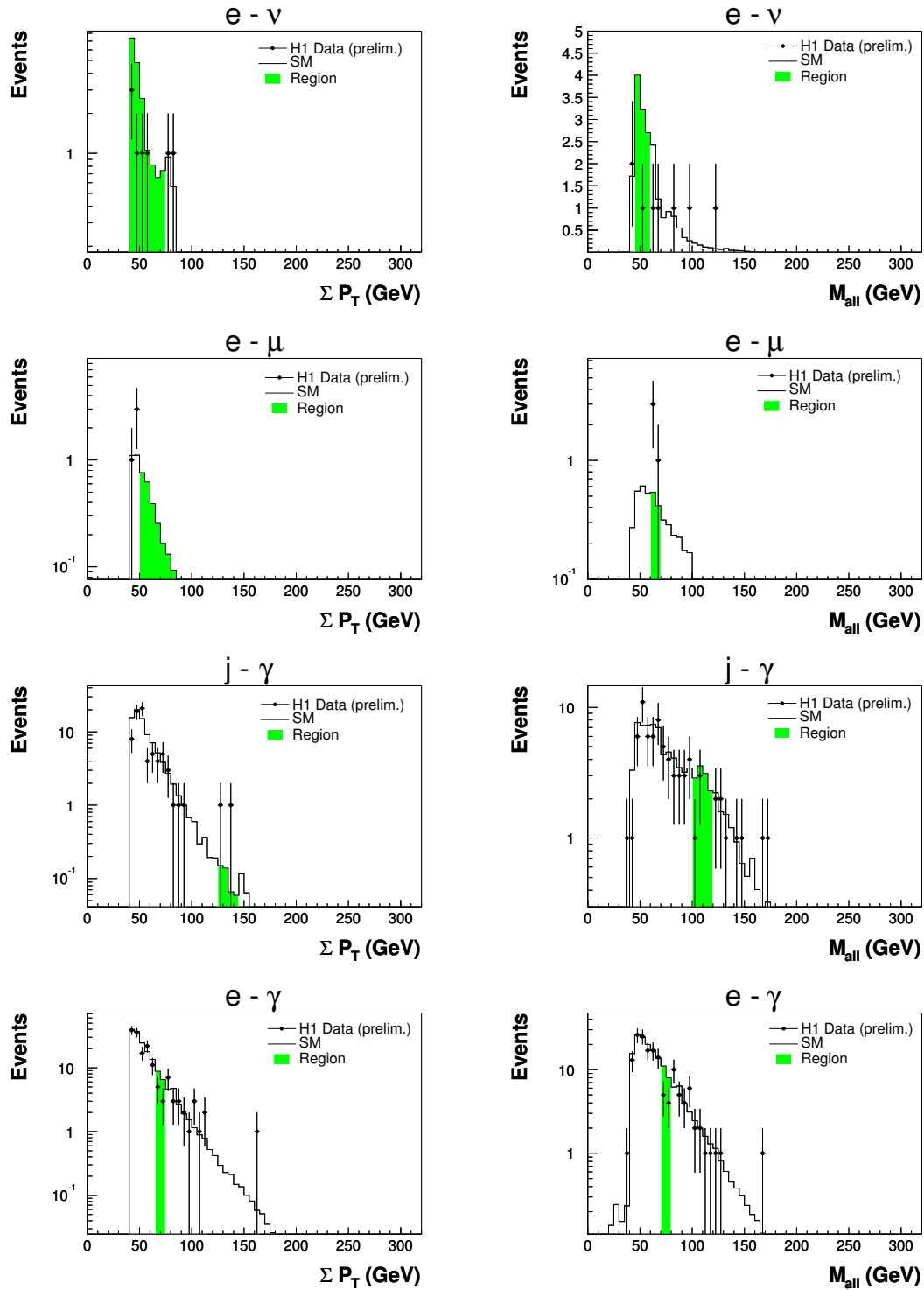


**Figure 4.19:** The number of data events and the SM expectation for various event classes as a function of  $\Sigma P_T$  and of  $M_{\text{all}}$ . The shaded regions show the regions of greatest deviation chosen by the search algorithm.

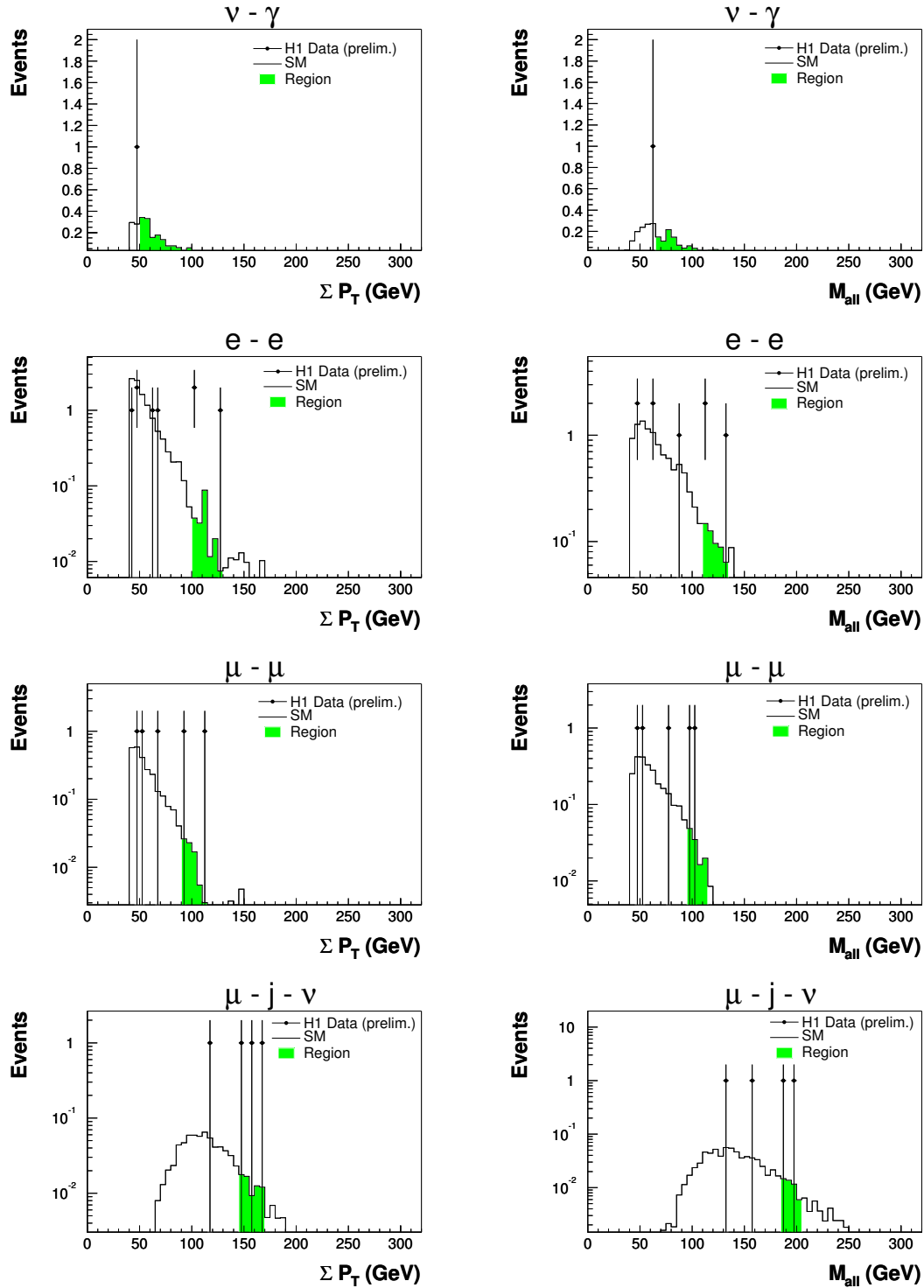


**Figure 4.20:** The number of data events and the SM expectation for various event classes as a function of  $\Sigma P_T$  and of  $M_{\text{all}}$ . The shaded regions show the regions of greatest deviation chosen by the search algorithm.

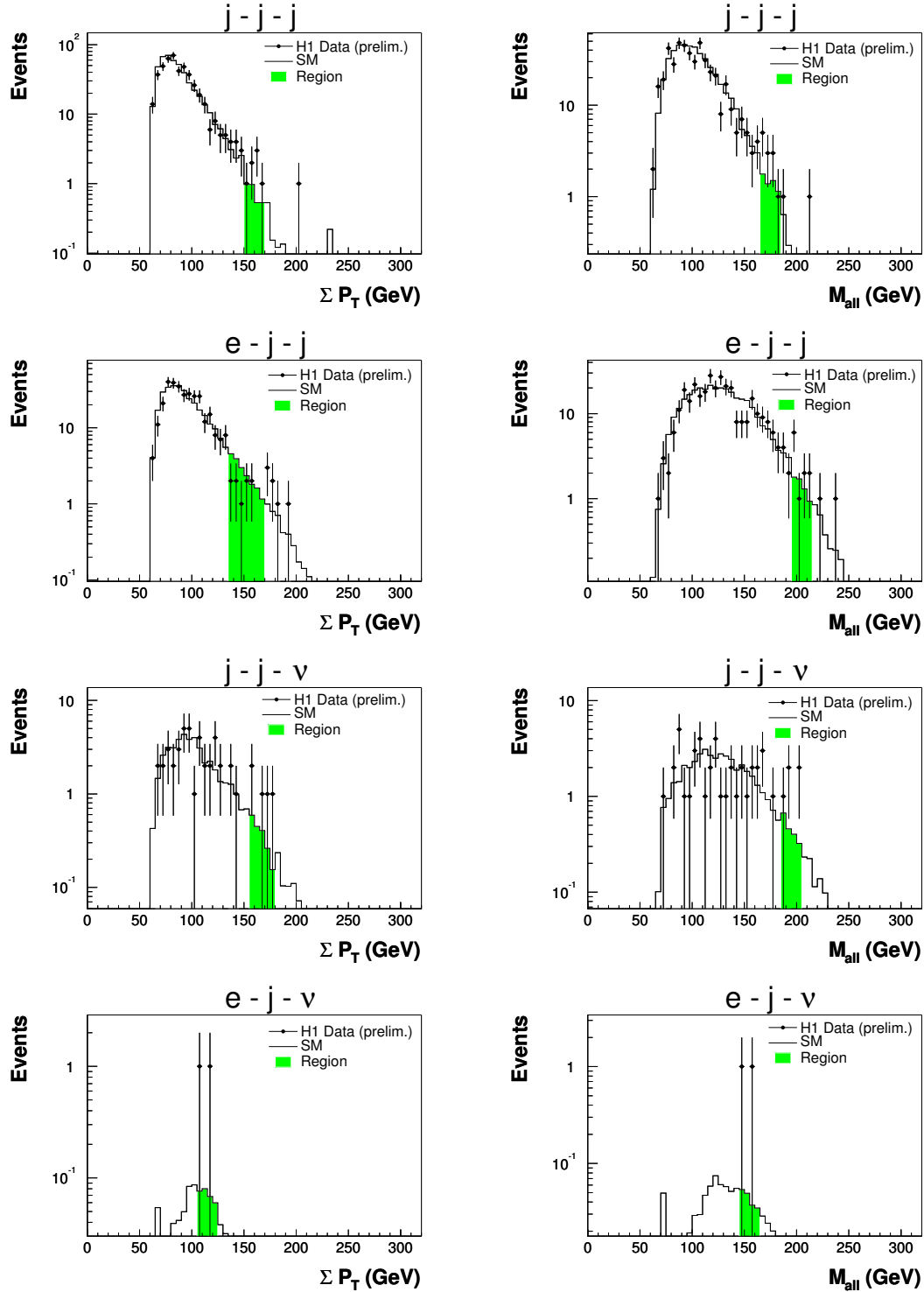


**Figure 4.21:** The number of data events and the SM expectation for various event classes as a function of  $\Sigma P_T$  and of  $M_{all}$ . The shaded regions show the regions of greatest deviation chosen by the search algorithm.

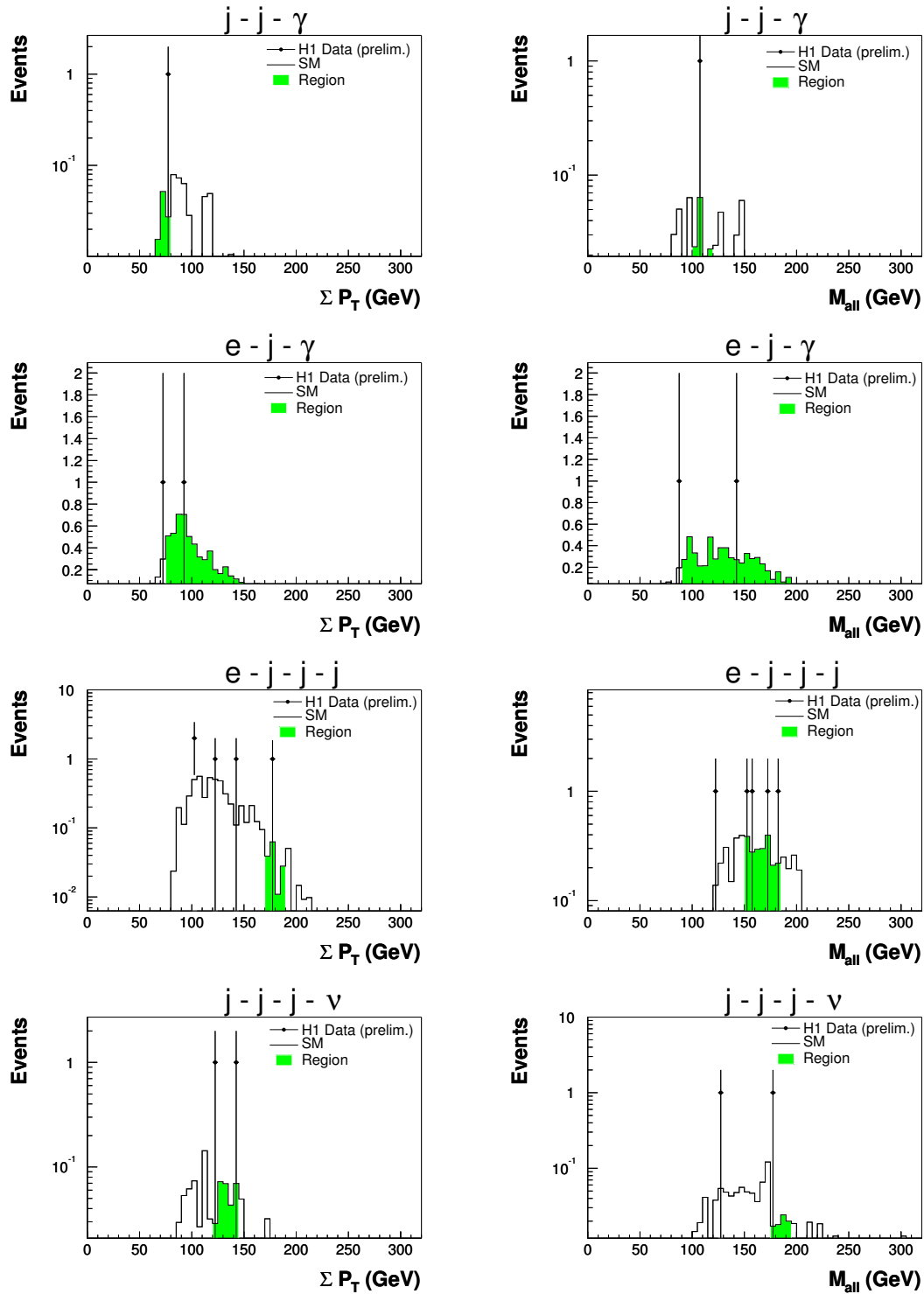


**Figure 4.22:** The number of data events and the SM expectation for various event classes as a function of  $\Sigma P_T$  and of  $M_{all}$ . The shaded regions show the regions of greatest deviation chosen by the search algorithm.

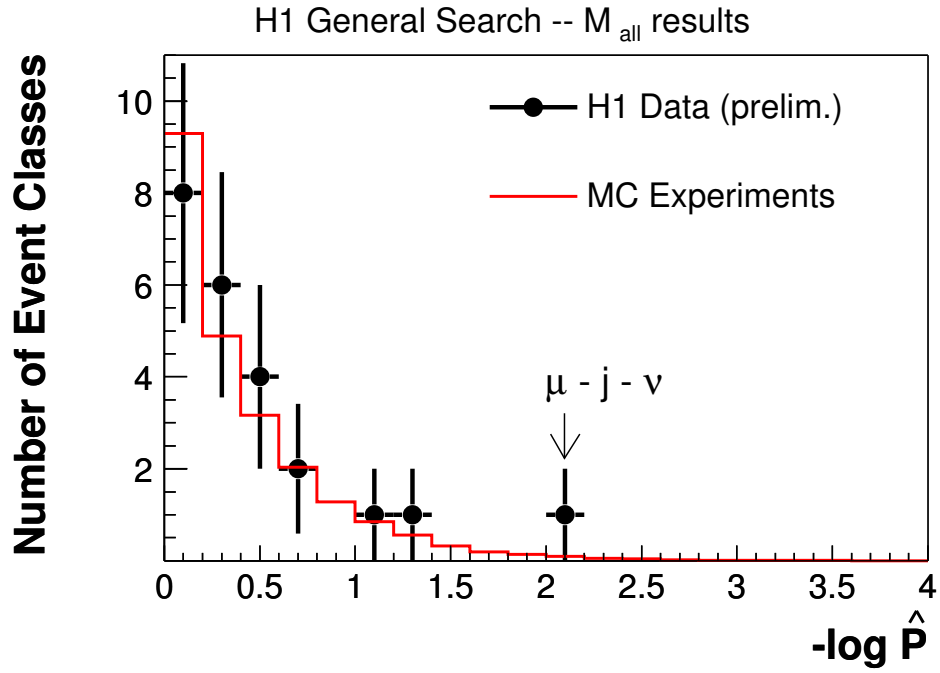


**Figure 4.23:** The  $-\log \hat{P}$  distribution for the data event classes and the expected distribution from MC experiments. The  $M_{\text{all}}$  distributions are tested with the search algorithm. All event classes with a SM expectation greater than 0.1 events, except the  $j-j-j-j$  and  $e-j-j-j-j$  event classes, are considered.

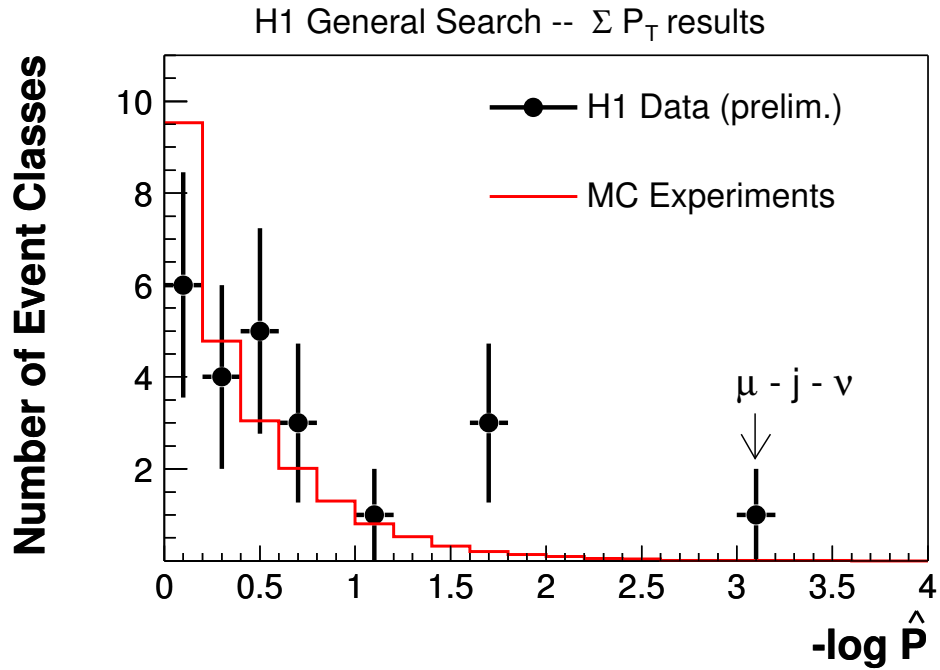


**Figure 4.24:** The  $-\log \hat{P}$  distribution for the data event classes and the expected distribution from MC experiments. The  $\Sigma P_T$  distributions are tested with the search algorithm. All event classes with a SM expectation greater than 0.1 events, except the  $j-j-j-j$  and  $e-j-j-j-j$  event classes, are considered.

Event class	$\hat{P}$	$N_{\text{obs}}$	$N_{\text{exp}} \pm \delta N_{\text{exp}}$	$p$
$j-j$	0.25	1	$0.025 \pm 0.014$	0.026
$e-j$	0.97	11	$7.2 \pm 1.7$	0.15
$\mu-j$	0.68	3	$1.10 \pm 0.27$	0.11
$j-\nu$	0.51	84	$114.7 \pm 14.3$	0.041
$e-\nu$	0.39	1	$9.9 \pm 5.2$	0.044
$e-e$	0.28	3	$0.52 \pm 0.11$	0.017
$e-\mu$	0.20	4	$0.95 \pm 0.12$	0.017
$\mu-\mu$	0.05	2	$0.12 \pm 0.04$	0.007
$j-\gamma$	0.62	4	$11.9 \pm 3.8$	0.062
$e-\gamma$	0.41	9	$19.0 \pm 2.0$	0.015
$\nu-\gamma$	1.	0	$0.96 \pm 0.37$	0.406
$j-j-j$	0.38	12	$5.8 \pm 2.0$	0.047
$e-j-j$	0.57	11	$5.7 \pm 1.3$	0.053
$j-j-\nu$	0.66	5	$1.86 \pm 0.45$	0.050
$e-j-\nu$	0.10	2	$0.18 \pm 0.04$	0.014
$\mu-j-\nu$	0.01	2	$0.046 \pm 0.02$	0.0012
$j-j-\gamma$	0.39	1	$0.12 \pm 0.07$	0.112
$e-j-\gamma$	0.43	1	$5.76 \pm 1.6$	0.049
$e-j-j-j$	0.91	4	$2.10 \pm 0.9$	0.19
$j-j-j-\nu$	0.40	1	$0.08 \pm 0.07$	0.091

**Table 4.19:** The  $\hat{P}$ -values of the regions derived with the search algorithm using the  $M_{\text{all}}$  distributions for event classes with at least one data event (except the  $j-j-j-j$  and  $e-j-j-j-j$  event classes). In addition, the data events  $N_{\text{obs}}$  and the SM expectation  $N_{\text{exp}}$  with its uncertainty  $\delta N_{\text{exp}}$ , as well as the  $p$ -value are given for each of these regions.

Event class	$\hat{P}$	$N_{\text{obs}}$	$N_{\text{exp}}$	$\pm$	$\delta N_{\text{exp}}$	$p$
$j$ - $j$	0.065	1	0.010	$\pm$	0.005	0.010
$e$ - $j$	0.02	12	30.4	$\pm$	5.0	0.0032
$\mu$ - $j$	0.29	3	0.70	$\pm$	0.20	0.038
$j$ - $\nu$	0.17	19	36.6	$\pm$	6.4	0.020
$e$ - $\nu$	0.38	6	18.0	$\pm$	7.4	0.073
$e$ - $e$	0.02	3	0.20	$\pm$	0.08	0.0015
$e$ - $\mu$	0.51	0	2.70	$\pm$	0.4	0.07
$\mu$ - $\mu$	0.02	2	0.074	$\pm$	0.03	0.0031
$j$ - $\gamma$	0.52	2	0.41	$\pm$	0.2	0.071
$e$ - $\gamma$	0.76	8	15.3	$\pm$	2.3	0.056
$\nu$ - $\gamma$	0.76	0	1.51	$\pm$	0.53	0.252
$j$ - $j$ - $j$	0.35	7	3.01	$\pm$	0.96	0.055
$e$ - $j$ - $j$	0.49	9	18.4	$\pm$	3.4	0.040
$j$ - $j$ - $\nu$	0.56	5	1.86	$\pm$	0.55	0.054
$e$ - $j$ - $\nu$	0.16	2	0.28	$\pm$	0.07	0.035
$\mu$ - $j$ - $\nu$	0.0008	3	0.07	$\pm$	0.03	0.00007
$j$ - $j$ - $\gamma$	0.31	1	0.10	$\pm$	0.07	0.104
$e$ - $j$ - $\gamma$	0.37	1	5.64	$\pm$	1.50	0.050
$e$ - $j$ - $j$ - $j$	0.75	1	0.14	$\pm$	0.08	0.135
$j$ - $j$ - $j$ - $\nu$	0.22	2	0.28	$\pm$	0.20	0.048

**Table 4.20:** The  $\hat{P}$ -values of the regions derived with the search algorithm using the  $\sum P_T$  distributions for event classes with at least one data event (except the  $j$ - $j$ - $j$ - $j$  and  $e$ - $j$ - $j$ - $j$ - $j$  event classes). In addition, the data events  $N_{\text{obs}}$  and the SM expectation  $N_{\text{exp}}$  with its uncertainty  $\delta N_{\text{exp}}$ , as well as the  $p$ -value are given for each of these regions.





---

# Search for $W$ Bosons in the Hadronic Decay Channel

---

## 5.1 Introduction

The HERA collaborations H1 and ZEUS have reported the observation of events with a high energy isolated charged lepton and missing transverse momentum [4, 35, 97, 98, 99]. The kinematics of these events are compatible with a leptonic  $W$  decay. Considering the electron and muon channels, both experiments find an agreement of the overall observed number of events with the number predicted by the Standard Model (SM). However, the H1 collaboration observes an excess of events with high hadronic transverse momentum  $P_T^X$ , whilst the ZEUS data are in agreement with the SM prediction over the whole  $P_T^X$  range. At  $P_T^X > 25$  GeV, ten events are found compared to a SM expectation of  $2.9 \pm 0.5$  [4]. At  $P_T^X > 40$  GeV, the H1 excess is even more significant with six events found compared to an expectation of  $1.08 \pm 0.22$  [4]. Fig. 5.1 shows the corresponding  $P_T^X$  distribution. In the general search for new phenomena presented in chap. 4, the excess arising from the muon channel alone is found to be even the largest deviation in the H1 data. In addition, the ZEUS collaboration has given results for a search in the tau channel [98] finding an excess of two (one) event(s) at  $P_T^X$  greater than 25 (40) GeV compared to an expectation of  $0.20 \pm 0.05$  ( $0.07 \pm 0.02$ ).

This work presents a search for  $W$  bosons in the dominant hadronic decay mode. In analogy to the leptonic channel, the data are compared to the SM expectation as a function of  $P_T^X$ .  $P_T^X$  can be reconstructed by subtracting the hadronic decay products of the  $W$  from the total hadronic system. The  $W$  signal in the hadronic decay channel is overwhelmed by QCD multi-jet production. Even at high  $P_T^X$ , the QCD cross section is approximately two orders of magnitude higher than the  $W$  cross section. An enhanced  $W$  signal could, however, be detectable. A multivariate likelihood method (sec. 5.3.2) is used in order to maximise the significance of the  $W$  signal.

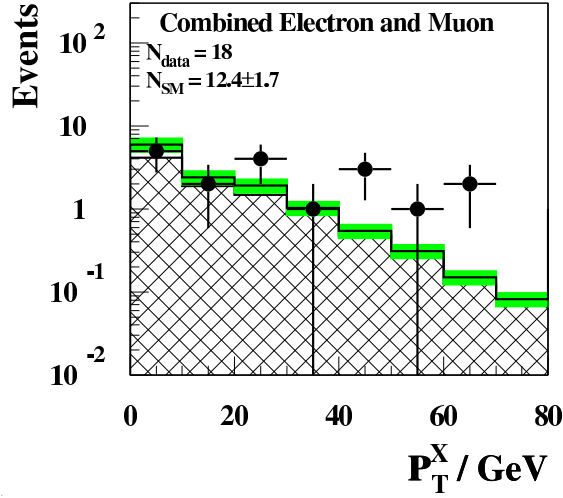


**Figure 5.1:** The  $P_T^X$  distribution in the electron and muon channels combined compared with the SM expectation (open histogram) [4]. The total error on the SM expectation is given by the shaded band. The signal component of the SM expectation is dominated by  $W$  production ( $> 97\%$ )<sup>1</sup> and is given by the hatched histogram.  $N_{\text{data}}$  and  $N_{\text{SM}}$  are the total number of data events and the total SM expectation, respectively.

## 5.2 Standard Model Expectation

The main physics background to this search is the production of jets via hard partonic scattering, which is modelled by PYTHIA and RAPGAP for the photoproduction and DIS regimes, respectively. The predicted cross section is increased by a factor of 1.2 in order to match the observed number of events outside the signal region, which will be defined in the next section. The production of  $W$  and  $Z$  events is simulated with EPVEC. The reader is referred to chap. 2, where the SM processes and their simulation are explained in detail.

## 5.3 Event Selection

The analysis uses data collected between 1995 and 2000 corresponding to an integrated luminosity of  $117.3 \text{ pb}^{-1}$ . In the following, the basic event selection criteria as well as the multivariate likelihood analysis are described.

### 5.3.1 Basic Event Selection

The decay quarks of the  $W$  give rise to two jets with high transverse momentum  $P_T$  each, clustering around the position of the Jacobian peak at half the  $W$  mass. The QCD background events, however, tend to populate the low  $P_T$  region. In direct photon interactions, the  $W$  may be produced at high  $P_T$ , and a third jet balancing the  $P_T$  of the  $W$  may be detected. Considering the resolved contribution, the spectator jet originating from the resolved photon, which proceeds in the direction of the original beam electron, has in general low transverse momentum.

<sup>1</sup> $Z$  production with subsequent decay to neutrinos contributes to less than 3% to the signal prediction.

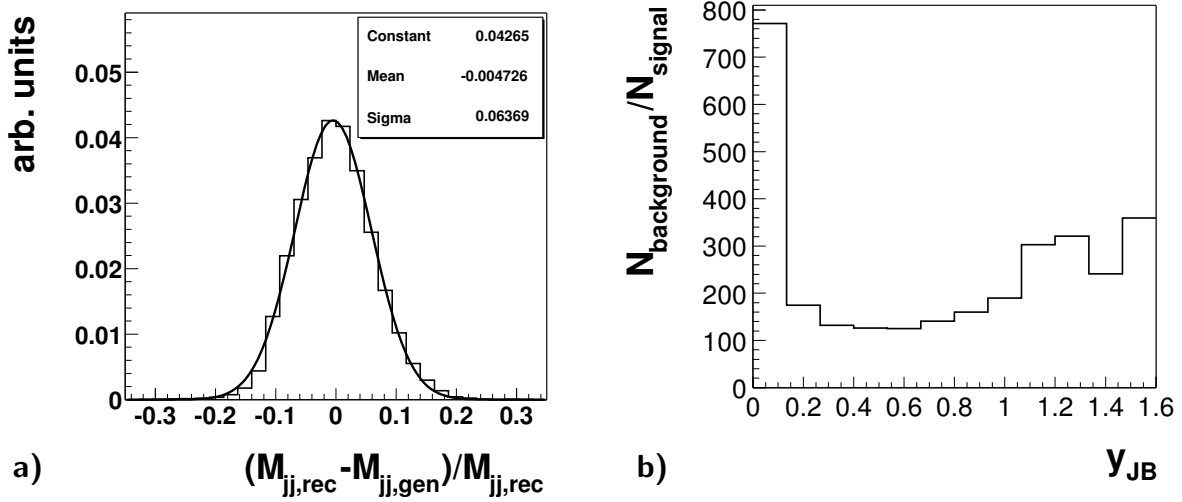


**Figure 5.2:** **a)** Resolution of the  $W$  mass determined with the EPVEC MC. The subscripts *rec* and *gen* denote the reconstructed and generated quantities, respectively. **b)** The background-to-signal ratio  $N_{\text{background}}/N_{\text{signal}}$  as a function of  $y_{\text{JB}}$ .

Consequently, events are selected with at least two hadronic jets, reconstructed using an inclusive  $k_T$  algorithm [80], with a transverse momentum  $P_T$  greater than 25 GeV for the leading jet and greater than 20 GeV for the second highest  $P_T$  jet. The minimum  $P_T$  of any further jet considered in the event is set to 5 GeV. The pseudorapidity  $\eta$  of each jet is restricted to the range  $-0.5 < \eta < 2.5$ . The dijet combination with invariant mass  $M_{jj}$  closest to the  $W$  mass is selected as the  $W$  candidate. The resolution of the reconstructed  $W$  mass is approximately 5 GeV (see fig. 5.2a). The inelasticity  $y_{\text{JB}}$ , reconstructed according to the Jacquet-Blondel method [100], is required to be in the range  $0.1 < y_{\text{JB}} < 1.2$  to account for resolution effects and to reject background. Fig. 5.2b displays the background-to-signal ratio as a function of  $y_{\text{JB}}$  for the final selection (sec. 5.3.2) without the  $y_{\text{JB}}$  cut. At high and low values of  $y_{\text{JB}}$  the background significantly increases. A cut on the missing transverse momentum,  $\cancel{P}_T < 20$  GeV, is applied to reject charged current and non- $ep$  scattering background. Neutral current events where the electron is misidentified as a jet are rejected. Further details on the jet identification and calibration can be found in sec. 4.4.1 and sec. 4.6, respectively.

The kinematic quantities are shown in figs. 5.3 and 5.4 after the above cuts. Fig. 5.3 shows the  $P_T$  and the pseudorapidity of the first and second highest  $P_T$  jet. The  $P_T$  and the pseudorapidity of the third highest  $P_T$  jet are presented in fig. 5.4. The jet kinematics are well described by the SM within the uncertainties (defined in sec. 5.4). At the bottom of fig. 5.4,  $y_{\text{JB}}$  and the missing transverse momentum are shown, which are also well reproduced by the simulation.

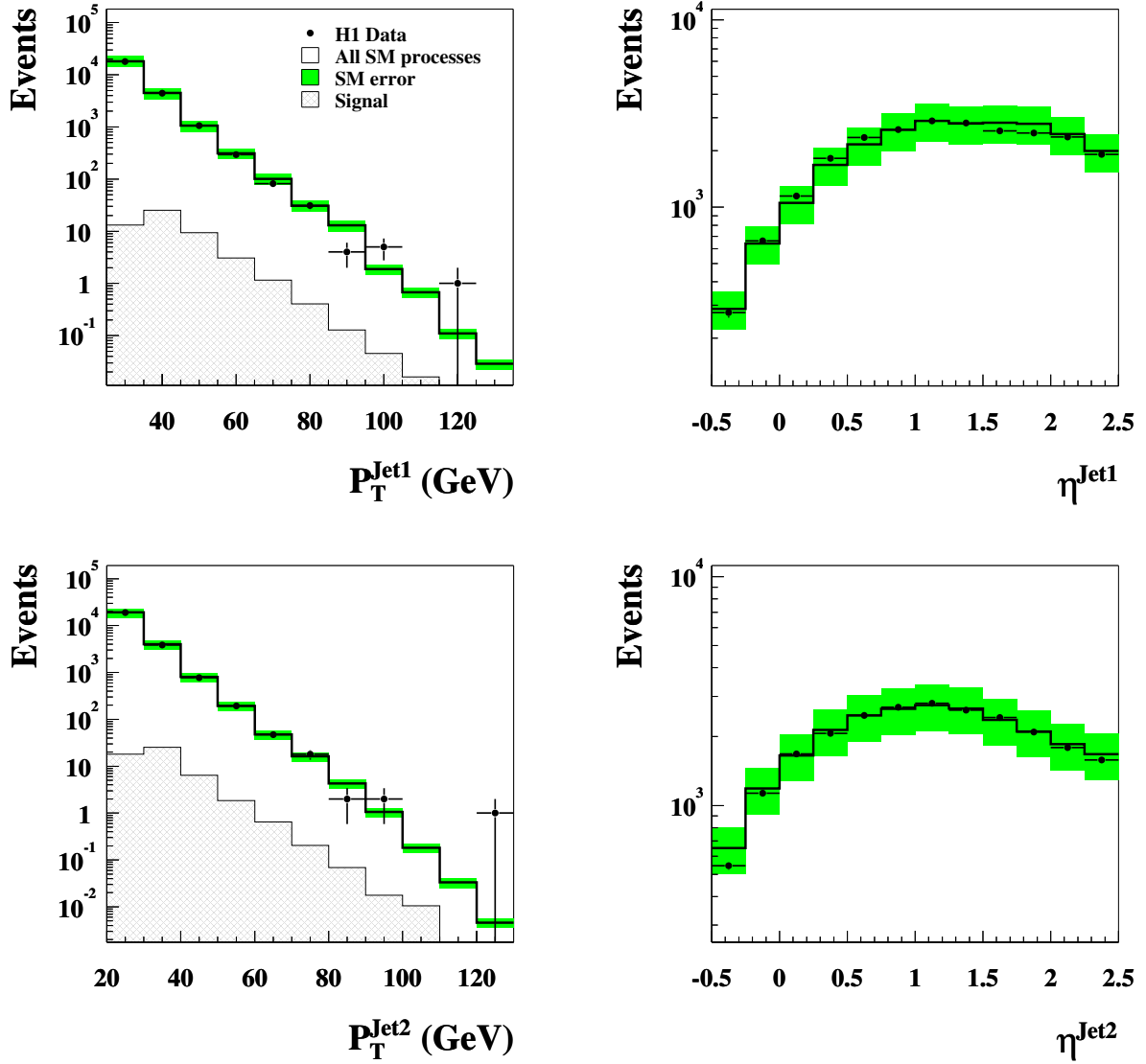


**Figure 5.3:** Distributions of the transverse momentum and pseudorapidity of the first and the second highest  $P_T$  jet before the final selection cuts compared with the SM expectation (open histogram). The total error on the SM expectation is given by the shaded band. The  $W$  production component of the SM expectation is given by the hatched histogram.

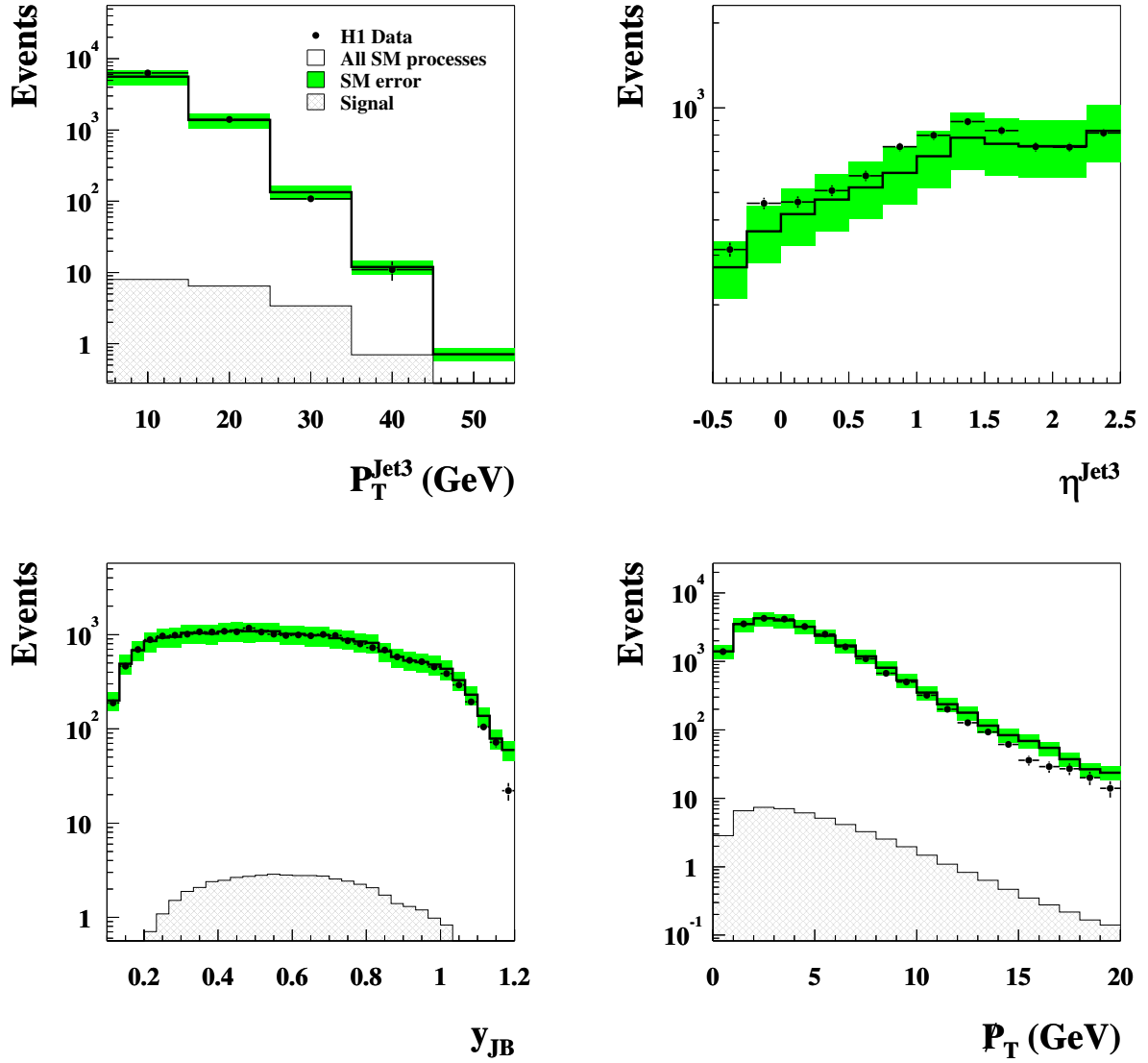


**Figure 5.4:** Distributions of the transverse momentum and pseudorapidity of the third highest  $P_T$  jet, as well as of  $y_{\text{JB}}$  and  $P_T$  before the final selection cuts compared with the SM expectation (open histogram). The total error on the SM expectation is given by the shaded band. The  $W$  production component of the SM expectation is given by the hatched histogram.

### 5.3.2 Multivariate Likelihood Analysis

A likelihood approach is used to further discriminate the  $W$  signal from the QCD background. The selection of the input variables which enter the likelihood analysis as well as the likelihood method itself are described in the following.

#### Selection of Input Variables

Many observables have been studied to attain an optimal discrimination between the  $W$  signal and the QCD background [101]. Some of the most promising observables rely on the jet shape, *e.g.* the radial moment (see sec. 4.4.1) and the subjet multiplicity. Nevertheless their discrimination power is likely to be overestimated as the parton shower in EPVEC is only applied to the final state [65]. Therefore these observables are not considered here.

Two observables have finally been considered for the likelihood analysis. The invariant mass  $M_{jj}$  of the dijet combination closest to the  $W$  mass is naturally one of them. The second one is  $|\cos \hat{\theta}|$ , where  $\hat{\theta}$  is the decay angle of the jets evaluated in the  $W$  rest frame, with the  $W$  flight direction in the laboratory frame taken as the reference axis (see fig. 5.5). Since forward and backward scattering cannot be distinguished due to the similarity of the decay products, only the modulus of the cosine function can be measured. The decay angle  $\hat{\theta}$  is sensitive to the dynamics of the hard subprocess. Most of the QCD matrix elements diverge as  $|\cos \hat{\theta}| \rightarrow 1$  [5]. In the direct photon processes, the exchange of a massless quark dominates and leads to a typical angular distribution  $\sim (1 - |\cos \hat{\theta}|)^{-1}$ . In the resolved processes, mostly a massless vector boson is exchanged yielding an angular distribution  $\sim (1 - |\cos \hat{\theta}|)^{-2}$ . However, in the decay of the

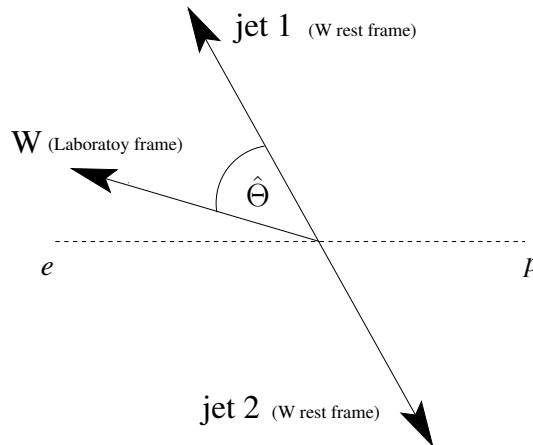


**Figure 5.5:**  $\hat{\theta}$  is the decay angle of the jets evaluated in the  $W$  rest frame, with the  $W$  flight direction in the laboratory frame taken as the reference axis.

massive  $W$  its helicity  $\lambda_W$  leads to the angular distribution [102]

$$\left. \frac{d\Gamma(W \rightarrow f\bar{f}')}{d\cos\hat{\theta}} \right|_{\lambda_W=\begin{pmatrix} \pm 1 \\ 0 \end{pmatrix}} \sim \begin{pmatrix} (1 - \lambda_W \cos\hat{\theta})^2 \\ \sin^2\hat{\theta} \end{pmatrix}.$$

The invariant mass  $M_{jj}$  is related to the decay angle  $\hat{\theta}$  through

$$M_{jj} = \frac{2\hat{P}_T^{\text{jet}}}{\sqrt{1 - |\cos\hat{\theta}|^2}}. \quad (5.1)$$

For a given transverse momentum  $\hat{P}_T^{\text{jet}}$  in the  $W$  centre-of-mass system, events with high values of  $|\cos\hat{\theta}|$  have a high invariant dijet mass.

The relation between  $M_{jj}$  and  $|\cos\hat{\theta}|$  suggests a two dimensional analysis of these observables to obtain an optimal discrimination between the  $W$  signal and QCD background by using all relevant topological information of the underlying subprocess.

### Likelihood Analysis

In order to optimise the phase space cuts for  $W$  production a two-dimensional likelihood analysis is performed in the  $M_{jj} - |\cos\hat{\theta}|$  plane. Two-dimensional probability densities  $P(M_{jj}, |\cos\hat{\theta}|)$  of simulated  $W$  and QCD events are used to evaluate the likelihood  $\mathcal{L}$  of an event:

$$\mathcal{L} = \frac{P_W(M_{jj}, |\cos\hat{\theta}|)}{P_W(M_{jj}, |\cos\hat{\theta}|) + P_{\text{QCD}}(M_{jj}, |\cos\hat{\theta}|)}. \quad (5.2)$$

As the MC events are, despite the large MC samples, sparsely distributed in some regions of the two-dimensional space, the so-called multivariate kernel estimation method [103, 104, 105] is applied in order to obtain smooth probability density functions. Here, each sample point in the two-dimensional space, which is normally directly filled into a binned histogram, is smeared according to a two-dimensional Gaussian taking the linear correlation of the data properly into account. Therefore 1000 sample points are pulled randomly from this Gaussian distribution and centred on each original sample point with a statistical weight of 1/1000. The widths of the distribution are controlled by the so-called smoothing parameters [103]. Adding up these Gaussian bumps centred around the original values ends up in a smooth distribution. Fig. 5.6 shows the resulting probability density functions for background and signal. Because of the  $P_T$  requirements, events with large values of  $|\cos\hat{\theta}|$  are suppressed. Considering the background, the shape of  $|\cos\hat{\theta}|$  drastically changes as a function of the  $M_{jj}$  values. With increasing values of  $M_{jj}$ , the restriction of the phase space is more and more reduced due to the correlation with the  $P_T$  requirements, and the shape of the  $|\cos\hat{\theta}|$  distribution changes towards that expected from the QCD matrix elements. On the other hand, the phase space of the  $W$  signal is hardly affected by the  $M_{jj}$  requirements.

Once the probability density functions have been estimated, the likelihood distribution follows trivially from the above formula. To determine the optimal cut value of the likelihood in the sense of efficiency and signal-to-background ratio, the upper limit  $\sigma^{95\%CL}$  is calculated at 95% confidence level (CL) for each possible likelihood cut value considering only the signal and background models. The minimum value of  $\sigma^{95\%CL}$  determines the likelihood cut value.

Fig. 5.7a displays  $\sigma^{95\%CL}$  as a function of the likelihood cut value, the minimum value of  $\sigma^{95\%CL}$  being indicated. This procedure guarantees to obtain the region with the optimal sensitivity for  $W$  production without any bias. The selected region is shown as small boxes in fig. 5.7b. It may be astonishing that the high mass region ( $100 \text{ GeV} \lesssim M_{jj} \lesssim 200 \text{ GeV}$ ) is also favoured. But, even if the efficiency for  $W$  production is low in this phase space, the signal-to-background ratio increases as a function of the mass. At very high masses ( $M_{jj} \gtrsim 200 \text{ GeV}$ ), the SM expectation becomes negligible.

Finally, the region selected by the likelihood method can be approximated by the open rectangular visualised in fig. 5.7b and defined through the cuts  $M_{jj} > 70 \text{ GeV}$  and  $|\cos \hat{\theta}| < 0.6$ . Very similar results are obtained with both selections, and the likelihood method is therefore only used as a motivation to chose the final selection cut scenario, *i.e.*  $M_{jj} > 70 \text{ GeV}$  and  $|\cos \hat{\theta}| < 0.6$ .

The kinematical quantities of the final data sample are discussed in the following. Fig. 5.8 displays the distributions of the transverse momentum and pseudorapidity of the highest and the second highest  $P_T$  jet. The corresponding distributions for the third highest  $P_T$  jet are shown at the top of fig. 5.9. The jet kinematics are again well described by the SM within the uncertainties. Compared to figs. 5.3 and 5.4, the signal-to-background ratio has been improved by a factor  $\approx 4$ . A similar improvement is reached at  $P_T^X > 40 \text{ GeV}$ . The distribution of  $y_{JB}$  shown at the bottom of fig. 5.9 is also in agreement with the SM expectation. The one-dimensional distribution of  $|\cos \hat{\theta}|$  is presented at the bottom of fig. 5.9. The cut on  $|\cos \hat{\theta}|$  has here been omitted. As already previously discussed, the SM expectation, which is dominated by QCD background events, has a different shape compared to the  $W$  signal.

$P_T^{\text{Jet1, Jet2}} > 25, 20 \text{ GeV}$
$P_T > 5 \text{ GeV}$ for any further considered jet
$-0.5 < \eta < 2.5$
$M_{jj} > 70 \text{ GeV}$
$ \cos \hat{\theta}  < 0.6$
jet quality criteria as defined in sec. 4.4.1
$0.1 < y_{JB} < 1.2$
$\cancel{P}_T < 20 \text{ GeV}$

**Table 5.1:** The final  $W$  selection criteria.



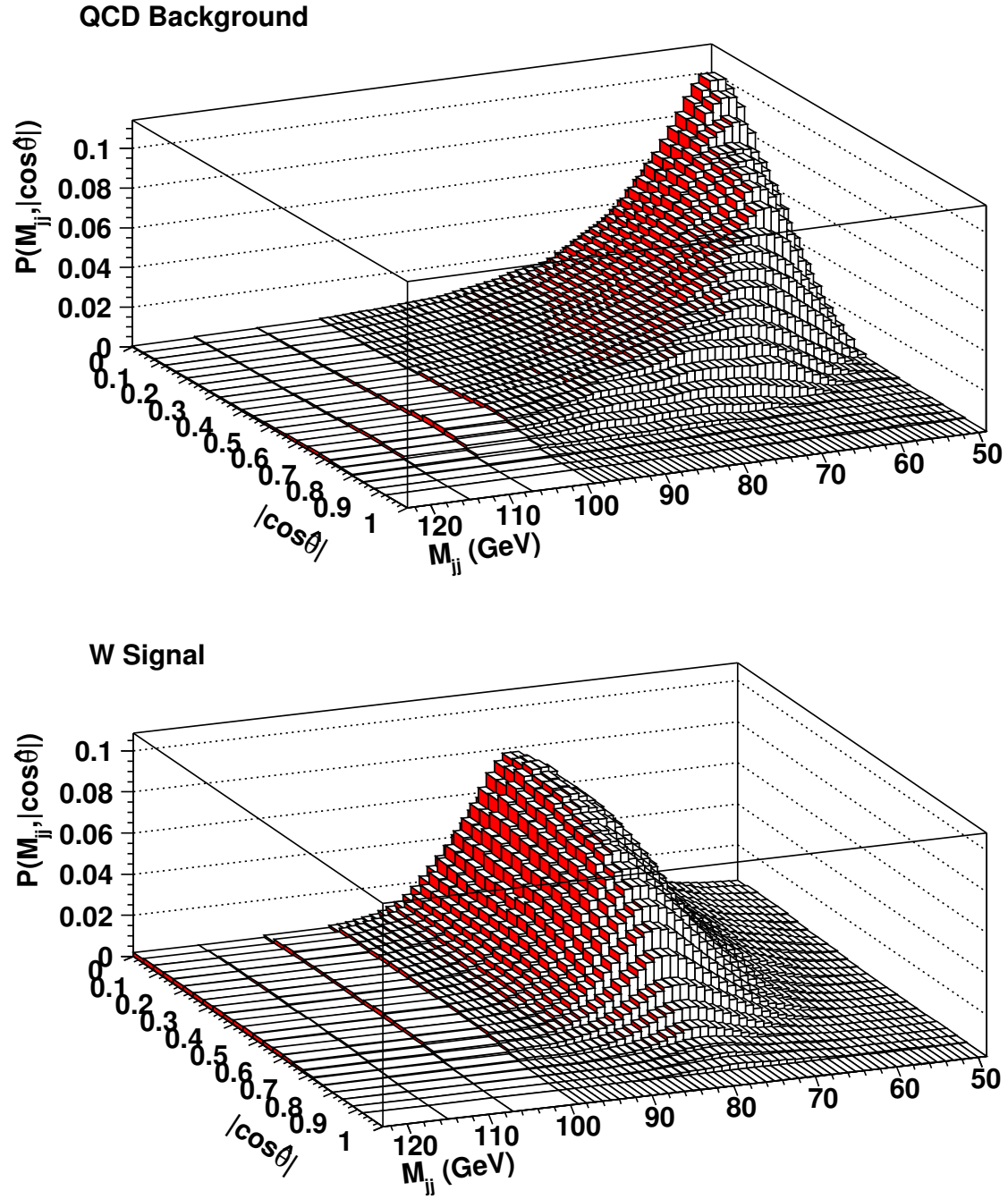


**Figure 5.6:** Probability density functions of QCD background and  $W$  signal.

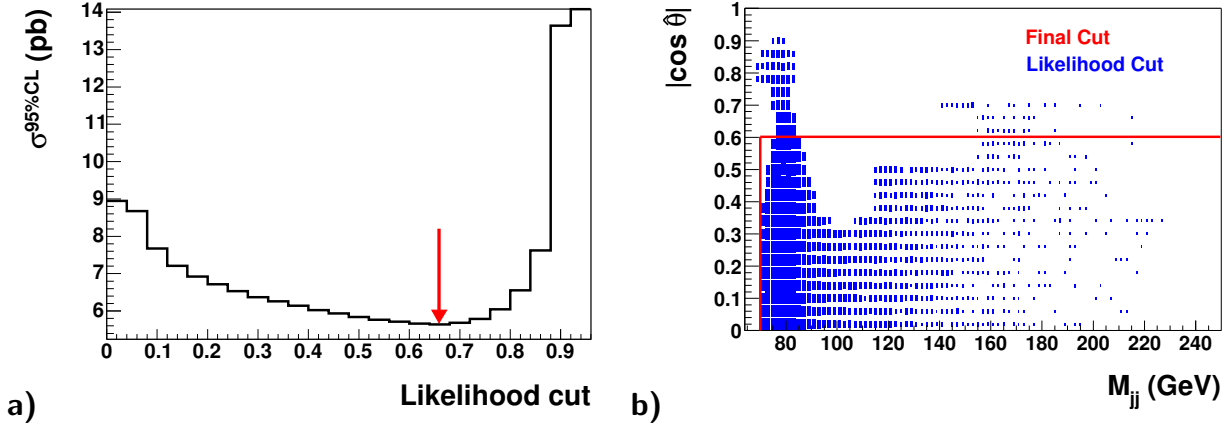


**Figure 5.7:** **a)** The upper limit  $\sigma^{95\%CL}$  as a function of the likelihood cut value. **b)** The signal region in the  $M_{jj} - |\cos \hat{\theta}|$  plane determined with the likelihood method. It is shown as small boxes and motivates the choice of the final cut region visualised by the open rectangle.

## 5.4 Systematic Uncertainties

The following sources contribute to the systematic uncertainty on the QCD expectation:

- The difference in shape between data and SM in the non-signal region leads to an uncertainty of 15% as explained in app. D.
- The uncertainty of the parton density functions at high transverse momentum results in an uncertainty of 10%.
- A 4% uncertainty in the jet energy scale results in an uncorrelated uncertainty of 10%.<sup>2</sup>
- Uncertainties arising from the high  $y_{JB}$  region, electron-jet separation and background add up to an uncertainty of 10%.

All errors are added quadratically so that the overall systematic uncertainty on the QCD expectation is 23%.

The  $W$  signal is modelled by EPVEC and reweighted to a NLO calculation as explained in sec. 2.9. The NLO calculation reduces the theory error on the  $W$  prediction at both high and low  $W$  transverse momentum to 15% (from 30% at leading order). The previously described uncertainty of 15%, which accounts for the difference in shape in the non-signal region, as well as the 10% uncertainty arising from the uncertainty of the parton density functions are omitted. The overall systematic uncertainties on the SM  $W$  expectation result thus after quadratic summation in a total uncertainty of 21%.

<sup>2</sup>The correlated uncertainty is taken into account by the normalisation factor of 1.2 (see sec. 5.2); although the jet energy scale has been estimated to be 2% (see sec. 4.6), the larger value of 4% is used to be consistent with the H1 search in the muon and electron channels.

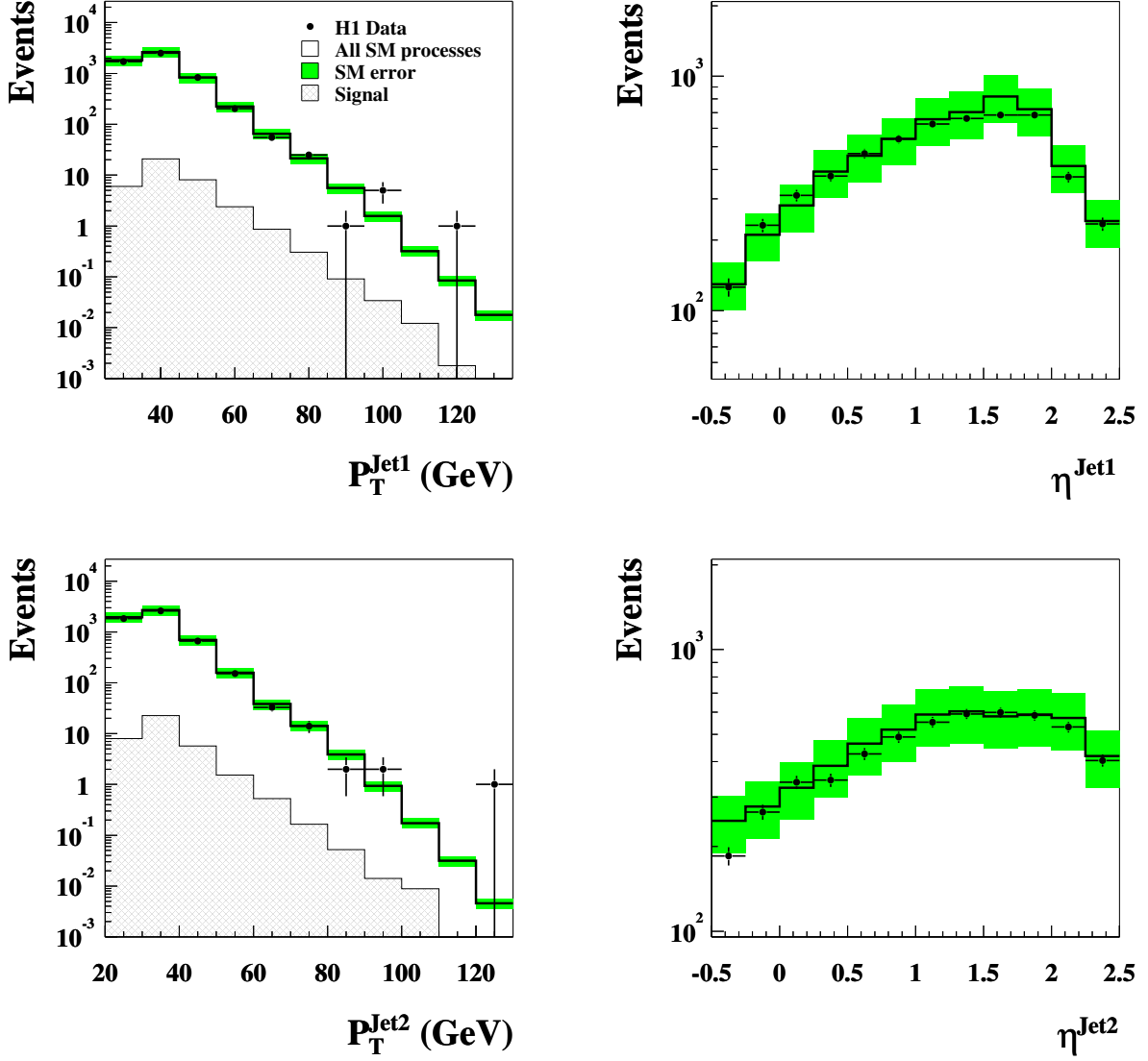


**Figure 5.8:** Distributions of the transverse momentum and pseudorapidity of the first and second highest  $P_T$  jet for the final data sample compared with the SM expectation (open histogram). The total error on the SM expectation is given by the shaded band. The  $W$  production component of the SM expectation is given by the hatched histogram. The highest  $P_T^{\text{Jet1}}$  and  $P_T^{\text{Jet2}}$  value belong to one single event, which builds the largest deviation in the  $j$ - $j$  event class in the general search for new phenomena (see chap. 4). The corresponding event display is presented in app. B.

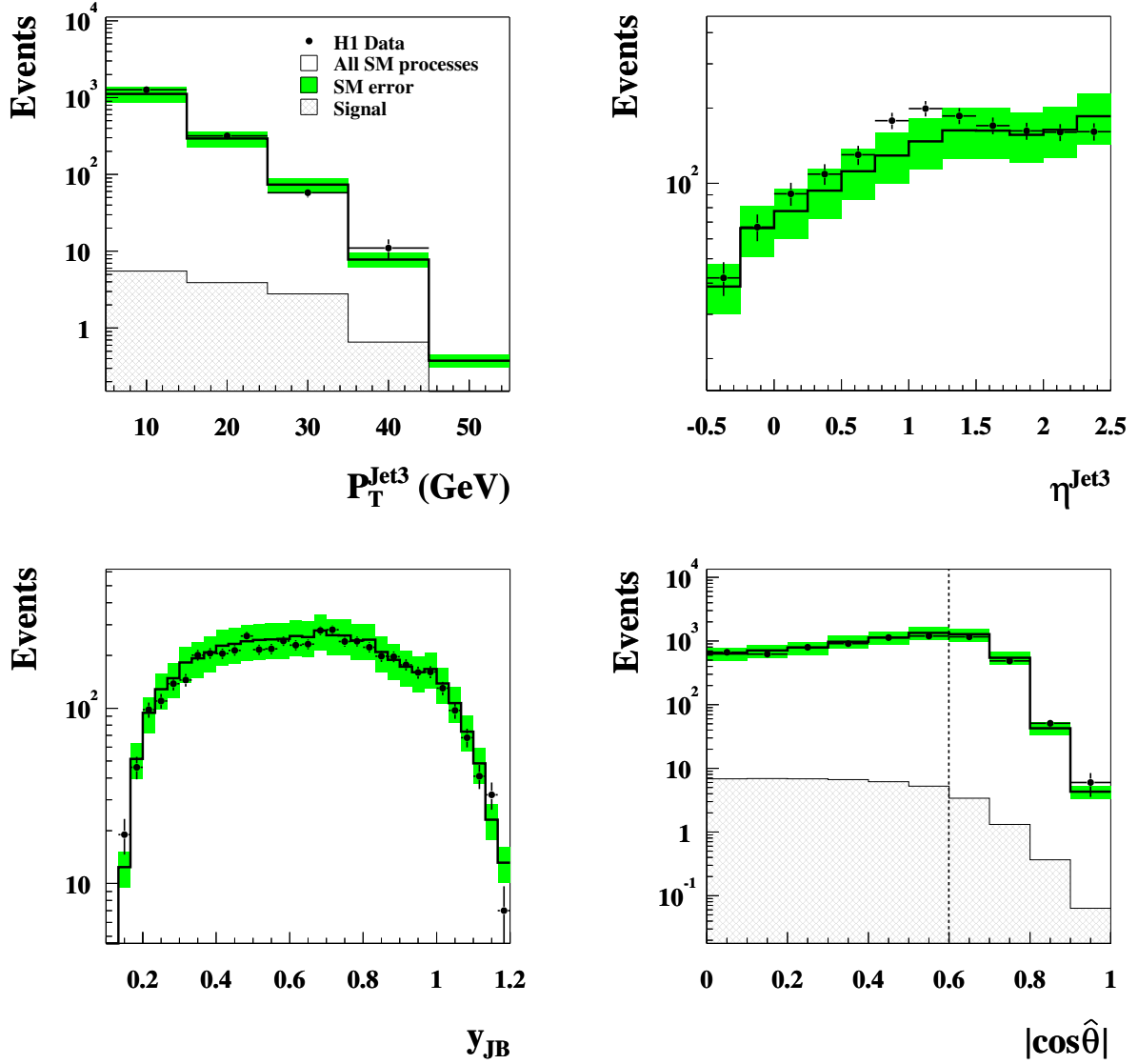


**Figure 5.9:** Distributions of the transverse momentum and pseudorapidity of the third highest  $P_T$  jet and of  $y_{\text{JB}}$  (with all cuts), as well as the  $|\cos \hat{\theta}|$  distribution (without the  $|\cos \hat{\theta}|$  cut, indicated by the dashed line) of the selected data compared with the SM expectation (open histogram). The total error on the SM expectation is given by the shaded band. The  $W$  production component of the SM expectation is given by the hatched histogram.

## 5.5 Results

Applying the selection criteria described above, the efficiencies as a function of  $P_T^X$  are shown in tab. 5.2. The efficiency loss at  $P_T^X > 12$  GeV is mainly due to the unavoidable merging of one of the  $W$  decay quarks with the  $W$  recoil quark into one jet by the jet algorithm if their distance  $R_{q_{\text{recoil}}}^{qW}$  in the  $\eta - \phi$  plane is less than the separation parameter used in the jet algorithm. In this analysis, the separation parameter is set to unity. Fig. 5.10a shows the reconstructed versus the generated  $P_T^X$  for the  $W$  model. Comparing the distance  $R_{q_{\text{recoil}}}^{qW}$  for the badly and well correlated events in fig. 5.10b confirms the merging hypothesis.

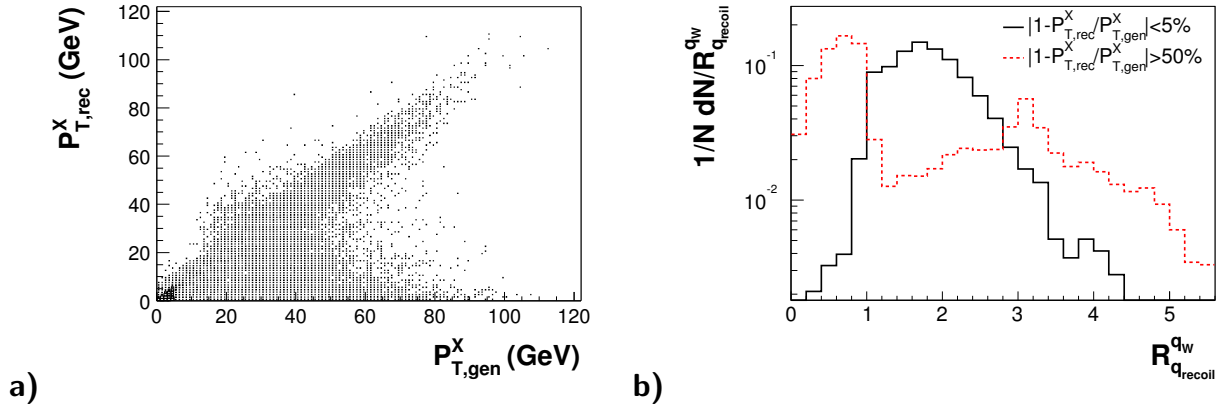


**Figure 5.10:** a) Reconstructed versus generated  $P_T^X$ . b) The minimum distance  $R_{q_{\text{recoil}}}^{qW}$  of the  $W$  recoil quark to the quarks originating from  $W$  decay. It is mostly below the separation parameter of the jet algorithm for events with wrongly reconstructed  $P_T^X$  (dashed line) compared to those with well reconstructed  $P_T^X$  (full line). Note that the distributions are normalised to unity.

The  $M_{jj}$  distribution (without the  $M_{jj}$  cut) and the  $P_T^X$  distribution (with all cuts) of the selected data are compared to the SM expectation in fig. 5.11. The data show an overall agreement with the SM expectation up to the highest  $P_T^X$  values. At  $P_T^X > 25$  GeV, 126 events are observed compared to a SM expectation of  $161.9 \pm 36.0$  with  $5.3 \pm 1.1$  expected from  $W$  production. The SM expectation is dominated by the QCD multi-jet production. The contribution from  $Z$  production is negligible. For  $P_T^X > 40$  GeV, 27 events are observed in the data comparable with the expectation of  $30.9 \pm 6.7$ . In this phase space, the  $W$  contribution amounts to  $1.9 \pm 0.4$  events with a selection efficiency of 29%. Tab. 5.3 presents the data and the SM expectation for different cuts on  $P_T^X$ .

The results are in the following compared to the results of the leptonic search [4], where at  $P_T^X > 40$  GeV, six events are found compared to an expectation of  $1.08 \pm 0.22$ , the  $W$  signal contributing  $0.96 \pm 0.22$  events. If one assumes that this excess is due to  $W$  production, the  $W$  cross section has to be enhanced by a factor  $6.2_{-2.3}^{+3.0}$  (app. E). This would lead in the hadronic channel to  $11.8_{-4.4}^{+5.7}$  events expected from  $W$  production. The compatibility of the measurements in the leptonic and hadronic channels is then 1.8 standard deviations, as explained in app. E.

Cut on $P_T^X$	Efficiency
$P_T^X > 0$ GeV	0.43
$P_T^X > 12$ GeV	0.30
$P_T^X > 25$ GeV	0.30
$P_T^X > 40$ GeV	0.29

**Table 5.2:** Efficiencies of the final selection for  $W$  bosons in the hadronic decay channel as a function of the cut on  $P_T^X$  calculated with the EPVEC generator.

	H1 data	SM expectation	$W$ signal	Other SM processes
$P_T^X > 0$ GeV	5308	$5568 \pm 1272$	$38.6 \pm 8.1$	$5529 \pm 1272$
$P_T^X > 12$ GeV	728	$735 \pm 166$	$11.3 \pm 2.4$	$724 \pm 166$
$P_T^X > 25$ GeV	126	$161.9 \pm 36.0$	$5.3 \pm 1.1$	$156.6 \pm 36.0$
$P_T^X > 40$ GeV	27	$30.9 \pm 6.7$	$1.9 \pm 0.4$	$29.0 \pm 6.7$

**Table 5.3:** Observed and predicted event rates in the hadronic channel for the final selection as a function of the cut on  $P_T^X$ . For each  $P_T^X$  cut, the observed event rates are compared to the total SM expectation; the  $W$  signal component, as well as the SM expectation without the  $W$  signal (“other SM processes”), are also given.

Although there is increasing sensitivity to  $W$  production with increasing  $P_T^X$ , there is thus no evidence for anomalous  $W$  production with the present statistics. Since the backgrounds remain large even at high  $P_T^X$ , it is at present not possible to conclude from the hadronic channel whether the observed excess of events with an isolated electron or muon with missing transverse momentum at high  $P_T^X$  is due to  $W$  production.

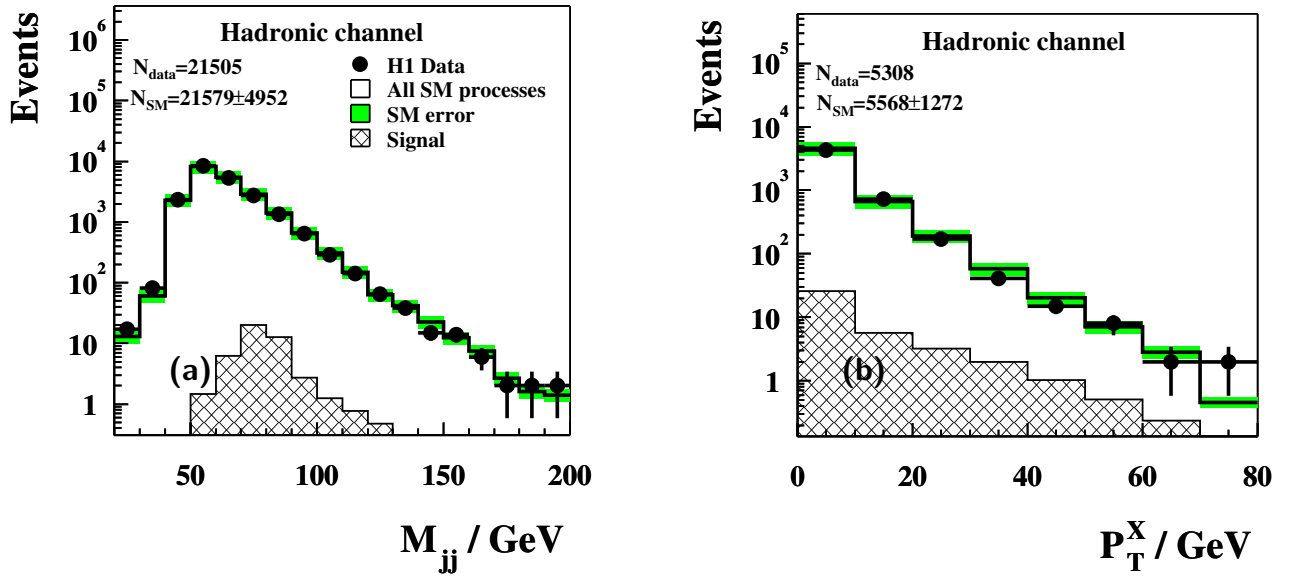


**Figure 5.11:** The dijet mass distribution  $M_{jj}$  (a) and the  $P_T^X$  distribution (b) compared with the SM expectation (open histogram) in the  $W$  hadronic decay channel search. The total error on the SM expectation is given by the shaded band. The  $W$  production component of the SM expectation is given by the hatched histogram.  $N_{\text{data}}$  is the total number of data events observed for each sample;  $N_{\text{SM}}$  is the total SM expectation.

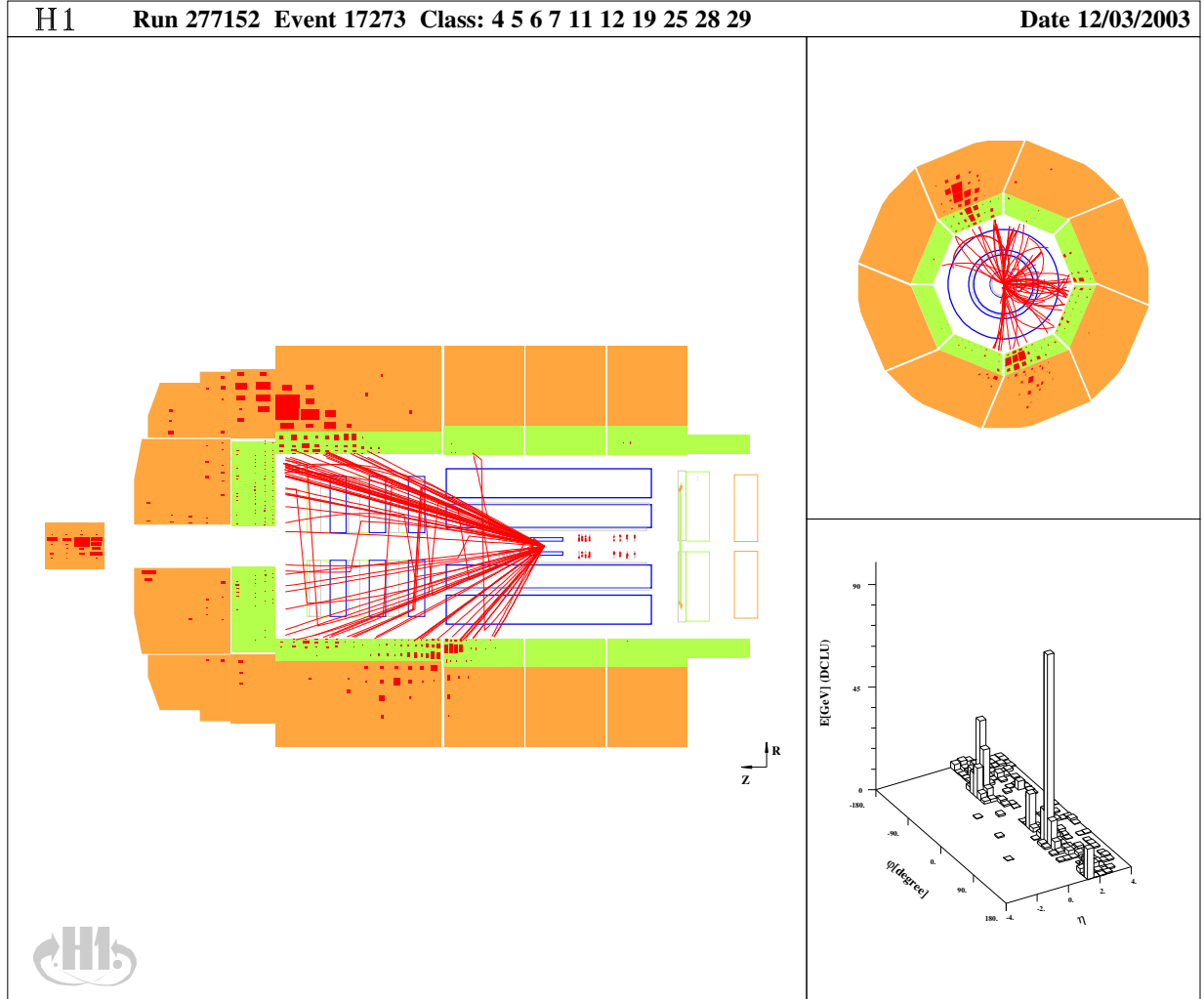


**Figure 5.12:** Event display of one out of the 27 selected events with  $P_T^X > 40$  GeV. It is a 3-jet event with an invariant mass of 76 GeV for the dijet  $W$  candidate.



---

# Summary and Outlook

---

A general search for new phenomena and a dedicated search for  $W$  bosons in the hadronic decay channel have been performed in  $ep$  collisions at HERA.

## General Search for New Phenomena

The data collected with the H1 experiment during the years 1994-2000 (HERA I) has been searched for deviations from the Standard Model prediction at high transverse momentum. All possible event topologies have been investigated in a coherent and model-independent way. Many event classes are analysed herein for the first time at HERA. A good agreement between data and Standard Model expectation has been found in most event classes. The invariant mass and sum of transverse momenta distributions of the event classes have been systematically searched for deviations with a novel algorithm. The most significant deviation is found in the  $\mu$ - $j$ - $\nu$  event class, a topology where deviations have also been previously observed. About 2% of hypothetical Monte Carlo experiments would produce deviations more significant than the one observed in the corresponding sum of transverse momenta distribution.

## Search for $W$ Bosons in the Hadronic Decay Channel

A dedicated search for hadronic  $W$  decays has been performed on an  $ep$  data sample collected with the H1 detector in the years 1995 to 2000. The analysis has been tuned to maximise the acceptance for  $W$  events and to reduce other Standard Model contributions. The search in the hadronic decay channel complements the corresponding H1 search in the leptonic decay channel. In the latter search, there is a significant excess of events with transverse momentum of the  $W$  recoil system ( $P_T^X$ ) greater than 40 GeV, with six events found compared to  $1.08 \pm 0.22$  expected. The excess in the muon channel alone has moreover been quantified in the general search for new phenomena to be the largest deviation in the H1 data. In analogy to the leptonic channel, the data are compared to the Standard Model expectation as a function of  $P_T^X$ . An agreement with

the Standard Model expectation is found up to the highest  $P_T^X$  values. The high background in this channel, however, does not allow one to conclude whether the excess of isolated leptons with missing  $P_T$  at high  $P_T^X$  is due to  $W$  production. The compatibility between the measurement in the leptonic and hadronic channels has been evaluated to be 1.8 standard deviations.

## **Outlook**

The luminosity upgrade of the HERA machine is expected to lead to a much higher integrated luminosity for the so-called HERA II data set by 2006. The concept of the general search is ideally suited to be implemented as a global search tool for new physics in HERA II data and can, moreover, be incorporated at future collider experiments. Finally, the HERA II increase in integrated luminosity will help to clarify whether the deviations found and discussed in this work are statistical fluctuations or signs of new physics.

# Appendix A: Track Selection

The track selection is based on the H1 standard track selection by L. West [106]. Most parameters are set to the default values. Following ref. [4], the standard requirement that the relative error of the track momentum measurement is below 100% for combined tracks<sup>1</sup> has not been made, as high transverse momentum tracks tend to be stiff and have large errors. Tab. A.1 displays the used settings.

Combined			Central			Forward		
$P_T$	>	0.12 GeV	$P_T$	>	0.12 GeV	$P$	>	0.5 GeV
$\theta_{\min}$	>	0.0°	$\theta_{\min}$	>	20.0°	$\theta_{\min}$	>	6.0°
$\theta_{\max}$	<	40.0°	$\theta_{\max}$	<	160.0°	$\theta_{\max}$	<	25.0°
$R_{\text{start}}$	<	50 cm	$R_{\text{start}}$	<	50 cm	$R_0$	<	10 cm
$DCA$	<	5.0 cm	$DCA$	<	5.0 cm	$N_{\text{seg}}$	>	2
			RPTPTH	=	1.0	$N_{\text{plan. seg}}$	>	1
$\chi^2_{\text{FT-CT-link}}$	<	50.0	Length	>	10.0 cm	$\chi^2_{\text{trackfit}}$	<	10.0
$\chi^2_{\text{vertexfit}}$	<	50.0				$\chi^2_{\text{vertexfit}}$	<	25.0

**Table A.1:** Track selection.

## Track Selection

- $P_T$ ,  $P$ : transverse track momentum and track momentum, respectively
- $\theta_{\min, \max}$ : minimum and maximum track polar angles, respectively
- $R_{\text{start}}$ : radial distance of the first hit to the  $z$ -axis
- $R_0$ : radial distance of a non-vertex fitted track to the nominal vertex

<sup>1</sup>A combined track results from the linking of a forward and a central track.

- *DCA*: distance of closest approach to the primary event vertex
- $\chi^2_{\text{FT-CT-link}}$ :  $\chi^2$  of the fit linking the forward and the central track segment
- $\chi^2_{\text{vertexfit}}$ :  $\chi^2$  of the fit to the primary event vertex
- $\chi^2_{\text{trackfit}}$ :  $\chi^2$  of the fit to the hits in the tracking detectors
- *Length*: difference of the radii at the start and at the end of a track
- $N_{\text{plan. seg}}$ : number of hit planar segments
- $N_{\text{seg}}$ : number of hit planar and radial segments
- *RTPH*: variable used to remove double tracks

---

## Appendix B: Particular Events

---

This section presents the classification of events from two previously published analyses [96, 4] which reported an excess of events with respect to the SM expectation. Furthermore, several event displays of outstanding events with high  $M_{\text{all}}$  and  $\sum P_T$  values which are selected in this analysis are shown.

### Multi-Electron Events

In ref. [96], six multi-electron events with an invariant mass greater than 100 GeV are selected in the HERA I data sample. Three of them are di-electron events, which are also found back in the  $e-e$  event class in this analysis. The other three events are tri-electron events. They are rejected because the two lowest  $P_T$  electrons (e2, e3) fail the  $P_T$  and/or the  $\theta$  requirement.

Run	Event	Event Class	Rejection Reason(s)
83507	16817	$e-e$	$P_T^{e2,3} < 20 \text{ GeV}, \theta^{e2} < 10^\circ$ $P_T^{e2,3} < 20 \text{ GeV}$
89256	224212	$e-e$	
168058	42123		
192864	123614		
254959	17892	$e-e$	$P_T^{e2,3} < 20 \text{ GeV}$
267312	203075		

**Table B.1:** *The multi-electron events and their classification.*

## Isolated Lepton Events

In ref. [4], 19 events with a high energy isolated electron or muon and missing transverse momentum (“isolated lepton events”) are selected in the HERA I data sample.

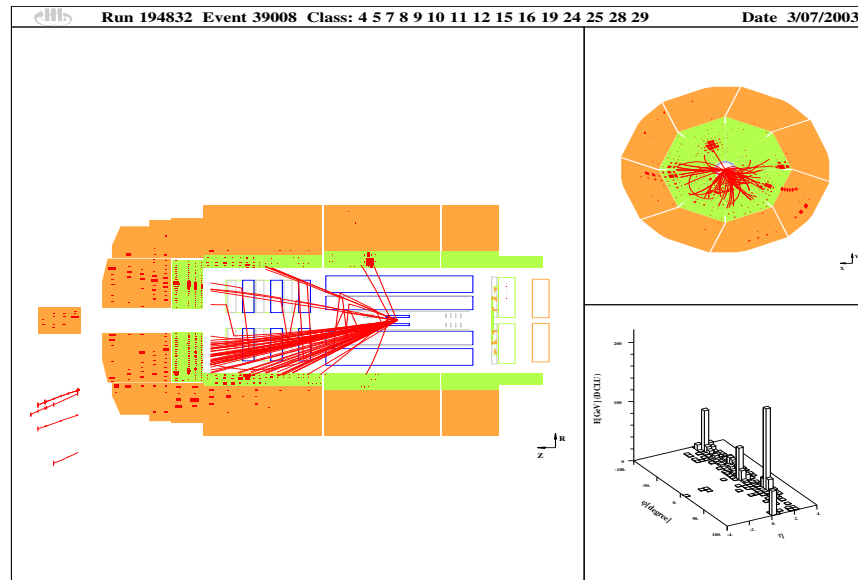
Run	Event	Event Class	Rejection Reason(s)
90264	313	$e-\nu$	$P_T^{\text{Jet}} < 20 \text{ GeV}$
186729	702	$\mu-j-\nu$	
188108	5066		$\theta^{\text{Jet}} < 10^\circ$
192227	6208	$\mu-j-\nu$	
195308	16793	$\mu-j-\nu$	
196406	38438		$P_T^{\text{Jet},e} < 20 \text{ GeV}$
236176	3849		$P_T^e < 20 \text{ GeV}$ , QBGFMAR background finder <sup>1</sup>
248207	32134	$e-j-\nu$	
251415	43944		$P_T^{\text{Jet}}, \cancel{P}_T < 20 \text{ GeV}$
252020	30485	$e-j-\nu$	
253700	90241		$P_T^{\text{Jet}} < 20 \text{ GeV}$
266336	4126	$j-\nu$	$P_T^\mu < 20 \text{ GeV}$
268338	70014		$ z_{\text{vertex}}  > 35 \text{ cm}$
269672	66918		$E_{R=0.75}/E^e > 2.5\%$
270132	73115	$\mu-j-\nu$	
274357	6157	$e-\nu$	$P_T^{\text{Jet}} < 20 \text{ GeV}$
275991	29613		$1/P_T^{e_{tk}} - 1/P_T^e > 0.02 \text{ GeV}^{-1}$
276220	76295		$1/P_T^{e_{tk}} - 1/P_T^e > 0.02 \text{ GeV}^{-1}$
277699	91265	$e-\nu$	$P_T^{\text{Jet}} < 20 \text{ GeV}$

**Table B.2:** The “isolated lepton events” and their classification.

<sup>1</sup>Due to  $P_T^e < 20 \text{ GeV}$ , the event is attributed to the  $j-\nu$  event class, where it is rejected by the QBGFMAR background finders.

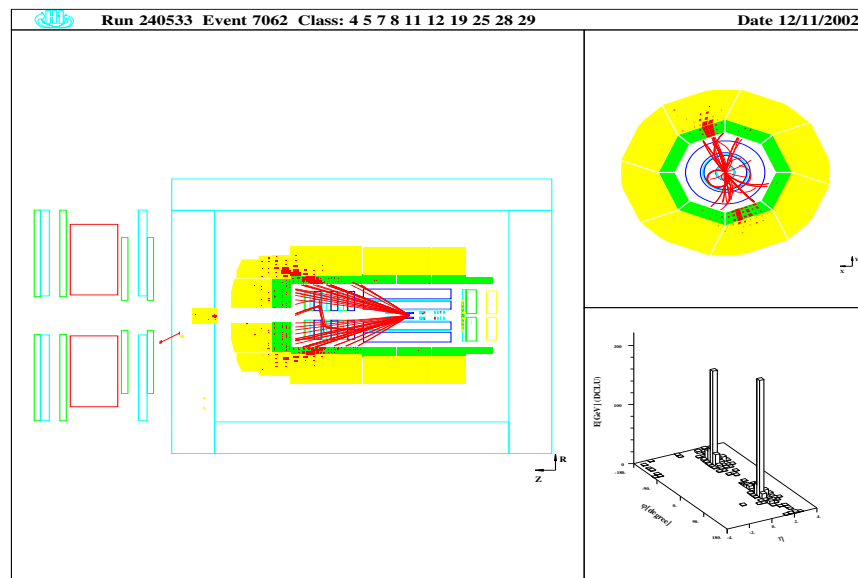
## Event Displays

### $e$ - $j$ - $j$ - $j$ - $j$ Event Class

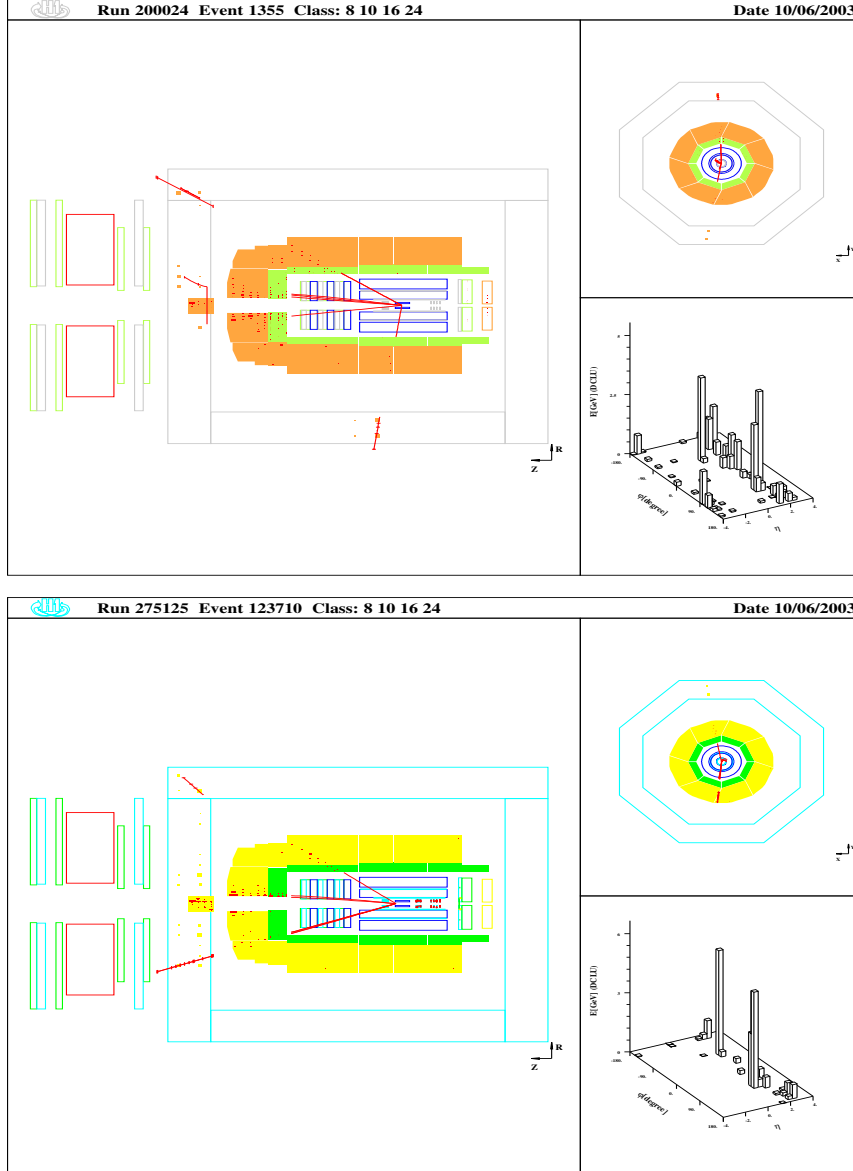


Event display of the one and only event attributed to the  $e$ - $j$ - $j$ - $j$ - $j$  event class. The  $e$ - $j$ - $j$ - $j$ - $j$  final state has an invariant mass of 263 GeV and  $\sum P_T$  of 209 GeV.

### $j$ - $j$ Event Class



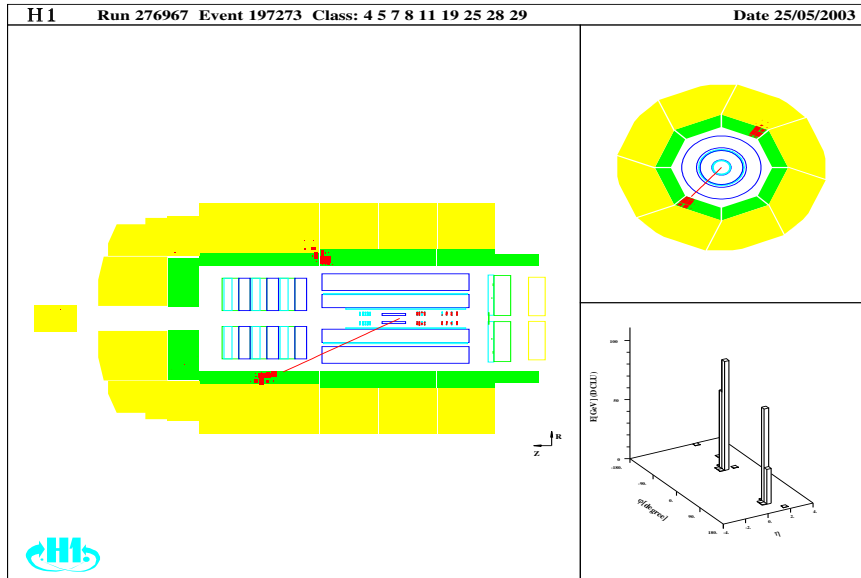
Event display of the event with the highest  $M_{\text{all}}$  and  $\sum P_T$  in the  $j$ - $j$  event class. The  $j$ - $j$  final state has an invariant mass of 244 GeV and  $\sum P_T$  of 244 GeV.

$\mu\text{-}\mu$  Event Class

Event displays of the two events with the highest  $M_{\text{all}}$  and  $\sum P_T$  values in the  $\mu\text{-}\mu$  event class. The event shown at the top has the kinematic values  $M_{\text{all}} = 102$  GeV and  $\sum P_T = 92$  GeV, and the one at the bottom  $M_{\text{all}} = 96$  GeV and  $\sum P_T = 110$  GeV.



## $e\text{-}\gamma$ Event Class



Event display of the event with the highest  $M_{\text{all}}$  and  $\sum P_T$  in the  $e\text{-}\gamma$  event class. The  $e\text{-}\gamma$  final state has an invariant mass of 168 GeV and  $\sum P_T$  of 164 GeV.



---

## Appendix C: Comparison of Different Jet Quality Criteria

---

The rejection power of different sets of cuts against fake jets are compared in the following. Listed is the percentage of rejected events for events with at least one fake jet (Fake Rejection) and for events with only genuine jets (Non-Fake Rejection). The purity and efficiency of all the studied sets of cuts are compared in fig. C.1.

### Set 1

At the top of fig. 4.2, the inelasticity  $y_{JB}$ , reconstructed according to the Jacquet-Blondel method [100], is shown before and after the cuts. For events with fake jets,  $y_{JB}$  is approximately 1 as the electron is here included in the hadronic final state. This fact has been used in the following jet quality criteria.

$M^{\text{Jet}}/P_T^{\text{Jet}} > 0.1$
$M^{\text{Jet}}/P_T^{\text{Jet}} > 0.12$ if $EM_{\text{frac}}^{\text{Jet}} > 0.9$ or $y_{JB} > 0.9$
$M^{\text{Jet}}/P_T^{\text{Jet}} > 0.14$ if $EM_{\text{frac}}^{\text{Jet}} > 0.9$ and $y_{JB} > 0.9$
$\langle R \rangle > 0.02$
$\langle R \rangle > 0.04$ if $EM_{\text{frac}}^{\text{Jet}} > 0.9$ or $y_{JB} > 0.9$
$\langle R \rangle > 0.14$ if $EM_{\text{frac}}^{\text{Jet}} > 0.9$ and $y_{JB} > 0.9$

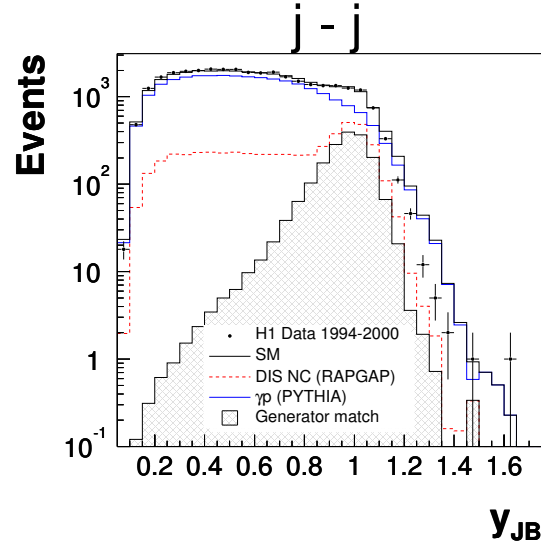


**Figure C.1:** The distribution of  $y_{JB}$  before the application of any jet quality criteria. The HERA I data sample is compared to the SM prediction for the  $j$ - $j$  event class; the contributions from DIS NC and photoproduction processes are also shown. The shaded contribution labelled “Generator match” represents the events where the generated electron lies within a cone of  $R = 1$  inside the reconstructed jet. The fake jet contribution dominates at  $y_{JB} \approx 1$ .

Event Class	Fake Rejection (%)	Non-Fake Rejection (%)
$j$ - $j$	78.9	1.2
$e$ - $j$	30.1	0.7
$\mu$ - $j$	90.8	3.8
$j$ - $\nu$	89.5	1.4
$j$ - $\gamma$	61.7	0.8
$j$ - $j$ - $j$	64.5	2.9
$e$ - $j$ - $j$	14.8	1.0
$j$ - $j$ - $\nu$	85.6	2.4

## Set 2

$M^{\text{Jet}}/P_T^{\text{Jet}} > 0.1$
$M^{\text{Jet}}/P_T^{\text{Jet}} > 0.12$ if $EM_{\text{frac}}^{\text{Jet}} > 0.9$
$\langle R \rangle > 0.02$
$\langle R \rangle > 0.04$ if $EM_{\text{frac}}^{\text{Jet}} > 0.9$

Event Class	Fake Rejection (%)	Non-Fake Rejection (%)
$j-j$	74.8	0.8
$e-j$	29.5	0.7
$\mu-j$	89.8	3.8
$j-\nu$	88.9	1.4
$j-\gamma$	61.7	0.8
$j-j-j$	56.4	1.6
$e-j-j$	14.1	0.9
$j-j-\nu$	85.6	2.4

## Set 3

In this study, a cut on the number of tracks in a jet,  $N_{\text{Track}}^{\text{Jet}} > 0$ , has been applied. In the  $\phi$ -crack regions of the LAr calorimeter the cut has been tightened ( $N_{\text{Track}}^{\text{Jet}} > 1$ ).  $\phi_{\text{crack}}$  is defined in sec. 4.4.2.

$N_{\text{Track}}^{\text{Jet}} > 0$
$N_{\text{Track}}^{\text{Jet}} > 1$ if $\phi^{\text{Jet}} \in \phi_{\text{crack}} \pm 2^\circ$
$\langle R \rangle > 0.1$ if $EM_{\text{frac}}^{\text{Jet}} > 0.9$

Event Class	Fake Rejection (%)	Non-Fake Rejection (%)
$j-j$	64.2	3.6
$e-j$	25.1	2.6
$\mu-j$	71.4	3.8
$j-\nu$	40.7	3.0
$j-\gamma$	50.6	4.5
$j-j-j$	50.4	6.3
$e-j-j$	14.8	3.3
$j-j-\nu$	42.5	5.1

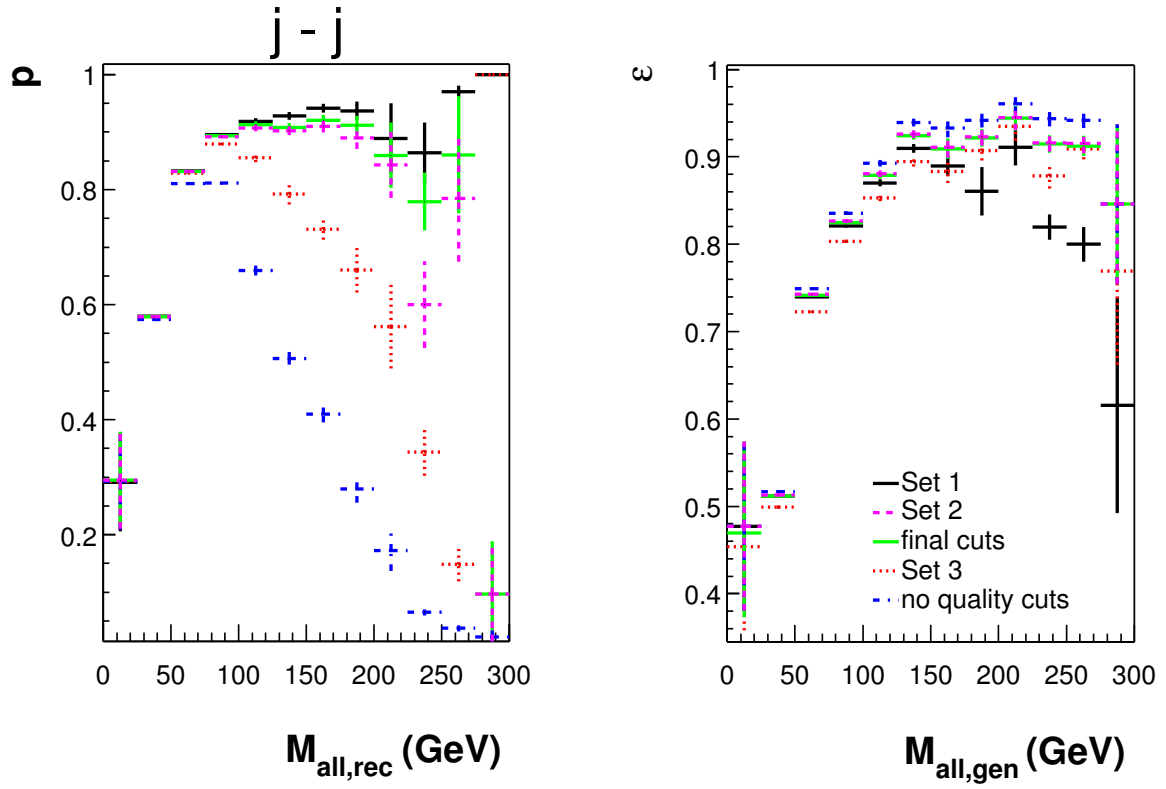


**Figure C.2:** Comparison of purities (left side) and efficiencies (right side) for different jet quality criteria as a function of the invariant mass  $M_{\text{all}}$  of the two jets selected in the  $j$ - $j$  event class. The subscripts  $\text{rec}$  and  $\text{gen}$  denote the reconstructed and generated invariant masses, respectively. The final cuts are those described in sec. 4.4.1.

---

## Appendix **D**: Shape Difference between Data and Standard Model

---

The main contribution to the systematic uncertainties arises from a difference in shape between data and SM in the non-signal region. The non-signal region is defined by inverting the cuts for the  $W$  selection and is thus given by the region corresponding to  $|\cos \hat{\theta}| > 0.6$  for  $M_{jj} > 70$  GeV and to  $0 \leq |\cos \hat{\theta}| \leq 1$  for  $M_{jj} < 70$  GeV. Fig. **D.1** displays the shape difference between the data and the corresponding SM expectation ("Data/SM") for various kinematical quantities. The SM expectation has been normalised to the number of data events. It is presented for the pseudorapidity of all jets and  $P_T^X$  at the top of fig. **D.1**, as well as for  $y_{JB}$  and  $|\cos \hat{\theta}|$  at the bottom. The difference in shape between data and SM is described within 15%, except for the high  $y_{JB}$  region, which is accounted for by an additional uncertainty.

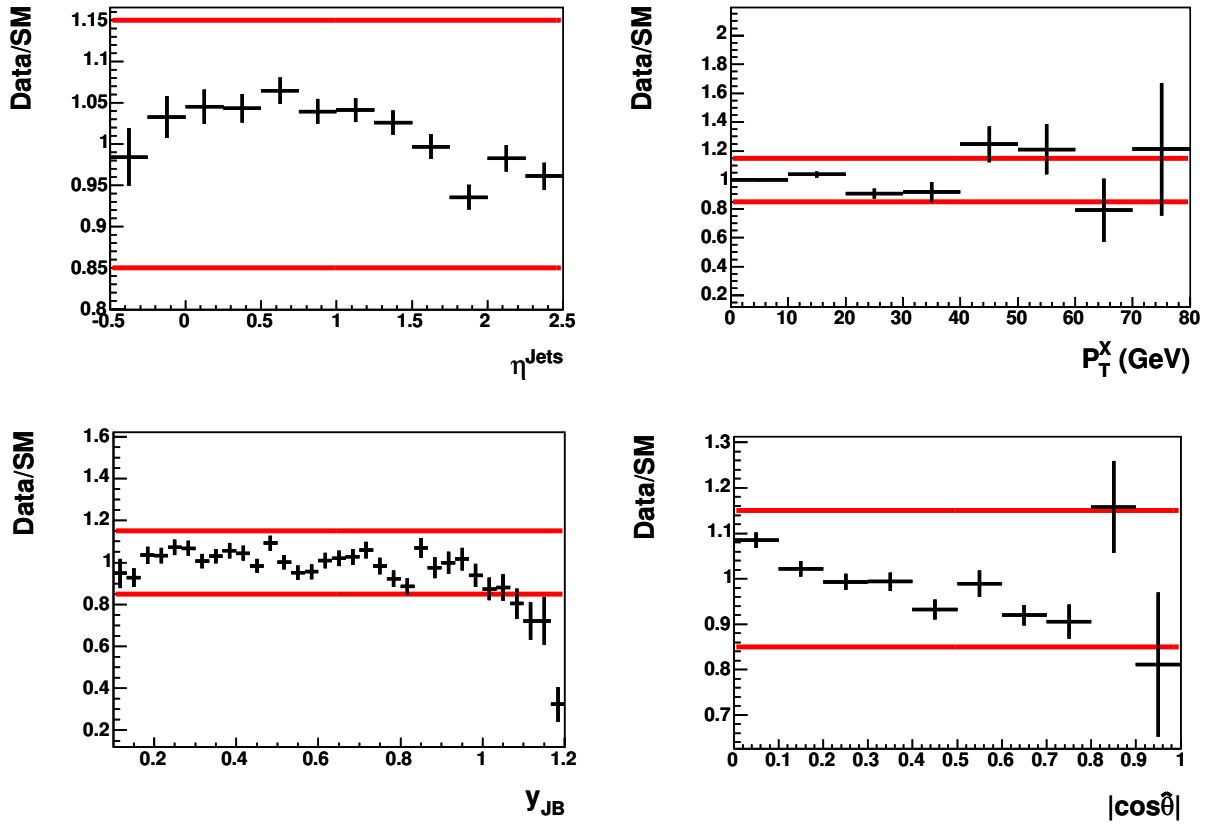


**Figure D.1:** The difference in shape between data and SM in the non-signal region. The ratio between the data and the SM distributions is shown for the pseudorapidity of all jets and  $P_T^X$  at the top, as well as for  $y_{JB}$  and  $|\cos \hat{\theta}|$  at the bottom. The SM expectation has been normalised to the number of data events.



---

## Appendix **E**: Compatibility of Measurements

---

Let's assume that the SM  $W$  expectation (SM ( $W$ )) has to be modified by a factor  $f$  to obtain a SM expectation  $\mu$  that exactly fits the measured data:  $\mu = f \cdot \text{SM} (W) + \text{SM} (\text{bg})$ . The observed and predicted event rates in the leptonic and hadronic channels are for  $P_T^X > 40 \text{ GeV}$ :

Channel	$n$	SM(total)	SM ( $W$ )	SM (bg)
Lepton (lep)	6	$1.08 \pm 0.22$	$0.96 \pm 0.22$	$0.12 \pm 0.04$
Hadron (had)	27	$30.9 \pm 6.7$	$1.9 \pm 0.4$	$29.0 \pm 6.7$

Here,  $n$  denotes the measured number of data events and SM (bg) the background expectation.

One can evaluate the Likelihood functions  $L(f_{\text{lep}})$  and  $L(f_{\text{had}})$ , as well as the corresponding negative logarithmic Likelihood functions  $F_{\text{lep}}$  and  $F_{\text{had}}$ , based on the Poisson distributions of the measured number of data events, e.g. for the leptonic channel:

$$\begin{aligned}
 L(f_{\text{lep}}) &= P(n_{\text{lep}} | \mu_{\text{lep}}) \\
 &= \frac{e^{-\mu_{\text{lep}}} \mu_{\text{lep}}^{n_{\text{lep}}}}{n_{\text{lep}}!}
 \end{aligned}$$

$$F_{\text{lep}} = -\ln L(f_{\text{lep}}) = (\mu_{\text{lep}} - n_{\text{lep}} \ln \mu_{\text{lep}}) + \text{const.},$$

and similarly for the hadronic channel. The best likelihood fit to the measurements and their expectations then yields for the

- hadronic channel:  $f_{\text{had}} = -0.3_{-2.0}^{+2.9}$  (including systematic uncertainties)
- leptonic channel:  $f_{\text{lep}} = +6.2_{-2.3}^{+3.0}$  (including systematic uncertainties)

An evaluation of the compatibility  $C$  (in standard deviation  $\sigma$ ) of the two measurements is straightforward:

$$C = \frac{f_{\text{lep}} - f_{\text{had}}}{\sqrt{\sigma_{\text{lep}}^2 + \sigma_{\text{had}}^2}} \approx 1.8\sigma.$$

Here, it has been assumed that the uncertainties on the expectation for the leptonic channel ( $\sigma_{\text{lep}}$ ) and for the hadronic channel ( $\sigma_{\text{had}}$ ) are uncorrelated.

---

# Bibliography

---

- [1] G. A. Voss and B. H. Wiik, *The Electron Proton Collider Hera*, Ann. Rev. Nucl. Part. Sci. **44** (1994) 413. 1
- [2] H1 Collaboration, contributed [paper #118](#) to the Int. Europhysics Conf. on High Energy Physics, July 2003, Aachen. 2
- [3] M. Wessels, *General Search for New Phenomena in ep Scattering at HERA*, Ph.D. Thesis, RWTH Aachen, Germany (in preparation - to be available at [http://www-h1.desy.de/publications/theses\\_list.html](http://www-h1.desy.de/publications/theses_list.html)). 2, 47, 49, 59, 60, 63, 64, 65, 66, 68, 69
- [4] V. Andreev *et al.* [H1 Collaboration], *Isolated electrons and muons in events with missing transverse momentum at HERA*, Phys. Lett. B **561** (2003) 241 [[arXiv:hep-ex/0301030](#)]. 2, 22, 50, 65, 68, 71, 83, 84, 95, 101, 103, 104
- [5] See, e.g., Ch. Berger, *Elementarteilchenphysik*, Springer (2002); 3, 15, 88  
R.K. Ellis, W.J. Stirling, B.R. Webber, *QCD and Collider Physics*, Cambridge University Press (1995);  
M.E. Peskin, D.V. Schroeder, *An Introduction to Quantum Field Theory*, Perseus Books (1995).
- [6] See, e.g., M. Klasen, *Theory of hard photoproduction*, Rev. Mod. Phys. **74** (2002) 1221 [[arXiv:hep-ph/0206169](#)]; 3  
M. Kuze and Y. Sirois, *Search for particles and forces beyond the standard model in high energy lepton hadron and hadron hadron collisions*, Prog. Part. Nucl. Phys. **50** (2003) 1 [[arXiv:hep-ex/0211048](#)].
- [7] R. P. Feynman, *Photon Hadron Interactions*, Benjamin, New York (1972). 4

- [8] J. D. Bjorken and E. A. Paschos, *Inelastic Electron Proton And Gamma Proton Scattering, And The Structure Of The Nucleon*, Phys. Rev. **185** (1969) 1975. 5
- [9] C. Adloff et al. [H1 Collaboration], *Measurement and QCD analysis of neutral and charged current cross sections at HERA*, [[arXiv:hep-ex/0304003](#)]. 5, 6, 26, 63, 65
- [10] H. Spiesberger et al., in Proceedings of the Workshop *Physics at HERA*, vol. 2, eds. W. Buchmüller, G. Ingelman, DESY (1992) 798. 5
- [11] A. Arbuzov, D. Y. Bardin, J. Bluemlein, L. Kalinovskaya and T. Riemann, *HECTOR 1.00 - A program for the calculation of QED, QCD and electroweak corrections to ep and IN deep inelastic neutral and charged current scattering*, Comput. Phys. Commun. **94** (1996) 128 [[arXiv:hep-ph/9511434](#)]. 6
- [12] P. Kessler, *Sur une méthode simplifiée de calcul pour les processus relativistes en électrodynamique quantique*, Nuovo Cimento **17** (1960) 809. 7
- [13] V. M. Budnev, I. F. Ginzburg, G. V. Meledin and V. G. Serbo, *The Two Photon Particle Production Mechanism. Physical Problems. Applications. Equivalent Photon Approximation*, Phys. Rept. **15** (1974) 181. 7, 12
- [14] S. Frixione, M. L. Mangano, P. Nason and G. Ridolfi, *Improving the Weizsacker-Williams approximation in electron - proton collisions*, Phys. Lett. B **319** (1993) 339 [[arXiv:hep-ph/9310350](#)]. 7
- [15] H. Bethe and W. Heitler, *On The Stopping Of Fast Particles And On The Creation Of Positive Electrons*, Proc. Roy. Soc. Lond. A **146** (1934) 83. 10
- [16] N. Arteaga-Romero, C. Carimalo and P. Kessler, *High P(T) Lepton Pair Production At E P Colliders: Comparison Between Various Production Mechanisms*, Z. Phys. C **52** (1991) 289. 13
- [17] U. Baur, J. A. Vermaseren and D. Zeppenfeld, *Electroweak vector boson production in high-energy e p collisions*, Nucl. Phys. B **375** (1992) 3. 13, 21
- [18] J. C. Pati and A. Salam, *Unified Lepton - Hadron Symmetry And A Gauge Theory Of The Basic Interactions*, Phys. Rev. D **8** (1973) 1240. 15, 16
- [19] H. Georgi and S. L. Glashow, *Unity Of All Elementary Particle Forces*, Phys. Rev. Lett. **32** (1974) 438. 15
- [20] P. Langacker, *Grand Unified Theories And Proton Decay*, Phys. Rept. **72** (1981) 185. 15
- [21] J. L. Hewett and T. G. Rizzo, *Low-Energy Phenomenology Of Superstring Inspired E(6) Models*, Phys. Rept. **183** (1989) 193. 15

- 
- [22] B. Schrempp and F. Schrempp, *Light Leptoquarks*, Phys. Lett. B **153** (1985) 101; [15](#)  
J. Wudka, *Composite Leptoquarks*, Phys. Lett. B **167** (1986) 337.
- [23] S. Dimopoulos and L. Susskind, *Mass Without Scalars*, Nucl. Phys. B **155** (1979) 237; [15](#)  
S. Dimopoulos, *Technicolored Signatures*, Nucl. Phys. B **168** (1980) 69;  
E. Farhi and L. Susskind, *A Technicolored G.U.T.*, Phys. Rev. D **20** (1979) 3404; Phys. Rept. **74** (1981) 277.
- [24] H1 Collaboration, contributed [paper #105](#) to the Int. Europhysics Conf. on High Energy Physics, July 2003, Aachen; [15](#)  
C. Adloff *et al.* [H1 Collaboration], *A search for leptoquark bosons in  $e^- p$  collisions at HERA*, Phys. Lett. B **523** (2001) 234 [[arXiv:hep-ex/0107038](#)];  
S. Chekanov *et al.* [ZEUS Collaboration], *A search for resonance decays to lepton + jet at HERA and limits on leptoquarks*, Phys. Rev. D **68** (2003) 052004 [[arXiv:hep-ex/0304008](#)].
- [25] J. Breitweg *et al.* [ZEUS Collaboration], *A search for resonance decays to anti- $\nu$  jet in  $e^+ p$  scattering at HERA*, Phys. Rev. D **63** (2001) 052002 [[arXiv:hep-ex/0009059](#)]. [15](#), [53](#)
- [26] J. C. Pati and A. Salam, *Lepton Number As The Fourth Color*, Phys. Rev. D **10** (1974) 275. [16](#), [20](#)
- [27] H. P. Nilles, *Supersymmetry, Supergravity And Particle Physics*, Phys. Rept. **110** (1984) 1 and references therein. [16](#), [18](#)
- [28] H. E. Haber and G. L. Kane, *The Search For Supersymmetry: Probing Physics Beyond The Standard Model*, Phys. Rept. **117** (1985) 75 and references therein. [16](#)
- [29] C. Adloff *et al.* [H1 Collaboration], *A search for leptoquark bosons and lepton flavor violation in  $e^+ p$  collisions at HERA*, Eur. Phys. J. C **11** (1999) 447 [Erratum-ibid. C **14** (2000) 553] [[arXiv:hep-ex/9907002](#)]; [16](#)  
ZEUS Collaboration, contributed [paper #498](#) to the Int. Europhysics Conf. on High Energy Physics, July 2003, Aachen;  
ZEUS Collaboration, contributed [paper #906](#) to XXXIst Int. Conf. on High Energy Physics, July 2002, Amsterdam;  
S. Chekanov *et al.* [ZEUS Collaboration], *Search for lepton-flavor violation in  $e^+ p$  collisions at HERA*, Phys. Rev. D **65** (2002) 092004 [[arXiv:hep-ex/0201003](#)].
- [30] H. Harari, *Composite Models For Quarks And Leptons*, Phys. Rept. **104** (1984) 159; [16](#)  
K. Hagiwara, D. Zeppenfeld and S. Komamiya, *Excited Lepton Production At Lep And Hera*, Z. Phys. C **29** (1985) 115;

- U. Baur, M. Spira and P. M. Zerwas, *Excited Quark And Lepton Production At Hadron Colliders*, Phys. Rev. D **42** (1990) 815;
- F. Boudjema, A. Djouadi and J. L. Kneur, *Excited fermions at  $e^+ e^-$  and  $e p$  colliders*, Z. Phys. C **57** (1993) 425.
- [31] C. Adloff *et al.* [H1 Collaboration], *Search for excited electrons at HERA*, Phys. Lett. B **548** (2002) 35 [[arXiv:hep-ex/0207038](#)]; 17
- C. Adloff *et al.* [H1 Collaboration], *Search for excited neutrinos at HERA*, Phys. Lett. B **525** (2002) 9 [[arXiv:hep-ex/0110037](#)];
- S. Chekanov *et al.* [ZEUS Collaboration], *Searches for excited fermions in  $e p$  collisions at HERA*, Phys. Lett. B **549** (2002) 32 [[arXiv:hep-ex/0109018](#)];
- J. Breitweg *et al.* [ZEUS Collaboration], *A search for excited fermions in  $e^+ p$  collisions at HERA*, Z. Phys. C **76** (1997) 631 [[arXiv:hep-ex/9708007](#)].
- [32] T. Stelzer, Z. Sullivan and S. Willenbrock, *Single-top-quark production via  $W$ -gluon fusion at next-to-leading order*, Phys. Rev. D **56** (1997) 5919 [[arXiv:hep-ph/9705398](#)]; 17
- S. Moretti and K. Odagiri, *Single-top production at future  $e p$  colliders*, Phys. Rev. D **57** (1998) 3040 [[arXiv:hep-ph/9709435](#)].
- [33] D. Atwood, L. Reina and A. Soni, *Probing flavor changing top - charm - scalar interactions in  $e^+ e^-$  collisions*, Phys. Rev. D **53** (1996) 1199 [[arXiv:hep-ph/9506243](#)]; 17
- R. D. Peccei and X. Zhang, *Dynamical Symmetry Breaking And Universality Breakdown*, Nucl. Phys. B **337** (1990) 269;
- G. M. de Divitiis, R. Petronzio and L. Silvestrini, *Flavour changing top decays in supersymmetric extensions of the standard model*, Nucl. Phys. B **504** (1997) 45 [[arXiv:hep-ph/9704244](#)];
- H. Fritzsch and D. Holtmannspotter, *The production of single  $t$ -quarks at LEP and HERA*, Phys. Lett. B **457** (1999) 186 [[arXiv:hep-ph/9901411](#)].
- [34] A. Aktas *et al.* [H1 Collaboration], *Search for single top quark production in  $e p$  collisions at HERA*, [[arXiv:hep-ex/0310032](#)]. 17
- [35] S. Chekanov *et al.* [ZEUS Collaboration], *Search for single-top production in  $e p$  collisions at HERA*, Phys. Lett. B **559** (2003) 153 [[arXiv:hep-ex/0302010](#)]. 17, 83
- [36] G. F. Giudice and R. Rattazzi, *Theories with gauge-mediated supersymmetry breaking*, Phys. Rept. **322** (1999) 419 [[arXiv:hep-ph/9801271](#)] and references therein. 18
- [37] H1 Collaboration, contributed paper #101 to the Int. Europhysics Conf. on High Energy Physics, July 2003, Aachen; 19

- C. Adloff *et al.* [H1 Collaboration], *Searches at HERA for squarks in R-parity violating supersymmetry*, Eur. Phys. J. C **20** (2001) 639 [[arXiv:hep-ex/0102050](#)];
- S. Aid *et al.* [H1 Collaboration], *A Search for Selectrons and Squarks at HERA*, Phys. Lett. B **380** (1996) 461 [[arXiv:hep-ex/9605002](#)];
- S. Aid *et al.* [H1 Collaboration], *A Search for Squarks of Rp-Violating SUSY at HERA*, Z. Phys. C **71** (1996) 211 [[arXiv:hep-ex/9604006](#)];
- J. Breitweg *et al.* [ZEUS Collaboration], *Search for selectron and squark production in  $e+p$  collisions at HERA*, Phys. Lett. B **434** (1998) 214 [[arXiv:hep-ex/9806019](#)].
- [38] E. Eichten, K. D. Lane and M. E. Peskin, *New Tests For Quark And Lepton Substructure*, Phys. Rev. Lett. **50** (1983) 811; [19](#)
- R. Ruckl, *Effects Of Compositeness In Deep Inelastic Scattering*, Phys. Lett. B **129** (1983) 363;
- R. Ruckl, *Probing Lepton And Quark Substructure In Polarized  $E+N$  Scattering*, Nucl. Phys. B **234** (1984) 91;
- P. Haberl, F. Schrempp and H.-U. Martyn, in *Proceedings of the Workshop Physics at HERA*, eds. W. Buchmüller and G. Ingelmann, Vol. 2, p.1133, DESY, Hamburg, 1991.
- [39] E. Fermi, *An Attempt Of A Theory Of Beta Radiation*, Z. Phys. **88** (1934) 161; [19](#)
- E. Fermi, *Trends To A Theory Of Beta Radiation. (In Italian)*, Nuovo Cim. **11** (1934) 1.
- [40] C. Adloff *et al.* [H1 Collaboration], *Search for new physics in  $e+-q$  contact interactions at HERA*, Phys. Lett. B **568** (2003) 35 [[arXiv:hep-ex/0305015](#)]; [19](#)
- C. Adloff *et al.* [H1 Collaboration], *Search for compositeness, leptoquarks and large extra dimensions in  $e q$  contact interactions at HERA*, Phys. Lett. B **479** (2000) 358 [[arXiv:hep-ex/0003002](#)];
- ZEUS Collaboration, contributed [paper #602](#) to the Int. Europhysics Conf. on High Energy Physics, July 2001, Budapest;
- J. Breitweg *et al.* [ZEUS Collaboration], *Search for contact interactions in deep inelastic  $e+p \rightarrow e+X$  scattering at HERA*, Eur. Phys. J. C **14** (2000) 239 [[arXiv:hep-ex/9905039](#)].
- [41] I. Antoniadis, N. Arkani-Hamed, S. Dimopoulos and G. R. Dvali, *New dimensions at a millimeter to a Fermi and superstrings at a TeV*, Phys. Lett. B **436** (1998) 257 [[arXiv:hep-ph/9804398](#)]; [19](#)
- N. Arkani-Hamed, S. Dimopoulos and G. R. Dvali, *The hierarchy problem and new dimensions at a millimeter*, Phys. Lett. B **429** (1998) 263 [[arXiv:hep-ph/9803315](#)];
- N. Arkani-Hamed, S. Dimopoulos and G. R. Dvali, *Phenomenology, astrophysics and cosmology of theories with sub-millimeter dimensions and TeV scale quantum gravity*, Phys. Rev. D **59** (1999) 086004 [[arXiv:hep-ph/9807344](#)].

- [42] R. N. Mohapatra and J. C. Pati, *Left-Right Gauge Symmetry And An 'Isoconjugate' Model Of CP Violation*, Phys. Rev. D **11** (1975) 566; 20  
R. N. Mohapatra and J. C. Pati, *A 'Natural' Left-Right Symmetry*, Phys. Rev. D **11** (1975) 2558.
- [43] G. Senjanovic and R. N. Mohapatra, *Exact Left-Right Symmetry And Spontaneous Violation Of Parity*, Phys. Rev. D **12** (1975) 1502. 20
- [44] B. Dutta and R. N. Mohapatra, *Phenomenology of light remnant doubly charged Higgs fields in the supersymmetric left-right model*, Phys. Rev. D **59** (1999) 015018 [[arXiv:hep-ph/9804277](#)] and references therein. 20
- [45] H1 Collaboration, contributed [paper #1020](#) to XXXIst Int. Conf. on High Energy Physics, July 2002, Amsterdam. 20
- [46] R. Brun *et al.*, *GEANT3 User's guide*, CERN-DD/EE/84-1 (1987). 20
- [47] H. Jung, *Hard diffractive scattering in high-energy  $e p$  collisions and the Monte Carlo generation RAPGAP*, Comput. Phys. Commun. **86** (1995) 147. 20
- [48] A. Kwiatkowski, H. Spiesberger and H. J. Mohring, *Heracles: An Event Generator For  $E P$  Interactions At Hera Energies Including Radiative Processes: Version 1.0*, Comput. Phys. Commun. **69** (1992) 155. 20
- [49] H. L. Lai *et al.* [CTEQ Collaboration], *Global QCD analysis of parton structure of the nucleon: CTEQ5 parton distributions*, Eur. Phys. J. C **12** (2000) 375 [[arXiv:hep-ph/9903282](#)]. 20
- [50] G. Ingelman, A. Edin and J. Rathsman, *LEPTO 6.5 - A Monte Carlo Generator for Deep Inelastic Lepton-Nucleon Scattering*, Comput. Phys. Commun. **101** (1997) 108 [[arXiv:hep-ph/9605286](#)]. 21
- [51] H. Spiesberger, *HERACLES and DJANGO: Event Generation for  $ep$  Interactions at HERA Including Radiative Processes*, 1998, available at <http://www.desy.de/~hspiesb/djangoh.html>. 21
- [52] L. Lonnblad, *ARIADNE version 4: A Program for simulation of QCD cascades implementing the color dipole model*, Comput. Phys. Commun. **71** (1992) 15. 21
- [53] T. Sjostrand, P. Eden, C. Friberg, L. Lonnblad, G. Miu, S. Mrenna and E. Norrbin, *High-energy-physics event generation with PYTHIA 6.1*, Comput. Phys. Commun. **135** (2001) 238 [[arXiv:hep-ph/0010017](#)]. 21
- [54] B. Andersson, G. Gustafson, G. Ingelman and T. Sjostrand, *Parton Fragmentation And String Dynamics*, Phys. Rept. **97** (1983) 31. 21



- 
- [55] M. Gluck, E. Reya and A. Vogt, *Parton structure of the photon beyond the leading order*, Phys. Rev. D **45** (1992) 3986. [21](#)
- [56] C. Berger and P. Kandel, in Proceedings of the Workshop *Monte Carlo Generators for HERA Physics*, ed. A. Doyle et al., DESY-PROC-1999-02, p.596. [21](#)
- [57] S. Kawabata, *A New Monte Carlo Event Generator For High-Energy Physics*, Comput. Phys. Commun. **41** (1986) 127. [21](#)
- [58] T. Abe, *GRAPE-Dilepton (Version 1.1): A generator for dilepton production in e p collisions*, Comput. Phys. Commun. **136** (2001) 126 [[arXiv:hep-ph/0012029](#)]. [21](#)
- [59] T. Ishikawa, T. Kaneko, K. Kato, S. Kawabata, Y. Shimizu and H. Tanaka [MINAMI-TATEYA group Collaboration], *GRACE manual: Automatic generation of tree amplitudes in Standard Models: Version 1.0*, KEK-92-19. [21](#)
- [60] A. Mucke, R. Engel, J. P. Rachen, R. J. Protheroe and T. Stanev, *Monte Carlo simulations of photohadronic processes in astrophysics*, Comput. Phys. Commun. **124** (2000) 290 [[arXiv:astro-ph/9903478](#)]. [21](#)
- [61] K. P. Diener, C. Schwanenberger and M. Spira, *Photoproduction of W bosons at HERA: QCD corrections*, Eur. Phys. J. C **25** (2002) 405 [[arXiv:hep-ph/0203269](#)]; [21](#), [22](#)  
P. Nason, R. Ruckl and M. Spira, *A note on W boson production at HERA*, J. Phys. G **25** (1999) 1434 [[arXiv:hep-ph/9902296](#)];  
M. Spira, *W boson production at NLO*, [[arXiv:hep-ph/9905469](#)].
- [62] K. P. Diener, C. Schwanenberger and M. Spira, *Photoproduction of W bosons at HERA: Reweighting method for implementing QCD corrections in Monte Carlo programs*, [[arXiv:hep-ex/0302040](#)]. [21](#)
- [63] P. Aurenche et al., *Higher order QCD corrections to the photoproduction of a direct photon at HERA*, Z. Phys. C **56** (1992) 589. [22](#)
- [64] H. L. Lai et al., *Improved parton distributions from global analysis of recent deep inelastic scattering and inclusive jet data*, Phys. Rev. D **55** (1997) 1280 [[arXiv:hep-ph/9606399](#)]. [22](#)
- [65] C. Diaconu, in Proceedings of the Workshop *Monte Carlo Generators for HERA Physics*, ed. A. Doyle et al., DESY-PROC-1999-02, p.631. [22](#), [88](#)
- [66] J. R. Schneider, P. Soding, G. A. Voss, A. Wagner and B. H. Wiik, *The Deutsches Elektronen Synchrotron*, Europhys. News **25** (1994) 91. [23](#)

- [67] I. Abt *et al.* [H1 Collaboration], *The H1 Detector At Hera*, Nucl. Instrum. Meth. A **386** (1997) 310; 23, 24
- I. Abt *et al.* [H1 Collaboration], *The Tracking, calorimeter and muon detectors of the H1 experiment at HERA*, Nucl. Instrum. Meth. A **386** (1997) 348;
- B. Andrieu *et al.* [H1 Calorimeter Group Collaboration], *The H1 liquid argon calorimeter system*, Nucl. Instrum. Meth. A **336** (1993) 460.
- [68] ZEUS Collaboration, *The ZEUS detector*, Status Report 1993, DESY, Hamburg (1993). 23
- [69] HERA-B Collaboration, Web Page: <http://www-hera-b.desy.de>. 23
- [70] HERMES Collaboration, Web Page: <http://www-hermes.desy.de>. 23
- [71] B. Andrieu *et al.* [H1 Calorimeter Group], *Electron / pion separation with the H1 LAr calorimeters*, Nucl. Instrum. Meth. A **344** (1994) 492; 26
- B. Andrieu *et al.* [H1 Calorimeter Group Collaboration], *Beam tests and calibration of the H1 liquid argon calorimeter with electrons*, Nucl. Instrum. Meth. A **350** (1994) 57;
- B. Andrieu *et al.* [H1 Calorimeter Group Collaboration], *Results from pion calibration runs for the H1 liquid argon calorimeter and comparisons with simulations*, Nucl. Instrum. Meth. A **336** (1993) 499.
- [72] H1 Collaboration, *Technical proposal to upgrade the backward scattering region of the H1 detector*, DESY-PRC-93-02. 26
- [73] R. D. Appuhn *et al.* [H1 SPACAL Group Collaboration], *The H1 lead/scintillating-fibre calorimeter*, Nucl. Instrum. Meth. A **386** (1997) 397. 26
- [74] B. Abbott *et al.* [D0 Collaboration], *Search for new physics in  $e$  muon  $X$  data at D0 using Sherlock: A quasi model independent search strategy for new physics*, Phys. Rev. D **62** (2000) 092004 [[arXiv:hep-ex/0006011](https://arxiv.org/abs/hep-ex/0006011)]. 33, 69
- [75] B. Abbott *et al.* [D0 Collaboration], *A quasi-model-independent search for new high  $p(T)$  physics at D0*, Phys. Rev. Lett. **86** (2001) 3712 [[arXiv:hep-ex/0011071](https://arxiv.org/abs/hep-ex/0011071)]. 33
- [76] V. M. Abazov *et al.* [D0 Collaboration], *Search for new physics using QUAERO: A general interface to D0 event data*, Phys. Rev. Lett. **87** (2001) 231801 [[arXiv:hep-ex/0106039](https://arxiv.org/abs/hep-ex/0106039)]. 33
- [77] C. Adloff *et al.* [H1 Collaboration], *Measurement of dijet cross sections in photoproduction at HERA*, Eur. Phys. J. C **25** (2002) 13 [[arXiv:hep-ex/0201006](https://arxiv.org/abs/hep-ex/0201006)]. 34, 65
- [78] QBGFMAR: *An updated PHAN package for cosmic and halo muon topological rejection in high  $P_T$  physics analysis*, H1 internal note-556 (1998). 36

- 
- [79] B. Leissner, *Muon pair production in electron proton collisions*, Phd. Thesis, RWTH Aachen, Germany, 2002, DESY-THESIS-2002-049, also available at [http://www-h1.desy.de/publications/theses\\_list.html](http://www-h1.desy.de/publications/theses_list.html). 36, 51, 52
- [80] S. Catani, Y. L. Dokshitzer, M. H. Seymour and B. R. Webber, *Longitudinally invariant  $K(t)$  clustering algorithms for hadron-hadron collisions*, Nucl. Phys. B **406** (1993) 187; 38, 85  
S. D. Ellis and D. E. Soper, *Successive combination jet algorithm for hadron collisions*, Phys. Rev. D **48** (1993) 3160 [[arXiv:hep-ph/9305266](http://arxiv.org/abs/hep-ph/9305266)].
- [81] S. Caron, *Jets in photoproduction at HERA*, Phd. Thesis, RWTH Aachen, Germany, 2002, DESY-THESIS-2002-035, also available at [http://www-h1.desy.de/publications/theses\\_list.html](http://www-h1.desy.de/publications/theses_list.html). 38, 39, 63
- [82] W. T. Giele, E. W. Glover and D. A. Kosower, *Jet investigations using the radial moment*, Phys. Rev. D **57** (1998) 1878 [[arXiv:hep-ph/9706210](http://arxiv.org/abs/hep-ph/9706210)]. 40
- [83] M. Stoye, *Untersuchung von Endzuständen mit mehreren Elektronen in der Elektron-Proton-Streuung*, Dipl. Thesis, RWTH Aachen, Germany, 2003, also available at <http://mozart.physik.rwth-aachen.de/Diplom-Doktor.html>. 47, 49
- [84] P. Bruel, *Recherche d'interactions au-delà du Modèle Standard à HERA*, Ph.D. Thesis, Université Paris, France, May 1998, also available at [http://www-h1.desy.de/publications/theses\\_list.html](http://www-h1.desy.de/publications/theses_list.html). 47
- [85] U. Bassler *et al.*, *QESCAT -  $e$  identification software in H1PHAN*, H1 internal software package. 47
- [86] H. Albrecht, M. Erdmann, P. Schleper, *A guide to H1PHAN, an H1 physics analysis package*, H1 internal software manual (1997). 47
- [87] V. Blobel, *The BOS System, Dynamic memory management*, University of Hamburg (1987). 47
- [88] A. Aktas *et al.*, *The H1 OO physics analysis project*, H1 internal software manual (2003). 52
- [89] B. Heinemann, *Measurement of charged current and neutral current cross sections in positron proton collisions at  $s^{1/2}$  approx. 300-GeV*, Phd. Thesis, Hamburg University, Germany, 1999, DESY-THESIS-1999-046, also available at [http://www-h1.desy.de/publications/theses\\_list.html](http://www-h1.desy.de/publications/theses_list.html). 58, 59
- [90] A. Vest, Ph.D. Thesis, RWTH Aachen, Germany (in preparation - to be available at [http://www-h1.desy.de/publications/theses\\_list.html](http://www-h1.desy.de/publications/theses_list.html)). 58

- [91] C. Adloff *et al.* [H1 Collaboration], *Diffraction dissociation in photoproduction at HERA*, Z. Phys. C **74** (1997) 221 [[arXiv:hep-ex/9702003](#)]. 58
- [92] J. Ebert *et al.*, *HFS - a software package to cope with the Hadronic Final State*, H1 internal software package. 58, 59
- [93] J. Rauschenberger, *Prozesse des geladenen Stromes in tief- unelastischer Positron-Proton Streuung bei HERA*, Ph.D. Thesis, Hamburg University, Germany, 2002, also available at [http://www-h1.desy.de/publications/theses\\_list.html](http://www-h1.desy.de/publications/theses_list.html). 63
- [94] A. Aktas *et al.* [H1 Collaboration], *Muon pair production in  $e p$  collisions at HERA*, [[arXiv:hep-ex/0311015](#)]. 63, 65
- [95] G. Frising, Appendix to this work, available at <http://mozart.physik.rwth-aachen.de/Diplom-Doktor.html>. 66, 68
- [96] A. Aktas *et al.* [H1 Collaboration], *Multi-electron production at high transverse momenta in  $e p$  collisions at HERA*, [[arXiv:hep-ex/0307015](#)]. 68, 69, 71, 103
- [97] C. Adloff *et al.* [H1 Collaboration], *Observation of events with an isolated high energy lepton and missing transverse momentum at HERA*, Eur. Phys. J. C **5** (1998) 575 [[arXiv:hep-ex/9806009](#)]. 83
- [98] S. Chekanov *et al.* [ZEUS Collaboration], *Isolated tau leptons in events with large missing transverse momentum at HERA*, [[arXiv:hep-ex/0311028](#)]. 83
- [99] J. Breitweg *et al.* [ZEUS Collaboration], *W production and the search for events with an isolated high-energy lepton and missing transverse momentum at HERA*, Phys. Lett. B **471** (2000) 411 [[arXiv:hep-ex/9907023](#)]. 83
- [100] F. Jaquet, A. Blondel, in Proceedings of the Workshop *Study for an ep facility for Europe*, ed. U. Amaldi, DESY-79-48 (1979) 391. 85, 109
- [101] G. Frising, *Eine Likelihood-Analyse der H1 Jet-Daten*, Dipl. Thesis, RWTH Aachen, Germany, 2000, also available at [http://www-h1.desy.de/publications/theses\\_list.html](http://www-h1.desy.de/publications/theses_list.html). 88
- [102] See e.g., C. Quigg, *Gauge Theory of the Strong, Weak and Electromagnetic Interactions*, Benjamin Cummings, Reading (1983). 89
- [103] D.W. Scott, *Multivariate Density Estimation. Theory, Practice and Visualization*, Wiley, New York (1992). 89
- [104] L. Holmstrom, S. R. Sain and H. E. Miettinen, *A New Multivariate Technique For Top Quark Search*, Comput. Phys. Commun. **88** (1995) 195. 89

- 
- [105] K. S. Cranmer, *Kernel estimation in high-energy physics*, Comput. Phys. Commun. **136** (2001) 198 [[arXiv:hep-ex/0011057](#)]. 89
- [106] L. West, *How to use the Heavy Flavour Working Group Track, Muon and Electron Selection Code*, H1 internal software manual (2000). 101



## Acknowledgements

I would like to thank my supervisor Prof. Dr. Christoph Berger for his advice, interest and confidence in me throughout my research work in Hamburg. I am thankful to Prof. Dr. Günter Flügge for kindly accepting to be my second referee. Furthermore, I would like to thank all my colleagues at H1 for their support during my time in Hamburg. I am particularly grateful to Dr. Sascha Caron, Dr. Boris Leißner and Martin Wessels for their great collaboration and assistance in all aspects regarding this thesis and beyond. I especially would like to thank Thomas Kluge, Dr. Hans-Ulrich Martyn and Anja Vest for helpful discussions and for proofreading this thesis, Dr. Carlo Duprel for his helpful tips, and Adil Aktas for his amusing and diverting entertainment. More special thanks go to all other present and former members of the Aachen group in Hamburg. I am also thankful to the H1 collaboration for operating and maintaining the H1 detector. At this place, I want to express my gratitude to my family for supporting me throughout my life. Finally, I am deeply grateful to Sandrine Bauer for her endless support.